Doctoral theses at NTNU, 2022:161

Luis Bracamonte

Development of an Electrochemical Sensor for Alumina Concentration Measurements and Dissolution Characteristics of Alumina in Cryolite Melt.

Doctoral thesis

NTNU
Norwegian University of Science and Technology
Thesis for the Degree of
Philosophiae Doctor
Faculty of Natural Sciences
Department of Materials Science and Engineering

NTNU
Norwegian University of
Science and Technology

Luis Bracamonte

Development of an Electrochemical Sensor for Alumina Concentration Measurements and Dissolution Characteristics of Alumina in Cryolite Melt.

Thesis for the Degree of Philosophiae Doctor

Trondheim, May 2022

Norwegian University of Science and Technology
Faculty of Natural Sciences
Department of Materials Science and Engineering

NTNU
Norwegian University of
Science and Technology

NTNU
Norwegian University of Science and Technology

Thesis for the Degree of Philosophiae Doctor

Faculty of Natural Sciences
Department of Materials Science and Engineering

ISBN 978-82-326-6471-9 (printed ver.)
ISBN 978-82-326-5598-4 (electronic ver.)
ISSN 1503-8181 (printed ver.)
ISSN 2703-8084 (online ver.)

Doctoral theses at NTNU, 2022:161

Printed by NTNU Grafisk senter

Dedicada a la memoria de mi padre, como regalo por todo lo que luchaste.
Y como homenaje a mi madre, a tu amor y apoyo infinito.

Preface

This thesis has been submitted to Norwegian University of Science and Technology, NTNU, in partial fulfilment of the requirements for the Degree of Philosophiae Doctor.

The work was mainly performed at the Department of Materials Science and Engineering at NTNU in Trondheim from 2017 to 2021. The work was supervised by Espen Sandnes (Main supervisor, Associated Professor, NTNU), and Christian Rosenkilde (Co-supervisor, Chief Engineer, Hydro Aluminium).

The work was mainly funded by the Norwegian Research Council and partially funded by SFI Metal Production, Centre for Research-based Innovation.

All experimental work presented in this thesis has been conducted by the author, except the following:

Chapter 4: The alumina sensor measurements were performed by master student Karoline Aasen Nilsen under the supervision of Luis Bracamonte.

Chapter 5: The sieving and PSD measurements of some of the aluminas were done by master student Vegard Aulie.

Chapter 7: The experiments to investigate the influence of LiF content on the alumina dissolution was done by Sindre Engzelius Gylver.

Chapter 7: Bath composition analysis and physicochemical analysis on the alumina (PSD, XRF, BET, Phase content) was done by Hydro Aluminium.

All co-authors listed for each paper contributed to the corresponding discussions.

Luis Bracamonte
Trondheim
December 30th, 2021

Acknowledgements

First and foremost, I am very grateful to my main supervisor, Associated Professor Espen Sandnes. Thank you for giving me this opportunity and be part of this project. I have really enjoyed our time working together. Thank you so much for all your guidance and support.

I would also like to thank my co-supervisor Professor Cristian Rosenkilde from Hydro Aluminium. You had many insightful comments and suggestions. Thank you so much for the opportunity to work with you.

I would like to offer a special thanks to Professor Kristian Etienne Einarsrud, you have been a large part of this work and helped me with the discussions in my papers. I am sincerely thankful.

This project has cooperated with the SFI Metal Production (Centre for Research-based Innovation). I would like to thank the participants in this centre, among others the industrial partners Hydro and Alcoa, and the group from NTNU and SINTEF. I am very grateful for the opportunities I have had as part of this centre, and for the encouragement you have given me. I have also appreciated the close collaboration between NTNU and SINTEF that this project has facilitated.

I would like to thank Sindre Engzelius Gylver for the good discussions and help to perform some of the experiments. I would also like to thank the master students involved in my project, Karoline Aasen Nilsen and Vegard Aulie. I appreciate the help of all engineers and equipment responsible personnel I have encountered over the years. Thanks to Pei Na Kui, Elin Harboe Albertsen, Magnus Bentzen Følstad and Anita Storsve. A special thanks to Aksel Alstad from the workshop, all the work that you did was an important part in the development of my project. Henrik Gudbrandsen, thank you for all your help in the lab.

These last years at the department have of course included a lot of people, who made the life as a PhD student a lot easier. Everyone in the department and the electrochemistry group, thank you for all the advice, tips, talks and social gatherings.

To my friends outside of work, you know who you are; you have made life in Trondheim very special.

Last, but not least, I must thank my family. Everyone has always showed a lot of interest in my work. A special thanks goes to Ingunn for all your support and help. Thanks to my mom, this thesis would not have been possible without your support and encouragement. Thank you all so much.

Luis

.

Summary

Alumina concentration is mainly determined in the industry by bath sampling of individual cells and subsequent analysis. Even though this method works relatively well, it has some drawbacks such as long time between the sampling and the analysis, and occasionally sample contamination. These drawbacks can potentially lead to inappropriate operation decisions and result in poor cell performance. A device to perform in-situ alumina concentration measurements would be of great interest both in the industry and in the laboratory. In-situ alumina concentration measurements can give important information in a laboratory setting to improve the understanding about the dissolution process and can further be valuable in an industrial setting to achieve better control of the pots during operation that could lead to an increased energy efficiency of the process.

This work studied the development and behaviour of an in-situ electromotive force (emf) based electrochemical sensor composed of a graphite probe during the addition and dissolution of alumina in cryolite-based melts. The principle of the alumina sensor is based on the measured potential of the graphite electrode immersed in the bath (chamber I) against a reference electrode (chamber II). Thus, the potential between the graphite probe and the reference electrode is due to the difference in activity of alumina in the two chambers. Then, the emf measurements can be indirectly related to a change in alumina concentration when properly calibrated. This method allows to determine the absolute concentration of alumina after addition only if the initial condition or concentration is known. In the present work, alumina concentration measurements are always referring to the measured potentials. The half-cell reactions for the graphite electrode and the reference electrode were derived together with the corresponding Nernst equation. Further, the potentials were calculated for comparison with the experimental results.

Two reference electrodes were tested during the experiments. An aluminium reference electrode and an alumina-saturated graphite quasi-reference electrode. Dissolution of alumina were investigated using emf-measurements at three different experimental systems:

1) Dissolution of alumina in a bath composed of 99 wt% synthetic cryolite and 1 wt% alumina in a sealed furnace under N_2 gas.

2) Dissolution of alumina in a partially open see-through furnace under N_2 gas with the same bath composition as in 1). Video recordings were performed separately with a small variation in the chemical composition of the bath.

3) Dissolution of alumina in an open see-through furnace under nitrogen gas/ambient air. The initial chemical composition of the bath was 75 wt% cryolite, 15 wt% AlF_3, 6.5 wt% CaF_2 and 3.5 wt% LiF and 1 wt% alumina. Video recordings were performed simultaneously as the sensor measurements.

The emf measurements were generally characterized by a gradual decrease in the potential after the addition of the alumina, followed by a stabilization and establishment of a plateau when the potential reached a constant value. The gradual decrease in potential was interpreted as an increase in the alumina concentration and the creation of the plateau as the finalization of the dissolution. There was a satisfactory agreement between the measured and calculated potential values after stabilization for some of the experiments carried out under the first and second experiemental systems. The initial decrease of the potential after the adding alumina to the electrolyte, the establishing of the plateau as well as the agreement between calculated and measured potential supported the fundamental working principle of the sensor. However, for the experiments carried out under the experimental system 3, the measured potential values were in less agreement with the calculated values. The difference arises most likely from the differences in the experimental conditions such as gas composition above the melt, initial chemical composition of the melt with the addition of AlF_3, CaF_2, and LiF or from the assumptions made in calculating the potentials.

In the first system, emf measurements were strongly affected when ambient air leaked into the furnace. An increase in the emf value was observed when a plug from the lid was removed and air entered into the furnace prior to alumina feeding. This phenomenon was most likely due the alterations in the partial pressures of CO and CO_2, due to the reactions between the graphite probe or carbon crucible with the oxygen in air. This phenomenon was not observed in the experimental systems 2 and 3. The open see-through furnace might help to create an equilibrium between adsorbed CO on the probe with the dissolved CO in the melt which was also in equilibrium with the partial pressure of CO above the melt.

An abrupt increase in the potential, also referred to as a “jump”, was observed right after the addition of the alumina during the experiments carried out with systems 1 and 2. It is believed that this sudden jump is the response of the sensor to the generation of gas when the alumina gets in contacts with the bath. Air and moisture are introduced when alumina is added and dissolves into the bath. The

oxygen reacts with the carbon surface of the sensor increasing the CO partial pressure and will lead to an increase in the observed emf voltage. During the experiments carried out in the see-through oven with system 3, no jumps in the potential were observed after the alumina additions. This is believed to be due to the open furnace used in these measurements, which ensures a stable CO concentration, in equilibrium with the atmosphere. However, it is not possible to exclude the impact of the different reference electrodes used.

The dissolution times obtained based on the sensor showed significant faster dissolution process for the secondary alumina than the primary alumina, which is consistent with previous results reported in the literature, and suggested that the sensor was capable for estimating alumina dissolution time. The results from the video recordings were also in fair accordance with the emf measurements, revealing a considerably shorter time needed for the secondary alumina to dissolve. The video recordings also revealed that the dissolution of the primary alumina was characterized by the formation of a crust, followed by the detachment, and sinking of alumina-bath flakes. The dissolution mechanism for the secondary alumina was characterized by rapid dispersion of all the particles throughout the melt leading to a faster dissolution.

An increase in the dissolution time with increasing initial alumina concentration in the melt during the experiments was generally observed in the emf measurements and video recordings. The video recordings revealed that for low alumina concentration the dissolution mainly proceeds through the rapid dispersion and dissolution of a white cloud consisting of alumina particles followed by the formation and rapid dissolution of a thin crust. On the contrary, for high alumina concentration, a thicker crust is formed, and it mainly dissolves by detachment and sinking of alumina-bath flakes.

The dissolution process of alumina fines and bulk alumina and possible correlations with its other physicochemical properties were also studied. Video recordings showed significant differences in the characteristics and time of the dissolution between secondary bulk alumina and secondary alumina fines. The dissolution mechanism of bulk alumina was characterized by a rapid dispersion and dissolution of the alumina particles immediately after the alumina get in contact with the bath. Further, a crust is formed on the top of the bath, followed by detaching and sinking of alumina-bath flakes from it. The last phase of the dissolution is characterized by the decrease in the thickness of the crust until it completely disappears when the dissolution is completed. On the contrary, alumina fines showed less dispersion of the particles in the bath immediately after

feeding and caused a considerably thicker crust than the bulk alumina. The dissolution process of the alumina fines takes place only at the alumina layer-bath surface interface. Towards the end of the dissolution process of alumina fines the alumina layer appears to have smaller pores and be more compact than the crust of the bulk alumina. Alumina fines were characterized by longer dissolution times compared to bulk alumina. The dissolution times of the alumina fines and bulk alumina were found to have a negative correlation with the particle size distribution (PSD), meaning that particles with small surface area tend to promote longer dissolution times. The small size of the particles and the lack of dispersion of alumina fines upon addition leads to the formation of a crust with less contact area between the alumina and the melt. On the other hand, the better dispersion of bulk alumina during addition leads to the formation of a less compact crust. Then the melt can penetrate the crust resulting in more contact between the melt and the alumina leading to the detachment and sinking of alumina flakes and shorter dissolution times.

List of abbreviations

a_x	Activity of species x
BET	Braunauer, Emmett, Teller
BN	Boron nitride
CCD	Critical Current Density
E	Cell potential
E°	Standard cell potential
emf	Electromotive Force
F	Faraday's constant
h	Height
l	Length
LOI	Loss on ignition
LSV	Linear Sweep Voltammetry
MOI	Moisture on ignition
n	Number of moles of electrons per mole of products
P_x	Partial pressure of species x
PSD	Particle Size Distribution
R	Molar gas constant
SEM	Scanning Electron Microscopy
T	Temperature
XRD	X-ray diffraction
XRF	X-ray fluorescence
$Ø_{inner}$	Inner diameter
$Ø_{outer}$	Outer diameter
α	Alpha
δ	Delta
ɣ	Gamma
θ	Theta
ζ	Xi

Table of contents

Chapter 1 Introduction

1.1 Motivation

In recent years, innovations in the aluminium industry have brought improvement in the performance of the electrolysis cells. An example of this is the increase in amperage to 400-500 kA in several aluminium smelters [1] and reaching values up to 600 kA in the most modern cells [2]. These achievements have been accompanied by changes in the design of the cells such as the increase in the size of the anodes, and the reduction in the interpolar distance between the anode and the cathode [3] [4]. These changes have resulted in a reduction in the volume of the bath for dissolving the alumina, thus making feeding, and controlling alumina content more challenging. A good control of the alumina content is imperative for efficient pot operations and to avoid excess or deficiency of alumina content in the cell.

Excess of alumina can lead to the formation of excessive amount of undissolved alumina hindering the dissolution, resulting in unstable cell operations and a reduced energy efficiency of the process. Lack of alumina in the cell can result in failures such as the anode effect, a phenomenon where the passivation of the anodes leads to the formation of gases such as CO, CF_4 and C_2F_6. The anode effect not only results in energy waste and potentially cell instability but also contributes to the greenhouse effect accompanied by fluorocarbon emissions, which are harmful because of their high global warming potential [5]. Therefore, continuous, and representative alumina concentration measurements would bring important improvements to the process to correct the conditions in the operation on time and thus be able to restore and maintain an optimal operation of the cell.

Continuous improvements in the accuracy of the alumina concentration measurements as well as the measurement time have been achieved at an industrial level. However, the method is based on sampling of the bath resulting in a long and tedious process. In addition, after the operator makes the measurement, the samples need to be processed and there is an amount of time needed before obtaining the results. The electrolysis cells are very dynamic, meaning that parameters such as temperature and chemistry in the bath are changing every second. This generates that the decisions for the control of the process are based on old results and not on current conditions [6] [7].

Over the years, initiatives aimed to solve the challenges related to the dissolution of alumina have resulted in the study of different methods for measuring the concentration and dissolution rate of alumina. Some of the studies have been

focused on the development of methods based on electrochemical techniques such as linear sweep voltammetry (LSV), critical current density (CCD), chronopotentiometry or electromotive force (emf) measurements [8] [9] [10] [11]. Visual observations have also served as a useful technique to obtain dissolution rates and physical characteristics of alumina dissolutions [12] [13]. These studies [8-13] represent a first approach in the finding of new solutions to measure more effectively the alumina content of the alumina as well as for the acquisition of data that reveals the most important parameters that influence the dissolution process. However, there is still a lot of improvements to be made and a lot of knowledge to be obtained.

Therefore, investigations related to study the principle and the development of a new method to perform in-situ alumina concentration measurements during the whole dissolution process of the alumina are necessary. Initially, a lab scale study of a method to measure alumina concentrations can lead to the acquisition of important data that improves the understanding about the dissolution process and bring to light the variables that influence the most the dissolution characteristics and dissolution rate of alumina. Then, this method can be valuable to later improve the industrial alumina feeding and achieve better efficient control of the pots during operation, increasing the energy efficiency of the process. In addition, further studies of the physicochemical properties of the alumina such as LOI, MOI, coarse fraction, fines would be also beneficial to obtain a complete view of the dissolution process. .

1.2 Aim of Work

The aim of the present work is to study the principle and performance of a not previously proposed emf-based electrochemical alumina sensor for in-situ alumina concentration measurements during the entire dissolution process in cryolite based melts.

The first objective was to analyze and compare the emf measurements with calculations to explore whether the principle stated for the sensor was correct. The emf measurements were performed during subsequent additions of alumina in cryolite melt. Two references electrodes were used. A traditional aluminium reference electrode, and an alumina-saturated graphite quasi-reference electrode. The theoretical cell voltages were calculated by deriving the half-cell reactions for the alumina sensor and the reference electrodes and finally ending up with a simplified Nernst equation.

The second objective was to compare the emf measurements with video recordings of the addition and dissolution process of different types of alumina,

e.g., primary, and secondary alumina. Video recordings serve as a technique to obtain visual information during the dissolution of alumina, which help to better understand the dissolution characteristics and behaviour of the sensor emf measurements. The video recordings were performed in a see-through furnace, both separately and simultaneously as the sensor measurements.

The last objective was to perform video recordings during the dissolution of different secondary aluminas in order to explore possible correlations between the physicochemical properties and the characteristics of the dissolution in order to expand the knowledge on the dissolution of the alumina in cryolite melts.

1.3 Structure of Thesis

The thesis is a collection of four individual papers, presented in chapters 4-7. This format makes some repetitions inevitable. The papers have been re-formatted to fit with the format of the thesis. The chapters are structured as follows:

Chapter 2: presents some essential concepts on alumina dissolution and a bibliographic review about previous studies on alumina concentration and dissolution measurements.

Chapter 3: summarizes the development of different experimental procedures and different set ups used on the experiments.

Chapter 4: presents the first study of the behaviour of an electrochemical alumina sensor based on a graphite probe. emf measurements between the alumina sensor and two differences reference electrodes were explored (paper 1).

Chapter 5: further studies of the behaviour of the electrochemical alumina sensor were performed. emf-based alumina sensor measurements together with images from a high-speed camera of the addition and dissolution process of primary and secondary alumina were studied (paper 2).

Chapter 6: emf-based alumina sensor measurements and camera video recording were performed simultaneously in a see-through cell during the addition of different secondary alumina and throughout the entire dissolution process. The dissolution time and the characteristics of the dissolution process were obtained (paper 3).

Chapter 7: shows video recordings of the dissolution of additions of bulk alumina and alumina fines. The influence of different physicochemical properties on the dissolution was studied (paper 4).

Chapter 8: highlights the important findings of the chapters 4-7.

Chapter 9: contains the concluding remarks from the chapter 4-7.

Chapter 10: evaluates suggestions for further work.

Appendix A: contains images of the different electrodes used during the investigation. Images of the see-through furnace and set-up are also provided

Appendix B: contains links to videos of the alumina dissolution process for some alumina and melt compositions. The videos make it easier to understand the results presented and the discussion in the thesis.

Appendix C: contains supplementary information that could not be included in some of the chapters.

References

1. G. Tarcy, H. Kvande and A. Tabereaux, "Advancing the Industrial Aluminium Process: 20th Century Breakthrough Inventions and Developments," *JOM,* vol. 63, no. 8, pp. 101-108, 2011.

2. F. Charmier, O. Martin and R. Gariepy, "Development of the AP Technology Through Time," *JOM,* vol. 67, no. 2, pp. 336-341, 2015.

3. O. Martin, S. Despinasse, C. Ritter, R. Santerre and T. Tomasino, *Light Metals,* pp. 255-260, 2008.

4. P. Lavoie, M. Taylor and J. Metson, "A Review of Alumina Feeding and Dissolution," *Metallurgical and Materials Transactions B,* vol. 47B, pp. 2690-2696, 2016.

5. J. Thonstad, P. Fellner, G. M. Haarberg and Å. Sterten, Aluminium Electrolysis. Fundamentals of the Hall-Heroult Process, Aluminium-Verlag, 2001.

6. X. Wang, B. Hosler and G. Tarcy, "Alcoa STARprobe," *Light Metals,* pp. 844-850, 2011.

7. X. Wang, "Alcoa STARprobe Update in Further Development for Measuring Cryolite Properties," *Light Metals ,* pp. 397-402, 2016.

8. R. Haverkamp and B. Welch, "Modelling The Dissolution of Alumina Powder in Cryolite," *Chemical Engineering and Processing,* vol. 37, no. 177-187, 1998.

9. J. Thonstad, "Critical Current Densities in Cryolite Melts," *Electrochemical Acta,* pp. 1219-1226, 1967.

10. J. Thonstad, "Dissolution of Alumina in Cryolite," *Metallurgical Transactions,* vol. 3, p. 408, 1972.

11. N. Vasyunina, I. Vasyunina, Y. Mikhalev and A. Vinogradov, "The Solubility and Dissolution Rate of Alumina in Acidic Cryolite Aluminous Melts," *Metallurgy of Non-Ferrous Metals,* vol. 50, no. 4, pp. 338-342, 2009.

12. Y. Yang, B. Gao, Z. Wang, Z. Shi and X. Hu, "Effect of Physicochemical Properties and Bath Chemistry on Alumina Dissolution Rate in Cryolite Electrolyte," *JOM,* vol. 67, no. 5, pp. 973-983, 2015.

13. Y. Yang, B. Gao, Z. Wang, Z. Shi and X. Hu, "Study on the Dissolution of Alumina in Cryolite Electrolyte Using the See-Through Cell," *Light Metals,* pp. 583-588, 2015.

Chapter 2 Alumina dissolution and previous studies

2.1 The Hall-Héroult process

In the last decades, aluminium has become widely used in several industrial sectors such as construction and transportation among others. The use of aluminium became highly important for the fabrication of buildings, automobiles, aircraft, and spacecraft because of the need of a material with characteristics such as low density, corrosion resistance and mechanical strength. The global production of aluminium has grown considerably since 1950 from 3 million tonnes to 63 million tonnes in 2019. Norway is the second largest producer of aluminium in Europe with 1.3 million tonnes only behind Russia with 3.6 million tonnes. [1]

The method to produce industrial primary aluminium is called the Hall-Héroult process and it has been carried out basically in the same way since its invention in 1886. The process is based on the electrochemical reduction of dissolved alumina in cryolite melt. The primary electrochemical reaction can be one of the following Equation 2.1 and 2.2:

$$Al_2O_{3(l)} + 3C \rightarrow 2Al_{(l)} + 3CO_{(g)} \quad (2.1)$$

$$2Al_2O_{3(l)} + 3C_{(s)} \rightarrow 4Al_{(l)} + 3CO_{2(g)} \quad (2.2)$$

At the cathode, Al^{3+} ions are reduced to liquid aluminium $Al_{(l)}$. At the anode, oxygen containing species are oxidized and produce mainly $CO_{2(g)}$, and some $CO_{(g)}$ [2] [3].

Nowadays, the most common aluminium pots used by the industry are formed by prebake cell. The cells are mainly formed by prebaked carbon anodes, a carbon cathode, and a cryolite-based electrolyte. The carbon anodes which are dipped into the electrolyte are blocks made of petroleum coke aggregates and coal tar

pitch binder. A metal rod is connected in the top of the anode block to conduct the electric current. The cathode is a prebaked carbonaceous block which contains the liquid aluminium and the electrolyte. It is commonly made of semi-graphitic or semi-graphitized carbon material, joined by a carbonaceous seam mix. Metal current collector bars are inserted at the bottom of the blocks. The electrolyte consisted mainly of a cryolite based melt (Na_3AlF_6) because the capacity of the cryolite to dissolve the alumina. Some additives such as aluminium fluoride (AlF_3), and calcium fluoride (CaF_2), are usually added to the bath to obtain lower metal solubility, higher electrical conductivity, lower vapor pressure and thus obtain better cell operations. These additives also reduce the liquidus temperature or melting point of the cryolite leading to lower operating temperatures around 955-965°C. This is considered advantageous because it increases the current efficiency of the process. In general, most of the additive reduce the solubility of the alumina. Modern cells are also equipped with automatic point feeders to add the alumina and with dry scrubbers and close hoods to collect the evolved gasses. A schematic representation of an industrial cell is shown in Figure 2.1.

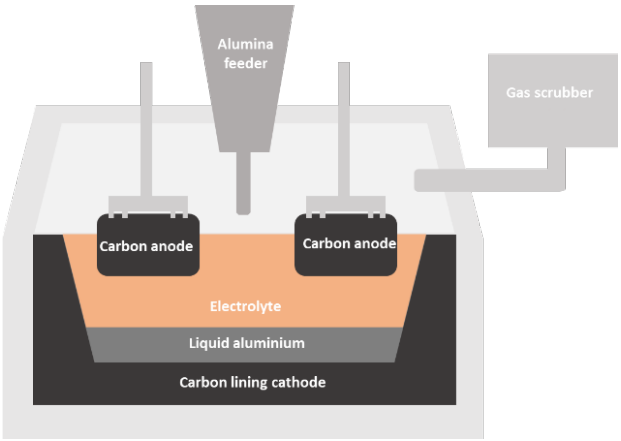

Figure 2.1 Schematic representation of an industrial cell with prebaked anodes.

The basis for dry scrubbers is to remove $HF_{(g)}$ from the cell gases by chemisorption on “fresh alumina”. The fresh alumina captures the particulate fluorides, entrained alumina and carbon dust, and other particulate impurities evolved from the cells. Then, the “reacted” or “secondary alumina” is recycled and added to the melt through the point feeders [2].

Many of the aluminium plants are formed by 150-250 electrochemical cells arranged in series. The cathode of one cell is electrically connected to the anode of the next to form a cell line. The cells are placed side by side in order to reduce adverse magnetic effects of the high electrical current to conserve the heat losses. The interaction between the current flowing through the liquid aluminium pad and the magnetic fields induced by high currents can cause magnetic stirring of the metal pad resulting in metal height variations and instabilities. A special arrangement of the interconnecting electrical system is thus needed to compensate the magnetic forces.

Modern high amperage aluminium pots, 400-500 kA operates stably and efficiently at around 3.85 volts and at energy consumption of 12.5 DC kWh/kg Al [4]. To achieve low energy consumption, it is important to have good control of important cell conditions such as electrolyte composition and stable mass and energy balance in the cell. Thus, high control of the daily cell operations plays an important role for the smelters. Changing of the anodes and metal removal are some of the most important cell operations that can affect the performance of the cell. Anode changing can result in variations in the electrolyte temperature and disturbance of the anodic current distribution of the cell. Tapping of the metal can also produce perturbations of the thermal equilibrium of the cell resulting in instabilities.

A good control of the alumina content is another key parameter for efficient pot operations and to avoid excess or deficiency of alumina content in the cell. High concentration of alumina can lower the liquidus temperature of the melt and result in excess of superheat and change in the acidity of the electrolyte. It can also form undissolved alumina lumps and a decrease in the dissolution rate. Low alumina content in the cell can result in the passivation of the anode or anode effect, leading to the formation of gases such as CO, CF_4 and C_2F_6. All these problems result in unstable cell operations and a decrease in the energy efficiency of the process. Therefore, the development of better alumina concentration measurements has become so important in recent years. Accurate and faster alumina concentration measurements in modern cells, would help to immediately correct possible

variations in the conditions of the cell, so that optimal functioning of the cell can be restored.

2.2 Alumina

Alumina is produced from aluminium hydroxide minerals which are the main component of bauxite. The Bayer process is the principal process to produce alumina. The total world production of alumina was 131 million tonnes in 2019 [1], which most was used in the aluminium industry. Alumina is produced by calcination of $Al(OH)_3$ or gibbsite. This calcination results in the formation of various transition crystal phases such as gamma (γ), delta (δ), xi (ζ), and theta (θ), and a fraction of the stable phase, alpha (α) alumina or corundum, Figure 2.2. [5].

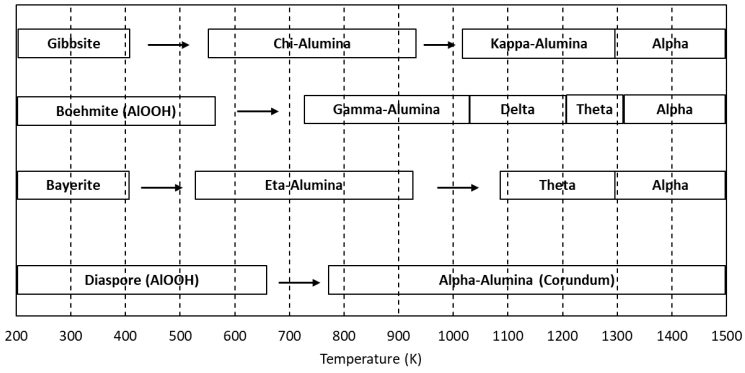

Figure 2.2 Thermal diagram of the transition aluminas (after Wefer and Misra, 1987) [5].

Crystal phases are one of the most important properties for the industry. Gamma alumina, also known as sandy alumina, is characterized by free-flowing properties, and can be conveyed easily. It is one of the preferred types of alumina for the smelters. Gamma alumina is calcined at lower temperature, has coarser crystals with high BET surface area and has a low fraction of fines. Alpha alumina also known as fluory, is formed through high temperature calcination and is a poorly flowing powder. It has a low BET surface area and a higher fraction of fines [2].

The conversion from gamma to alpha alumina leads to a mechanism of interlocking of alumina grains resulting in the formation and sintering of platelets of alumina. Towsend and Boxwall found that crust is formed because gamma alumina dissolves faster in the bath and has a higher solubility limit than alpha alumina, causing local supersaturation. Further, gamma alumina continues to

dissolve, whereas alpha alumina crystallizes cementing the grains together [6]. Large flake-like agglomerates or raft will form and dissolve slower than individual grains due to the lower surface/volume ratio.

2.3 Alumina dissolution

The alumina solubility in cryolitic melts is relatively high, typically ranging between 7-10 wt%, depending on the melt composition and temperature. The high solubility of this strong endothermic process results from the formation of various oxyfluoride complexes. The alumina can take several dissolution paths from the moment of the addition until the dissolution is completed. The preferred path is when the alumina is well dispersed inside the bath right after the addition. Here, a layer of frozen bath is formed around the alumina particles due to the difference in temperature between the alumina and the melt. The layer needs to remelt before the dissolution can continue. The time needed for re-melting is only a small fraction of the total time needed for dissolution [7] [8]. This part of the process is heat transport controlled. Then, the dissolution can occur when the alumina reacts with the bath to form anion complexes such as $Al_2OF_6^{2-}$ at low concentration of alumina [9], Equation 2.3, and $Al_2O_2F_4^{2-}$ at high concentration of alumina [9], Equation 2.4, and direct contact between alumina and bath is re-established. This step is mass transport control.

$$4AlF_6^{3-} + Al_2O_3 = 3Al_2OF_6^{2-} + 6F^- \tag{2.3}$$

$$2AlF_6^{3-} + 2Al_2O_3 = 3Al_2O_2F_4^{2-} \tag{2.4}$$

The other path in the dissolution occurs when the alumina agglomerates as a clump and some bath freeze around the alumina particles. These agglomerates may either float on the bath surface or sink as a dense crust to the surface of the metal pad or to the bottom. The formation of agglomerates takes place when a lack of dispersion of the alumina particles occurs right after the feeding, resulting in a slower path for the dissolution of the alumina particles. Agglomeration is associated with the phase transition from ɣ-Al_2O_3 to α-Al_2O_3, which is catalysed by fluoride [10] and leads to sintering during recrystallization.

2.4 Factors that influence the dissolution process

The variables influencing the rate of dissolution of alumina in cryolite melts can be classified in two groups: Alumina quality and cell conditions

2.4.1 Alumina quality

The quality of the alumina added to the electrolyte melt has been found to have an impact on the dissolution during cell operation. There are different alumina producers worldwide, and small variations in the Bayer process steps results in changes in the physical and chemical properties of the alumina produced. Most smelters base the specifications on their own operating experience. This chapter has the intention to introduce the most common specification and characteristics of the alumina and to present what it seems to be a trend towards more similar requirements and international standardization [11]. However, the most suitable alumina and its physicochemical characteristics for use in alumina reduction cells are still subject to discussion due to numerous inconclusive or contradictory results from different studies [12]. A deeper discussion about the impact of the physicochemical properties of the alumina is shown in Chapter 7.

The phase content

The alpha phase content is given as the mass percentage of the alpha phase in the alumina. Typical alpha contents are usually below 10 wt%. The alpha content is mainly determined by the degree and the quality of the calcination step in the Bayer process. Alpha-alumina, with its low surface area, has been observed to be slower to dissolve in laboratory studies in laboratory studies. [13] [14] [15].

Particle size of the alumina grains

The particle size distribution is an important alumina characteristic that is closely monitored for the smelters. The industrial alumina used in electrochemical cells is a relatively fine-grained material with normal range of grain sizes between 40 and 150 μm [2]. The fraction of finer grains that are less than 45 μm are called fines [16]. Usually, smelters try to keep the fraction of fines lower than 10% during feeding. A high content of fines is considered harmful due to dusting emissions and mechanical handling problems. Very large particles are not wanted either because they are slow to dissolve in the bath. The fraction of large particles is usually kept below 15%. Therefore, the particle sizes should be neither too large nor too small [15]. The fraction with grain less than 20 μm are known as superfine fraction. It is importance to maintain this fraction limited to max. 0.5%. Larger content of superfines affect the current efficiency [17]. Maximum current efficiency requires a clean cell bottom and therefore alumina with stable quality; low in fines and superfines [18]. However, some studies have found that an

increase in content of fines -325 mesh did not affect the dissolution of the alumina [19].

Impurities in the alumina

Even though smelter grade alumina (SGA) is considered a relatively high-purity commodity with an aluminium oxide content in excess of 95.5 wt%, it contains some impurities which can impact the performance of electrolysis cells and the metal purity. Sodium oxide (Na_2O) is the major impurity in SGA, with typical values between 0.3 to 0.5 wt%. Calcium oxide (CaO) is another important impurity with content around 0.001 to 0.04 wt%. Sodium and calcium content needs to be low due to its impact on bath chemistry [20]. Aluminium fluoride (AlF_3) is consumed in great quantities to neutralize the impact of calcium and sodium that enter the process. This consumption of AlF_3 for the neutralization of excess CaO and Na_2O will consequently generate excess bath in pot lines. However, Wijayaratne et al. [21]. concluded that some content of sodium in the calcined alumina improved the strength of the alumina since sodium inhibits α-alumina formation, previously shown to induce a weak, attrition-prone, and macro-porous microstructure. Other important impurities which can be present in the alumina are some oxides such as silicon dioxide (SiO_2), iron oxide (Fe_2O_3) and phosphorus oxide (P_2O_5). Silicon (Si) and Iron (Fe) are electrochemically reduced and affect metal purity. Phosphorus (P) affects current efficiency negatevely and makes metal brittle and porous [14].

Attrition index

This quality refers to the strength of the alumina usually measured by Forsythe-Hertwig technique. It is the change in the 45 μm fraction of an alumina sample after it has been subjected to the test. It serves as an indication of the tendency for alumina particles to be eroded or fractured [22] [23]. Large attrition index is typically for aluminas with an increase in fines fraction due to attrition. This means a weak material.

Surface area

The BET surface is a technique invented by Braunauer, Emmett and Teller based on the calculation of the surface area of particles from physical adsorption of a gas, typically nitrogen, onto the surface of the sample at cryogenic temperatures. During this process, a crystal intergranular network is formed and restructured. Then, the BET surface area is the area of this porous network. BET surface area values are between $5 m^2/g$ for floury aluminas and up to 100 m^2/g for sandy aluminas. This value depends on the type of calcination and temperature

conditions during the Bayer process. Higher BET surface area is usually linked to higher dissolution rates [24] [16] [25].

MOI and LOI

Moisture on ignition (MOI) or adsorbed water, and loss on ignition (LOI) or structural hydroxyl, is the mass loss of the alumina on heating between specified temperatures in an inert atmosphere. The values can be reported as the total loss at 1000 °C. A second option to report these values can be as the loss on heating from 25 °C to 300 °C, MOI $_{(300\ °C)}$ value, combined with the loss on heating between 300 °C and 1000 °C, LOI $_{(1000\ °C)}$ value. The second option give the difference between free and chemisorbed water. It has been reported that high MOI and LOI values help with the dispersion of the alumina during the dissolution process resulting in high dissolution rates. A dramatic increase in dissolution rate was achieved by using aluminas which release volatile in the bath [24] [26] [25]. Moisture content was claimed to be the most influential parameter. However, in some studies the plots for physical properties such as M.O.I. and L.O.I. contents showed a lack of correlation with total dissolution time, for some of the aluminas examined [24].

Porosity and Density

The porosity of alumina may be measured by an absorption test using either water or carbon tetrachloride. However, the porosity does not seem to be a very important measure of the quality of aluminas and therefore is rarely used for alumina specification. Typical values are around 75% [16].

The bulk or apparent density can be determined by the Archimedes technique and is usually around 0.9 and 1.1 g/cm^3. The Archimedes principle states that the buoyant force on a submerged object is equal to the weight of the fluid that is displaced by the object. Bulk density and porosity can be measured of refractory materials using this technique with dry weights, soaked weights and immersed weights in water [27]. The true or real density is usually between 3.7 and 3.8 g/cm^3 for sandy aluminas [2]. The real density and the total porosity can be determined by a pycnometer. First, the alumina should be finely milled to open all its closed porosity. A known weight of this fine powder can then be used to displace liquid within the pycnometer to determine the real volume, and thereby the real density (ISO 5018 and SANS 5902). Total porosity can then be calculated from bulk density and real density (ISO 5016 and BS 1902-308) [27].

2.4.2 Cell conditions

The cell operational variables may have a greater impact on the dissolution process than the structural properties of alumina. Welch [25] showed that the operating conditions in a cell could create up to a thirty-fold increase in the alumina dissolution rate.

Bath chemistry

The solubility of the alumina is affected mainly by the change in the content of alumina in the bath and by the change in the acidity in the mixture. The changes in the acidity are mainly related to the changes in the AlF_3 and CaF_2 ratio. A decrease in the dissolution rate of alumina with increasing alumina content in the bath has been shown in several studies [14] [13]. Other investigators have found that dissolution time of the alumina increases by decreasing the mass ratio of NaF and AlF_3, also known as bath ratio [28]. Therefore, special attention is required during cell operations to monitor the excess of AlF_3 added, and to try to keep the alumina content around 2-4 wt%, far from the saturation point [29].

Bath superheat

The temperature difference between the bath temperature and its liquidus temperature at a given bath composition is defined as superheat. An increase in the superheat of the bath has been shown to decrease the dissolution time of the alumina [13] [25]. Superheat mainly influence the dissolution of the crust in the bath given that the dissolution of the crust is a heat limited process.

Turbulence

Electrolyte flows induced by mechanical stirring or gas bubbles, has been shown to increase the dissolution rate of alumina and to improve the dispersion of supplied alumina in the electrolyte and thus improving the heat transfer in existing aggregates and crust [30] [28]. This supports the increase in the dissolution rate of the alumina observed in the industry due to the anodic gases being directed to the central channel of the cells [31].

Feeding

The alumina feeding technology has become more important in the last years. Investigations seeking to improve the feeding method to achieve faster alumina dissolution rates are continuously being carried out. The objective is to achieve a method where all the added alumina effectively reaches and penetrates the electrolyte. The feed rate needs to be slow enough to allow all the alumina to distribute and to be efficiently transported throughout the mixture to ensure the largest possible contact area between the electrolyte and the particle. By this

means the heat is sufficient to quickly melt the frozen crust around each particle. Tessier et al. [32] measured improvement in industrial cell performance in terms of anode effect frequency and power-related cell voltage instability by reducing the alumina feed rate.

2.5 Crust and Sludge

Improvements in the feeding technology have resulted in the implementation of cell designs equipped with automatic point feeders. The alumina is supplied in small doses of about 1 to 2 kilograms. Small additions have been shown to improve the ability of the alumina to dissolve and mix rapidly in the electrolyte after each addition. However, during the feeding, not all alumina is dispersed as free-flowing particles. Part of the alumina will float on the surface and absorb some bath inside. The alumina is also encapsulated by a layer of frozen bath as a consequence of the heat absorbed by the alumina, resulting in the formation of a crust. The thickness of the crust will partly depend on the amount of alumina added, and on the heat absorbed by the alumina. The crust floating on the surface of the bath is commonly known as raft. Further, the melt will penetrate the crust while the frozen layer melts away [33] [34], and fill interparticle and intra-particle channels of the alumina. This will increase the density of the crust resulting in it sinking in the electrolyte [28] [35] [36]. As previously discussed, a phase transformation from gamma to alpha alumina will occur rapidly during the crust formation. As the alpha alumina platelets form and grow, they tend to form an interlocking matrix.

The dissolution time for the crust is longer than for the alumina powder. Heat transfer is the controlling process. Thus, extra heat must be supplied for dissolution and for remelting of the solid bath content inside. The crust may settle towards the bottom of the cell and remain suspended by surface tension in the electrolyte [37], or under the liquid metal pad and form what is commonly known as sludge [2]. Sludge can be described as a viscous two-phase mixture formed by high alpha-containing alumina grains and saturated bath. Studies of sludge formation and composition have shown that it contains primarily alpha alumina, of much larger particle size than the alumina that was fed to the bath [16]. The formation of sludge results in problems with the performance of the cell such as insufficient alumina content in the melt and instabilities in the metal pad.

2.6 Previous studies on alumina dissolution measurements

Although alumina has a high solubility in cryolite based melts, the problem of bringing the alumina feed into solution and the control of its concentration has always been of major concern in the operation of aluminium cells.

Many experimental studies on the dissolution of alumina in cryolite melts have been carried out during the years. These studies have been based on different methods. The methods can be divided in two large groups, in-situ, and ex-situ [38], Table 2.1. Ex-situ methods involve the sampling of bath or crust for later physical and chemical analysis. These analyses usually give more accurate and reliable results than the ones from in-situ measurements. However, longer times for the obtention of the results, lack in reproducibility during the sampling, and obtention of representative samples are some of the problems with the ex-situ measurements.

Table 2.1 Different methods used to study the concentration/dissolution of alumina.

Ex-situ	Sampling and analysis	LECO, oxygen analysis Wet chemistry techniques Optical microscopy Powder X-ray diffraction Particle size determinations Electron Microscopy and Diffraction Pellet/tablet/ agglomerate dissolution
In-situ	Physicochemical	X-ray absorption Temperature monitoring
	Electrochemical	Electromotive force (emf) Critical current Anode overpotential Voltage at anode effect Chronopotentiometry
	Optical	Video recordings

2.6.1 Ex-situ measurements

Oxygen analysis or LECO is one of the standard methods of determining the alumina content in quenched melt samples in a lab scale. The method is based on spectroscopic analysis of CO/CO_2 from carbo-thermally reduced oxygen compounds in the samples, [39]. The instrument is calibrated with a well-known standard material prior to sample characterization.

The rotating disc is one of the most applied techniques for the studies of the dissolution of alumina based on an ex-situ method. The technique is very convenient to determine dissolution rates and be able to compare dissolution behaviour of different aluminas.

The dissolution of sintered alpha alumina using a rotating sintered corundum disc was studied by Thonstad et al. [40]. The dissolution rate was found to have a linear dependency on the angular velocity, in agreement with the Levich equation. From the slope of the curve the diffusion coefficient was calculated to be $1 \cdot 10^{-9} m^2 s^{-1}$. In this study, Thonstad concluded that the dissolution of the alumina in the form of rotating disc could be treated as a mass transfer control process.

The rotating disk technique has also been useful to study the effect of the addition of different components in the dissolution of the alumina. Gerlach and Williams [41], found that the addition of LiF, CaF_2, MgF_2 and Al_2O_3 reduced the dissolution rate of the rotating disc. These results were attributed to the decrease in the alumina solubility with the incorporation of the additives.

2.6.2 In-situ measurements

The sudden drop in temperature in the electrolyte temperature right after the addition of alumina in the melt has also been studied. Several authors have tried to correlate these temperature measurements with alumina dissolution kinetics, [28] [36] [31] [42]. Liu et al. [42] derived a model for alumina single particle dissolution from a study of different temperature calcinated aluminas. Fast dissolution rates were observed when high superheat and fast stirring was applied. These conditions gave large temperature drops. A decrease in the dissolution rate was observe with increasing the alumina concentration.

X-ray studies in transparent laboratory cells has also been performed. Here, the absorption contrast of bulk alumina served for visualizing the degree of alumina dispersion in the melt [33]. Walker performed an experiment where additions of 3.5 wt% of fines grained alumina of 10 μm were performed. The formation of alumina balls floating on the surface of the electrolyte were observed after the addition until the frozen shell was melted after 11 seconds and the bath started to

penetrate into the balls. After 3-4 seconds the alumina started to sink into the melt until it hit the bottom. A slow dissolution was observed when the alumina was resting at the bottom.

Alarie et al. developed a gravimetric method to obtain alumina dissolution kinetics [43]. The method followed the weight of alumina disc samples while immersed into a crucible containing up to 10-14 kg of a cryolitic bath at 967 °C. Then, from the weight over time curve, it was possible to recorded and analyzed the forces acting on the alumina samples to determine the dissolution rate. The gravimetric method was compared to a geometric method, measuring the displacement of the sample boundary and to the total weight loss of the samples during the dissolution. In addition, a CFD model to analyze the alumina dissolution in the experiments was built with an axisymmetric laminar flow model centered on the rotational axe of a pure alumina disc with heated sidewalls of the crucible. The experimental results were usually in agreement with the predictions of the CFD model. The global dissolution flux had a mean value around 620 mg/m^2 s. The investigators found that this result represented a case where the heat losses were prevented but not avoided in the experimental setup. The also confirmed that the convection around the sample was controlled both by thermal and concentration effects.

Electrochemical studies

One of the most widely used electrochemical technique to measure the concentration of alumina in the mixture is the critical current density (CCD), perhaps due to its advantages such as robustness and an acceptable accuracy in its measurements [38].This potential-sweep method can study the occurrence of the anode effect on graphite electrodes in cryolite-alumina melts. One of the first scientists to use this technique was Piontelli [44], who suggested that the CCD was proportional to the square root of the concentration of alumina. Thonstad [45] measured the CCD as a function of the concentration of alumina from 1 wt% to 8 wt% alumina in the melt. They concluded that the process prior to the anode effect was diffusion-controlled and that the anode effect occurs when the concentration of alumina approaches zero at the surface of the anode.

Thonstad et al. [46] studied the dissolution of alumina as a function of time using chronopotentiometry analysis. The experiments were performed in a closed furnace under nitrogen atmosphere using a graphite electrode inside a cryolite melt. Potential-time diagrams were obtained with successive anodic constant current pulses larger than the limiting current (i_L) applied on the electrode and the time until a rapid increase in the voltage occurs was recorded. According to the theory, this time is proportional to the square of the concentration of alumina. In the voltage-time diagrams it was observed that no change occurred in the first

second of every addition of alumina, and then the concentration of alumina increased in the following 5 to 6 seconds. However, they reported that the use of this method was hampered at high rate and could not yield reproducible data.

Kuschel and Welch [47] tried to develop an apparatus to measure the dissolution behaviour of the alumina in the melt. The apparatus combined three different techniques, electroanalytical measurements, thermal analysis, and visual observations of the dissolution of the alumina. The experiments were carried out in a crucible with approximately 1kg of electrolyte. The set-up was formed by a stirrer to vary the flow rate of the electrolyte, a fiber-optic cable for the video recordings, a thermocouple, and an electrode to measure the dissolved oxide concentrations. The electrochemical measurements were done using a modification of single sweep cyclic voltammetry, using the relationship between the alumina concentration, critical current density, and the voltage which the electrode had the anode effect. The electrode was cycled every second with a forward sweep rate of 20 mV s^{-1} and a faster sweep rate in the reverse direction. A specific resting potential was used to ensure that the dissolved metals were always oxidized to avoid interactions with the electrode. Variations of about 10% in the accuracy were found but they could be filtered out by performing Fourier transforms. After measuring the dissolution time of more than 20 different alumina at different operating conditions, they concluded that operating conditions such as fast electrolyte flow, high superheat, and low alumina content had a great influence and favoured the dissolution rate. Some alumina properties such as high volatile content and short flow funnel time were also found to favour the dissolution of the alumina but with lower impact.

Haverkamp and Welch [48] worked in the formulation of two different models to describe the dissolution of alumina in cryolite. The first model stated that the rate of the dissolution depends on the reaction of the breaking of Al-O bond by complexing with fluoro-aluminate species. The model assumed that the mass transport is fast relative to the surface chemical reaction or heat transfer. The second model assumed that the rate was mass transport controlled, so it depended on the diffusion rate of the alumina. These models were compared with experimental data obtained using a modified fast linear sweep voltammetry. The dissolution rate of the alumina was determined by linear sweep voltammetry. It consisted of a cyclic voltage ramp applied between a graphite electrode of 3 mm in diameter and 7 mm in length and the graphite crucible containing the melt, which acted as the counter electrode. A fast forward sweep rate was used at 20 V s^{-1} with a very fast reverse sweep at 200 V s^{-1} until the occurrence of the ‘anode effect”. The position of the anode effect was repeatable and increased with alumina concentration and by various correlations the alumina concentration could be determined [49]. A reasonable fit to experimental data was obtained and

the heat transfer and diffusion models appeared to be the best, implying that the mechanism of dissolution might be a combination of both heat transfer and diffusion control.

Welch and Kuschel [25] carried out a study about crust and alumina dissolution measurements with the same method that they used in previous investigations [47]. The study was performed in electrolytes between 0.2 and 0.6 kg and the size of the alumina additions were 1 wt%. They found that the first seconds after the addition of the alumina were characterized by a good dispersion of the alumina and a rapid dissolution. However, during the dissolution process, some of the alumina tended to form aggregates and underwent exothermic phase transitions. In other instances, freezing and clump formations were observed resulting in slower dissolution times. They summarized the impact of some cell conditions and electrolyte variables not only based on this study but also on other complementary studies that used similar equipment and laboratory studies. Most of the results that they found confirmed what they reported in 1990 [47]. However, they also studied the impact of the fines content on the dissolution. They found a close relationship between the fines content and the flow funnel time. At high fines content the alumina flow became slow and inconsistent, leading to clumping and aggregation and subsequently poor dissolution. Another important aspect reported was the importance of the feeder design. For a fast dissolution, it was important to have a steady, dispersing flow, rather than a rapid one, which could lead to clumping of the alumina.

Vasyunina et al. [50] obtained the dissolution rate of different alumina in acidic cryolite melts with different molar ratios of NaF and AlF_3, also known as cryolite ratio (CR). The study was based on measurements of equilibrium electromotive force on a concentration galvanic cell conformed by cryolite/alumina/AlF_3 melt and two platinum electrodes. They performed additions of alumina doses into the electrolyte until saturation. The dissolution process was monitored by the emf measurements. Electrolyte samples were also taken to analyse the concentration of alumina in it. The dissolution rate of the alumina was found by plotting the dependence of the emf measurements with time. From emf measurements plots, they identified different responses which they associated to the addition of the alumina, the formation of agglomerates, and the sinking of the agglomerates into the melt. From the emf measurements they confirmed that the dissolution of the alumina occurred in two stages. The first stage was fast, which they associated with the abrupt decrease in the potential observed in the emf measurements, and then a slow second stage associated with the dissolution of agglomerates. Further, it was found a decrease in the solubility of the alumina with the increase of the acidity of the melt. Moreover, they reported that the dissolution rate depended on

the content of alumina in the melt, meaning that the limiting stages were the heat and mass transfer, associated with the formation and remelting of agglomerates.

More recently, Nikolaev et al. [51] studied the dissolution of the alumina with an electrochemical sensor based on a voltammetric technique based on the measurements of current peak values. The sensor consisted of a glassy carbon working electrode and a copper counter electrode. They studied the alumina dissolution process in cryolite melts with a CR of 2.1, 5 wt% of CaF2 and alumina. The alumina concentration was varied from 0.7 to 4.5 wt%. They found dissolution rates from 0.02 mol s^{-1} to 0.35 mol s^{-1} depending on the initial concentration of alumina in the melt. They reported that it was the first time to use a copper electrode as a cathode, which forms an alloy with the deposited aluminium. They reported that this avoids the measuring error associated with the depolarizing effect of dissolved alumina.

Pershin et al. [52] tried to demonstrate the possibility to use a non-destructive method to control the concentration of alumina during electrolysis. In their study, a cyclic voltammetry technique and LECO analysis was implemented. The measurements were performed using a carbon glass working electrode, a CO/CO_2 gas reference electrode, and a graphite counter electrode inside a $KF\text{-}AlF_3\text{-}Al_2O_3$ melt at 785°C. The electrochemical technique was based in the measurement of the current response peak as a function of the potential scan rate, the dissolution time of the alumina sample and the alumina content in the melt. They obtained different voltammograms recorded for the $KF\text{-}ALF_3$ varying alumina content. They observed that the current response peak increased linearly with the alumina content in the melt. With this result they proposed to use the empirical dependence as a tool for operating non-destructive control of the alumina content during electrolysis in the $KF–AlF_3–Al_2O_3$ melts. They concluded that it might be possible to control and determine the dynamics of changes in the alumina content and, hence, the correctness of operation of alumina automatic feeding to a cell.

Optical observations

Haupin [53] was one of the first researcher who used a see-through cell to observe different phenomena inside the cryolite melt during the process of electrolysis. Haupin worked in a see-through oven with different crucibles made of quartz and sapphire to contain the melt. He observed the electrolyte circulation and gas bubbles prior to, during and after electrolysis and the anode effect when the alumina was decreasing during the process of electrolysis. In addition, he reported hydrogen bubbles and a violet metal mist originated from the cathode.

Due to the high cost of the quartz cells, high temperatures and corrosive environments in the molten salts, and design limitations such as short lifetime of

the cell, and opacity of the cell because of the metal fog and fumes from the electrolyte, important improvements in the design of the cell have been achieve in the last years. To avoid small viewing problems obtained with the use of sapphire window in the crucibles, Qiu et al. [54] used a square-shaped quartz crucible for better viewing of some important phenomena during electrolysis such as metal fog, anode effect and alumina dissolution. Years later, Qiu made other improvements in the transparent cell design using double-chamber crucibles by positioning a square-shaped quartz tube inside the quartz crucible. Further improvements in the cell were done later. They implemented two chambers in one quartz crucible with a slot at the bottom of the middle wall connecting the two chambers. One of the advantages obtained with this design was the isolation of the metal fog in one of the chambers and have a clear view in the other one. In 2015, Northeastern University designed a new transparent cell with a new viewing window at the bottom of furnace [55]. With this improvement they could see the alumina that remained in the bottom of the crucible and other phenomena such as bubble behaviour.

Yang et al. [13] studied the dissolution of alumina in more than 11 different alumina samples from several commercial smelters. A quartz crucible with 200 gr of cryolite was placed inside a see-through oven and additions of 1 wt% of alumina were performed. The dissolution time for every alumina addition was recorded to compare the dissolution rate of the different alumina samples and the dependence on bath chemistry. No electrolysis or physical stirring was applied. The particle size distribution and some properties such as MOI, LOI and BET were presented. They reported that the dissolution rate of the alumina was initially constant and independent of the alumina concentration in the melt until 3 wt% of alumina, suggesting that the rate controlling step for alumina dissolution was a chemical reaction. For melts with high alumina concentrations, typically above 3 wt%, the dissolution rate was dependent on the alumina content, suggesting a diffusion-controlled process. He also reported that the dissolution rate was highly linked to the operating temperature and alumina solubility rather than the electrolyte superheat and minor changes of bath compositions. He further mentioned that alumina properties like high LOI and BET surface area could also facilitate the dissolution rate of the alumina. In another study, Yang et al. [56] observed that crust formation was favoured with melts with high alumina concentrations low temperatures, and poor convection. They also concluded that stirring of the melt facilitate the heat transfer and the diffusion of the alumina in the electrolyte, leading to a much faster dissolution.

Gao et al. [57] studied the dissolution behaviour of alumina and the mechanism for alumina dissolution under the influences of bath chemistry and temperature using a transparent cell. The study included a comparison of the dissolution

characteristics between primary and secondary alumina, the influence of some physical-chemical properties on the dissolution rate and some dynamic studies on the crust dissolution. They also presented some industrial measurement campaigns of alumina concentration in 410 kA and 500 kA cells to investigate the spatial effect and bath chemistry on alumina control in high amperage cells.
The dissolution experiments for primary and secondary alumina were conducted under static bath flow in a no-stirred cryolite melt with composition 2.4NaF-AlF_3-5%LiF-4%CaF_2 at 955 °C. The pictures of the dissolution process for the primary alumina revealed a fast dissolution process the first 20 seconds. This was followed by the formation of a layer of boat-like agglomerates with a dimension of 55 mm x 55 mm x 0.5 mm with a floating time of around 2 minutes. Then, the sinking of the crust was observed and the whole dissolution process was completed after 600 seconds. On the contrary, during the addition of secondary alumina, the powder was observed to rapidly dispersed into the melt in the forms of particles and fine fragments. The dissolution time was reported to last around 113 seconds and no crust formation was observed. The disappearance of agglomerates was attributed to the damage of the connection formed between alumina particles on the surface of the bath. Gao et al. believed that carbon trapped in the secondary alumina burned as soon as it reached the surface of molten electrolyte, generating heat and reducing the temperature difference between the cold alumina and the bath. They also reported that the carbon dioxide generated could serve as an agitator helping the alumina to break in small particles, causing a larger contact area and wetting with the melt, resulting in a faster dissolution. Moreover, from the alumina dissolution measurements in the industrial cells they found that factors such as bath super heat in the rage of 8-12°C and high alumina particle size with low impurities enable better alumina concentration control and more uniform concentration distribution.

References

[1] T. Brown, N. Idoine, C. Wrighton, S. Hobbs, R. Shaw, P. Everett, E. Deady and C. Kresse, "World Mineral Production 2015-19," *British Geological Survey,* 2019.

[2] J. Thonstad, P. Fellner, G. Haarberg, J. Hives, H. Kvande and A. Sterten, Aluminium Elctrolysis. Fundamentals of the Hall-Heroult Process, Dusseldorf: Aluminium-Verlag, 2001.

[3] J. Thonstad, "On The Anode Gas Reactions in Aluminium Electrolysis II," *Journal of The Electrochemical Society,* vol. 111, no. 8, pp. 959-965, 1964.

[4] G. Tarcy, H. Kvande and A. Tabereaux, "Advancing the Industrial Aluminum Process: 20th Century Breackthrough Inventions and Developments," *JOM,* pp. 101-108, 2011.

[5] R. Zhou and R. Snyder, "Structures and Transformation Mechanism of the Transition Aluminas," *Acta Cryst,* vol. B47, pp. 617-630, 1991.

[6] D. Townsed and L. Boxall, "Crusting Behavior of Smelter Aluminas," *Light Metals,* pp. 649-665, 1984.

[7] O. Asbjørnsen and J. Andersen, "Kinetics and Trasnport Procesess in the Disslution of Aluminium Oxide in Cryolite Melts," *Light Metals,* vol. 1, pp. 137-152, 1977.

[8] R. Hovland, R. Rolseth and A. Solheim, "On the Alumina Dissolution in Cryolite Melts," in *Proceedings of the International Sympsium on Light Metals Processing and Applications*, Quebec city, 1993.

[9] Å. Stern, *Electrochim. Acta,* vol. 25, pp. 1675-1677, 1980.

[10] R. Ødegård, S. Rønning and J. Thonstad, "On Alumina Phase Transformation and Crust Formation in Aluminium Cells," *Light Metals,* pp. 695-709, 1985.

[11] P. Laovie, M. Taylor and J. Metson, "A Review of Alumina Feeding and Dissolution Factors in Aluminium Reduction Cells," *Metallurgical and Materials Transactions B,* vol. 47, no. B, pp. 2690-2696, 2016.

[12] X. Wang, “Alumina Dissolution in Aluminum Smelting Electrolyte,” *Light Metals,* pp. 383-388, 2009.

[13] Y. Yang, B. Gao, Z. Wang, Z. Shi and X. Hu, “Effect of Physiochemical Properties and Bath Chemistry on Alumina Dissolution Rate in Cryolite Electrolyte,” *The Minerals, Metals & Materials Society,* vol. 67, no. 5, pp. 973-983, 2015.

[14] R. Jain, S. Trickleback and B. Welch, “Interaction of Aluminas with Aluminium Smelting Electrolytes,” *Light Metals,* pp. 609-622, 1983.

[15] L. Isaeva, A. Braslavskii and P. Polyakov, “Effect of the Content of the a-Phase and Granulometric Composition on the Dissolution Rate of Alumina in Cryolite–Alumina Melts,” *Russian Journal of Non-Ferrous Metals,* vol. 50, no. 6, pp. 600-605, 2009.

[16] K. Grotheim and H. Kvande, Introduction to Aluminium Electrolysis. Understanding the Hall-Heroult Process, Dusseldorf: Aluminium-Verlag, 1993.

[17] S. Lindsay, “Key Physical Properties of Smelter Grade Alumina,” *Light Metals,* pp. 597-601, 2014.

[18] B. Lillebuen, “Alumina,” in *Proceedings of the 2009 International Course on Process Metallurgy of Aluminium*, Trondheim, 2009.

[19] A. Johnson, “Alumina Crusting and Dissolution in Molten Electrolyte,” *JOM,* vol. 34, pp. 63-68, 1982.

[20] S. Lindsay, “Customer Impacts of Na2O and CaO in Smelter Grade Alumina,” *Light Metals,* pp. 163-167, 2012.

[21] H. Wijayaratne, M. Hyland, L. Perander and J. Metson, “Balancing Sodium Impurities in Alumina for Improved Properties,” *The Minerals, Metals & Materials Society and ASM International,* vol. 49B, pp. 2809-2820, 2018.

[22] J. Sang, “Factors Affecting the Attrition Strength of Alumina Products,” *Essential Readings Light Metals,* pp. 740-746, 2013.

[23] Y. Yang, B. Gao, Z. Wang , Z. Shi and X. Hu, “Study on the Dissolution of Alumina in Cryolite Electrolyte Using the See-Through Cell,” *Light Metals,* pp. 583-588, 2015.

[24] A. Bagshaw and B. Welch, “THe Influence of Alumina Properties on Its Dissolution in Smelting Electrolyte,” *Light Metals,* pp. 783-787, 1986.

[25] B. Welch and G. Kuschel, “Crust and Alumina Powder Dissolution in Aluminium Smelting Electrolytes,” *JOM,* vol. 59, no. 5, p. 50, 2007.

[26] T. Johnston and N. Richards, “Correlation between alumina properties and crust,” *Light Metals,* p. 623–639, 1983.

[27] B. Berger , “The Southern African Institute of Mining and Metallurgy Refractories 2010 Conference,” 2010.

[28] G. Kuschel and B. Welch, “Further Studies of Alumina Dissolution Under Conditions Similar to Cell Operations,” *Light Metals,* pp. 299-305, 1991.

[29] W. Li, X. Chen, S. Qiu and B. Zhang, *Light Metals,* pp. 893-898, 2013.

[30] O. Kobbeltvedt and B. Moxnes, “On The Bath Flow, Alumina Distribution and Anode Gas Release in Aluminium Cells,” *Light Metals,* pp. 257-264, 1997.

[31] S. Lindsay, “Key Physical Properties of Smelter Grade Alumina,” *Light Metals,* pp. 597-601, 2014.

[32] J. Tessier, G. Tarcy, E. Batista, X. Wang and P. Doiron, “Improvement of Alumina Dissolution Rate Through Alumina Feeder Pipe,” *Light Metals,* pp. 711-717, 2013.

[33] D. Walker, “Alumina in Aluminium Smelting and its Behaviour After Addition to Cryolite-Based Electrolytes,” in *PhD thesis*, University of Toronto, 1993.

[34] D. Walker, T. Utigard and W. Taylor, “Alumina Agglomerates in Aluminium Smelters,” *Light Metals,* pp. 425-434, 1995.

[35] H. Maeda, S. Matsui and A. Era, “Measurement of Dissolution Rate of Alumina in Cryolite Melt,” *Light Metals,* pp. 763-780, 1985.

[36] O. Kobbeltvedt, “Dissolution Kinetics for Alumina in Cryolite Melts. Distribution of Alumina in the Electrolyte of Industrial Aluminium Cells,” in *PhD Thesis*, NTNU, 1997.

[37] A. Solheim and S. Rolseth, “Some Surface and Interfacial Phenomena Encountered in Aluminium Electrolysis,” *Light Metals,* pp. 469-474, 2001.

[38] N. Richards, S. Rolseth, J. Thonstad and R. Haverkamp, “Electrochemical Analysis of Alumina Dissolved in Cryolite Melts,” *Light Metals,* pp. 391-404, 1995.

[39] S. Rolseth, R. Hovland and O. Kobbeltvedt, “Alumina Agglomeration and Dissolution in Cryolite Melts,” *Light Metals,* pp. 351-357, 1994.

[40] J. Thonstad, A. Solheim, S. Rolseth and O. Skar, “The Dissolution of Alumina in Cryolite Melts,” *Light Metals,* pp. 105-111, 1988.

[41] J. Gerlach and G. Wickhaus, *Light Metals,* pp. 301-313, 1985.

[42] X. Liu, S. George and V. Wills, “Effect of Alumina Phase Structure on its Dissolution in Cryolite Melt,” in *Third International Alumina Quality Workshop*, Hunter Valley, Australia, 1993.

[43] J. Alarie, T. Roger, L. Kiss, S. Poncsák and S. Guérard, “Validation of the Gravimetric Method to Properly Follow Alumina Dissolution in Cryolitic Bath,” *Light Metals,* pp. 680-687, 2020.

[44] R. Piontelli, B. Mazza and P. Pedeferri, *Electrochem. Acta,* vol. 10, p. 1117, 1963.

[45] J. Thonstad, “Critical Current Densities in Cryolite-Alumina Melts,” *Electrochemica Acta,* vol. 12, pp. 1219-1226, 1967.

[46] J. Thonstad, F. Nordmo and J. Paulsen, “Dissolution of Alumina in Molten Cryolite,” *Metallurgical Transactions,* vol. 3, pp. 403-408, 1972.

[47] G. Kuschel and B. Welch, Effect of Alumina Properties and Operation of Smelting Cells on the Dissolution Behaviour of Alumina, University of Auckland, New Zeland: PhD thesis, 1990.

[48] R. Haverkamp and B. Welch, “Modelling the Dissolution of Alumina Powder in Cryolite,” *Chemical Engineering and Processing,* vol. 37, pp. 177-187, 1998.

[49] R. Haverkamp, B. Welch and J. Metson, “An Electrochemical Method for Measuring the Dissolution Rate of Alumina in Molten Cryolite,” *Bull. Electrichem.,* vol. 8, no. 7, pp. 334-340, 1992.

[50] N. Vasyunina, I. Vasyunina, Y. Mikhalev and A. Vinogradov, “The Solubility and Dissolution Rate of Alumina in Acidic Cryolite Aluminous Melts,” *Metallurgy of Non-Ferrous Metals,* vol. 50, no. 4, pp. 338-342, 2009.

[51] A. Nikolaev, O. Pavlenko, A. Suzdaltsev and Y. Zaikov, “Electrochemical Sensor for Monitoring the Alumina Dissolution and Concentration in a Cryolite-Alumina Melt,” *Journal of The Electrochemical Society,* vol. 167, no. 126511, 2020.

[52] P. Pershin , A. Suzdaltsev and P. Zaikov, “Dissolution of Al2O3 in KF-ALF3,” *Russian Metallurgy,* vol. 2021, no. 2, pp. 213-218, 2021.

[53] W. Haupin, “See-Through Hall-Heroult Cell,” *Light Metals,* pp. 234-239, 1974.

[54] Z. Qiu, L. Fan, K. Grjotheim and H. Kvande, *Journal of Applied Electrochemistry,* vol. 17, no. 4, pp. 707-714, 1987.

[55] Z. Zhao, Z. Wang, B. Gao, Y. Feng, Z. Shi and X. Hu, “Anodic Bubble Behavior and Voltage Drop in a Laboratory Transparent Aluminium Electrolytic Cell,” *Metallurgical and Materials Transactions B,* vol. 47B, pp. 1962-1975, 2016.

[56] Y. Yang, B. Gao, Z. Wang, Z. Shi and X. Hu, “The Formation and Dissolution of Crust Upon Alumina Addition into Cryolite Electrolyte,” *The Minerals, Metals & Materials Society,* vol. 67, no. 9, pp. 2170-2180, 2015.

[57] B. Gao, Q. Feng and Z. Wang, “The Alumina Dissolution in Industrial Aluminium Cells,” *Journal of Siberian Federal University. Engineering & Technologies,* vol. 11, no. 4, pp. 376-386, 2018.

Chapter 3 Experimental: Development of the sensor and see-through oven

This chapter describes and summarizes the different setups and conditions used during the investigation. Even though, there is some overlap with the description in each chapter, this chapter illustrates the overall development of the sensor and the see-through experiments throughout the project as well as the challenges faced during the investigation. Moreover, the chapter briefly presents some of the results to help understand the reason for the choice of the experimental procedure, parameters and conditions used in each chapter. However, the results will be presented in its entirety in each of the chapters.

The present work started from the ground up with different designsand construction of a graphite probe, a graphite quasi-reference electrode and an aluminium reference electrode. This is the first reported alumina sensor composed of a graphite probe for emf-based in-situ alumina concentration measurements. Nor has a graphite quasi-reference electrode has been reported before. A great part of the work was aimed to the conduction of experiments to understand the behaviour of the sensor, and to find the right parameters in the setup. These experiments to understand the behaviour of the sensor were mainly conducted in a sealed furnace under nitrogen gas.

The planning and carrying out of experiments in a see-through oven were also part of the project. The aim of these experiments was to perform alumina sensor measurements and video recordings during the dissolution of the alumina in a transparent quartz crucible. The project started with the design and construction of some parts of the oven such as a metal lid, quartz crucibles, and quartz windows, as well as the design and building of the cooling and gas system of the furnace. Then, the project continued with the finding of a right camera and parameters to obtain the best quality in the videos during the experiments. In addition, the see-through oven being a not tight oven, the experiments were carried out in different conditions than the ones used in the sealed furnace. Thus, a new design of the alumina sensor, a new set-up, and new parameters for the performing of the experiments were made.

3.1 Development of the sensor and understanding of its behaviour

Initially, the investigation was focused on understanding the behaviour and the performance of the sensor. The purpose was to look at the emf measurements and identify the response of the sensor to the changes of alumina concentration in the cryolite melt. This part of the research was challenging since the system inside the furnace was very complex with generation of gases inside and above the bath. Thus, some experiments were carried out with the intention to differentiate the response of the sensor to the changes of alumina from the response of the sensor to the generation of gases. The experiments studying this part of the research are presented in chapter 4.

3.1.1 Chapter 4: Alumina concentration measurements in cryolite melts

The first experiments were performed in a sealed vertical furnace. The details of the set-up are presented in Figure 3.1 and Figure 3.2 . A carbon crucible (Ø 85 mm, h 130 mm) containing synthetic cryolite (500 g) was placed inside the furnace. The synthetic cryolite was used as received from Sigma-Aldrich and the composition was 99 wt% cryolite and 1 wt% alumina. The furnace was heated until the bath melted. The theoretical liquidus temperature at this bath composition is around 1000 °C. However, during these experiments, the thermocouple measured temperatures around 975 °C inside the melt. This means that the temperature measurements had some deviations or that some impurities were present in the synthetic cryolite. Experiments were done under N_2 gas. The electrodes and the thermocouple were placed inside the melt and fixed in the lid of the furnace with rubber plugs. Emf measurements between the graphite probe and the two reference electrodes were performed during the addition of alumina and throughout the entire dissolution process. A logger (Keithley 2000 multimeter) was used to acquire the emf data and temperature.

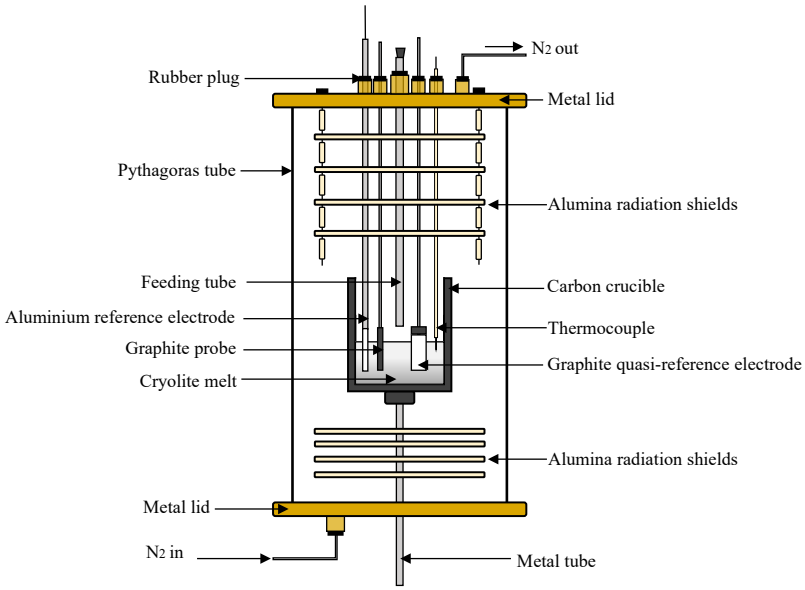

Figure 3.1 Sketch of the setup used for the sealed oven.

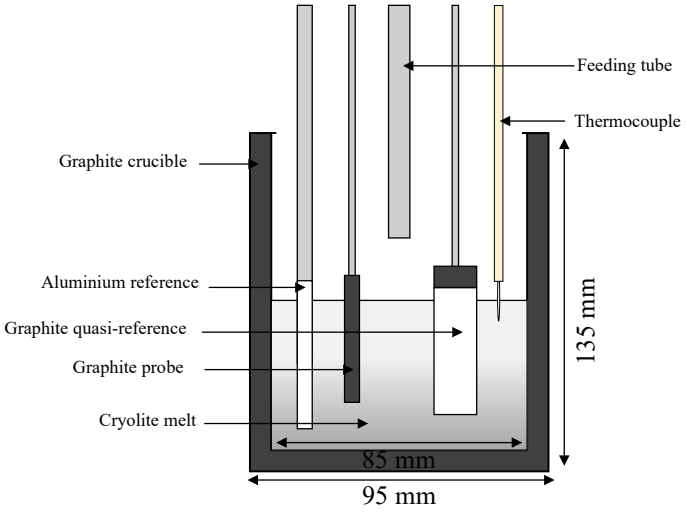

Figure 3.2 Sketch of the cell. From left to right: aluminium reference electrode, graphite probe, feeding tube, graphite quasi-reference electrode and the thermocouple.

Design of the graphite probe

The first design of the graphite probe, also referred as the alumina probe is shown in Figure 3.3 a . The electrode is a graphite rod (Ø 10 mm, h 60 mm). A stainless-steel rod connector bar (h 500 mm) was screwed to the graphite rod. The graphite electrode was made of the same carbon material as the graphite rod used in the graphite quasi-reference electrode.

Design of the graphite quasi-reference electrode

The first design of the graphite quasi-reference electrode is shown in Figure 3.3 b. A carbon rod (Ø 5 mm, h 50 mm) was screwed to a graphite connector and placed inside a boron nitride tube ($Ø_{inner}$ 10 mm, $Ø_{outer}$ 22 mm, h 80 mm). A hole (Ø 1.5 mm) was drilled above the bottom of the tube to ensure ionic contact between the alumina saturated bath inside the tube and the bath in the crucible. A stainless-steel rod connector bar (h 500 mm) was screwed to the graphite connector. Alumina powder (3 g) was added inside the boron nitride tube to make an alumina saturated bath (10-12 wt% alumina).

Design of the aluminium reference electrode

An illustration of the aluminium reference electrode is shown in Figure 3.3 c. A boron nitride tube ($Ø_{inner}$ 5 mm, $Ø_{outer}$ 10 mm, h 70 mm) was threaded to a stainless-steel tube. Pure aluminium (0.65 g) was added inside the boron nitride tube. A hole was drilled above the metal surface to allow bath to enter the tube. A tungsten wire in contact with the molten aluminium was used for electrical contact. The wire was shielded with an alumina tube to hinder the contact between the wire and the bath inside the boron nitride tube. The alumina tube ensured saturation of the bath inside the boron nitride tube. Pictures of the probe and electrodes are also shown in the appendices Figure A1.

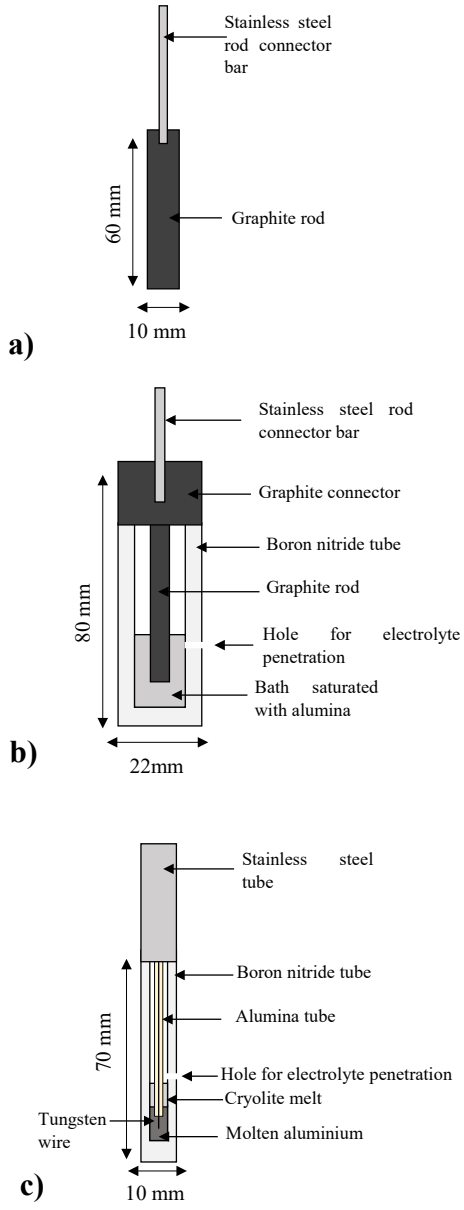

Figure 3.3 Sketch of the **a)** graphite probe, **b)** the graphite quasi-reference electrode, and **c)** the aluminium reference electrode.

Alumina feeding

Subsequent additions of 3 wt% of primary alumina were performed using a stainless-steel feeding tube (Ø inner 15 mm, h 300 mm). The tube was placed approximately 2 cm above the melt. The feeding was carried out by removing the plug from the tube and adding the alumina dose with a glass funnel from the top of the oven. The feeding procedure took between 8 to 10 seconds from the moment that the plug was removed until the plug was again inserted on the feeding tube when the addition was completed, Figure 3.4.

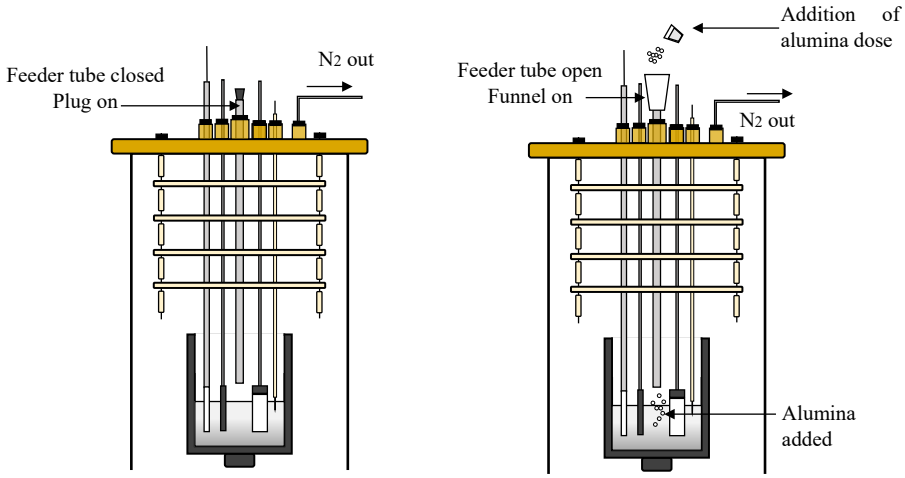

a) Closed oven/ N_2 atmosphere **b)** Open oven/ N_2 + ambient air

Figure 3.4 Sketch of the procedure for the addition of alumina. **a)** closed oven. **b)** open oven.

Nitrogen was normally the gas flowing through the furnace during experiments. When a plug in the lid was opened, air could enter the furnace. The measurements were strongly affected during such an operation showing an increase in the potential. The reactions shown in Equations (3.1), (3.2) and (3.3) might explain how the oxygen from the ambient could alter the partial pressures of CO and CO_2 in the cell and cause an increase in the potential.

$$C_{(probe,crucible)} + O_{2(gas)} = CO_{2(gas)} \quad (3.1)$$

$$C_{(probe,crucible)} + O_{2(gas)} = 2CO_{(gas)} \quad (3.2)$$

$$2CO_{(gas)} + O_{2(gas)} = 2CO_{2(gas)} \quad (3.3)$$

To understand this phenomenon some control experiments were performed. Substitution of N_2 by CO_2 was done to study the influence of having a gas composition rich in CO_2 above the melt. The sketch of the experimental setup is shown in Figure 3.5. It was observed that when CO_2 gas was flushed into the oven the emf measurements were not affected by the removal of the rubber plugs and no variations in the potential were observed. The results can be seen in chapter 4.

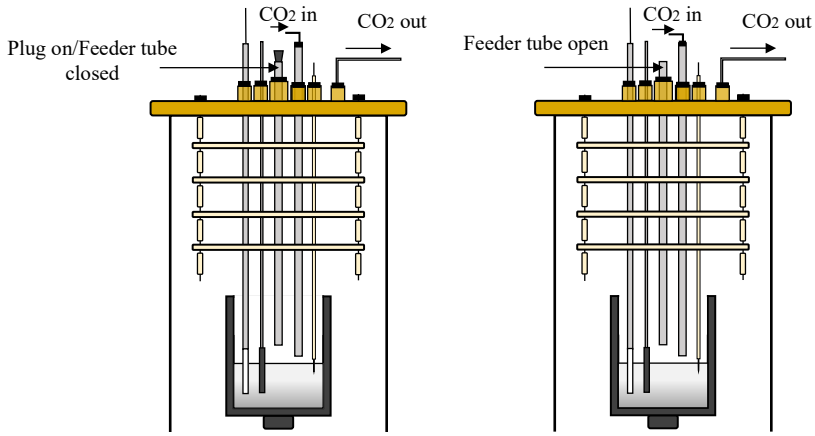

a) Closed oven/ CO_2 atmosphere **b)** Open oven/ CO_2 atmosphere

Figure 3.5 Set-up to study the influence on the potential of exposure of the cell to atmosphere when the gas composition above the melt was CO_2. **a)** Closed oven. b) Open oven

A constant flow of CO_2 into the cell was believed to prevent large variations in the partial pressures of CO and CO_2. The added CO_2 could establish a buffer system with respect to small amounts of air entering the cell.

Due to the response of the sensor to the gases above the melt, the design of the graphite or alumina probe was changed. The second design of the probe had a boron nitride shield (Ø 15 mm, h 20 mm) on top of the graphite rod (Ø 10 mm, h 40 mm), Figure 3.6. The purpose of the shielding was to hinder the reaction with air possibly presented above the melt and to prevent the carbon to be in contact

with the crust after feeding. Figure 3.7 shows a comparison between the two probe designs.

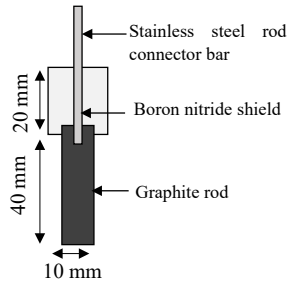

Figure 3.6 Sketch of the design of the graphite or alumina probe shielded with boron nitride.

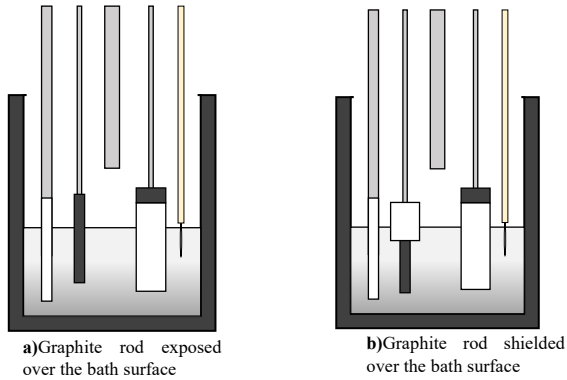

Figure 3.7 a): first design of the probe with the graphite rod partially immersed in the bath. **b)**: second design of the probe with the graphite rod totally immersed in the bath.

To further investigate the behaviour of the sensor, a control experiment with additions of alumina without opening the furnace were performed. The alumina was placed inside a chamber which was connected to the alumina feeding tube. The system was completely sealed under nitrogen gas and the additions were performed without removing the rubber plug of the feeding tube, Figure 3.8. During the experiment, the inlet N_2 gas flow was set at 500 mL/min. The out gas was connected to a gas trap. At this gas flow, a frequency of one bubble per second

was observed inside the gas trap. Right after the addition, a vigorously bubbling in the liquid of the gas trap was observed. This phenomenon last approximately 2 seconds, then the frequency of one bubble per second was re-established. During this phenomenon, a jump in the potential which also last few seconds was observed in the emf measurements. At this part of the investigation this result from this control experiment was not fully understood and was not included in chapter 4. However, this result was later analysed and together with data from later experiments, it pointed out that the jumps in the potential observed in some of the experiments might be related with the generation of gas during the additions. The results showing this kind of jump are shown in chapter 4 and chapter 5. More detailed discussions and hypothesis about this phenomenon are presented in chapter 5 and chapter 8.

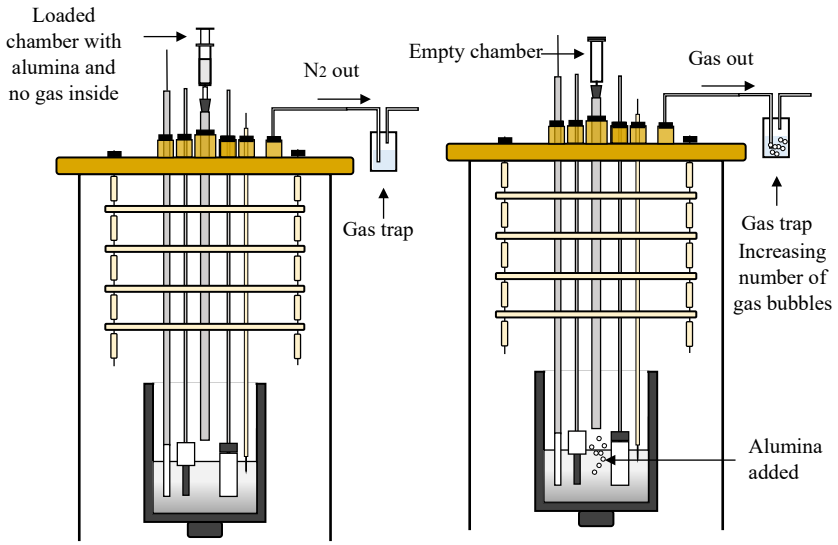

Figure 3.8 Alumina addition in a sealed system under nitrogen atmosphere. **a)** Previous addition. **b)** After addition.

Other results from some experiments showed that some of the major problems during the sensor measurements were due to magnetic and electrical issues. These issues were observed as noise or dramatic changes in the emf measurements. One

of the reasons for these problems was the electromagnetic field induced by the heating elements of the oven to the electrodes and cables connected to the multimeter. In order to solve these problems, all the cables were shielded and properly connected to earth to avoid electromagnetic or electrical interference. The Keithley 2000 multimeter was changed to a Data Acquisition (DAQ) measurement hardware (NI 9205). A new software (NI Flexlogger) with the option to monitor simultaneously the emf and the temperature through real time graphs/curves was used. This new software allowed the observation of any unusual change in the system and faster detection of any problem during the experiments. Finally, the sealed furnace was changed to a see-through oven with a different distribution of the heating elements where the voltage measurements were less affected by the noise from electromagnetic interference

3.2 Development of the see-through experiments

The assembly of the see-through oven was done to perform video recordings during the dissolution of the alumina. Video recordings helped to understand some of the behaviours of the sensor and to gather more information about the dissolution process of the alumina. Pictures of the furnace are shown in appendices Figure A2. The see-through oven was used in chapter 4, 5 and 6.

3.2.1 Chapter 5: Dissolution characteristics and concentration measurements of alumina in cryolite melts

The first challenge faced in the see-through oven was to find the right operational temperature during the experiments. In the first experimental setup, the oven had removable wall plugs on the sides, Figure 3.9. These wall plugs needed to be pulled out from the oven to be able to see inside where the quartz crucible was located. The removing of these wall plugs from the oven resulted in significant heat loss. Thus, temperatures above 1000 °C were needed in the oven to have a high super heat in the melt and prevent the mixture from freezing and from losing transparency when the wall plugs were pulled out. However, these temperatures resulted in negative impact on the lifetime of the quartz crucible and the material inside the oven. Thus, decrease in the operating temperature of the oven was necessary to avoid damage of the materials inside the oven and to prolong the lifetime of the furnace. Therefore, the alumina sensor experiments were done without pulling the plugs off from the oven during the additions of the alumina. However, the emf measurements were performed in the see-through oven because opening of the wall plugs and observation of the cell prior to the addition of

alumina gave better confidence that the positioning of the electrodes and feeding tube was correct.

The emf measurements were carried out with the alumina probe shown in Figure 3.6 and the aluminium reference electrode showed in Figure 3.3. A transparent quartz crucible (Ø 65 mm, height 75 mm) was used to contain 200 g of bath. The initial bath composition was 99 wt% synthetic cryolite and 1 wt% of alumina. The quartz crucible was placed inside the see-through furnace (Entech Energiteknik AB). A pytagoras tube ($Ø_{inner}$ 105 mm, $Ø_{outer}$ 115 mm, h 600 mm) was used to decrease heat losses and protect the heating elements and the oven. Two square holes (95 mm x 95 mm) were made in the pythagoras tube at the same level of the removable wall plugs to be able to observe the cell, Figure A3. Alumina radiation shields (Ø 85 mm, h 5 mm) were placed under and above the quartz crucible to reduce the temperature gradient inside the oven. A metal lid (120 mm x 120 mm), Figure A4, was designed and built. The lid had four holes to insert the electrodes, the feeding tube and the thermocouple. It also had a small hole for the inlet and outlet gas. A ceramic crucible (Ø 85 mm, h 95 mm) was used as a trap to catch leaking of the melt in case the quartz crucible broke. The temperature inside the melt was 980 °C and was monitored with a thermocouple type S (Pt/Pt-Rh). It is believed that the temperature measurements had some deviations or that some impurities were present in the synthetic cryolite. Nitrogen gas was flushed inside the oven during the experiments. However, the see-through furnace was not a sealed furnace even when the wall plugs were on.

Additions of 2 wt% of secondary alumina were performed using a glass funnel on the top of a stainless-steel metal tube (Ø 20 mm, h 400 mm). The emf between the alumina probe and the aluminium reference electrode was measured during the addition of alumina and throughout the entire dissolution process. A DAQ measurement hardware (NI 9205) was used for the emf measurements.

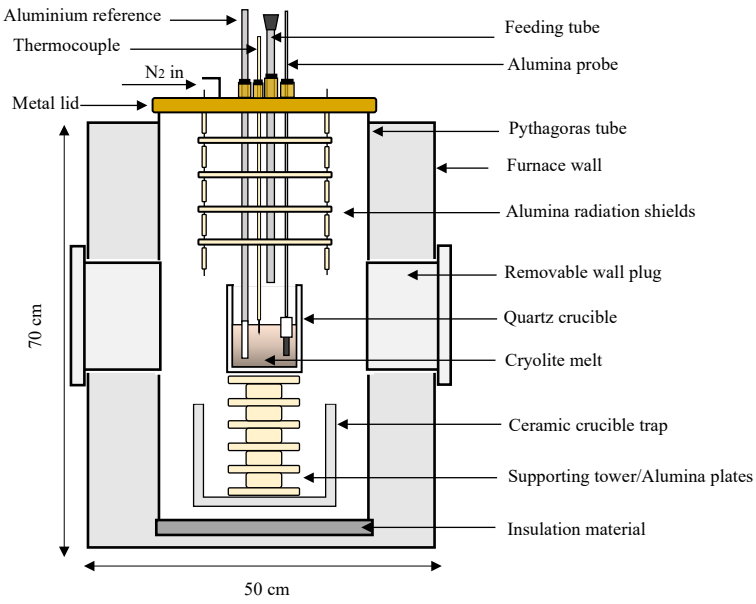

Figure 3.9 Sketch of the experimental setup for the emf measurements performed in a transparent quartz crucible. The cell is placed in the middle of the furnace and contains the melt, the aluminium reference electrode, the thermocouple, and the graphite probe. The alumina feeding tube is inserted from the top.

At this point of the research, the video recordings of the dissolution of alumina were not carried out simultaneously with the emf measurements. In order to perform the video recordings of the dissolution of the alumina the wall plugs had to be pulled off from the oven before the feeding, Figure 3.10. One of the plugs was removed for the camera and the second plug was removed in order decrease the intensity of the light inside the oven and obtain better pictures. Heat losses occurred when the wall plugs were pulled off. Therefore, aluminium fluoride and

calcium fluoride were added to the bath to lower the liquidus temperature and avoid freezing of the melt during the feeding procedure. The initial bath composition was synthetic cryolite (150 g, 75 wt%), aluminium fluoride (30 g, 15 wt%) and calcium fluoride (20 g, 10 wt%). The temperature in the melt was 980 °C. Subsequent additions of 1 wt% of primary and secondary alumina were performed. The video recordings were performed using a high-speed camera (Photron Fastcam Mini AX).

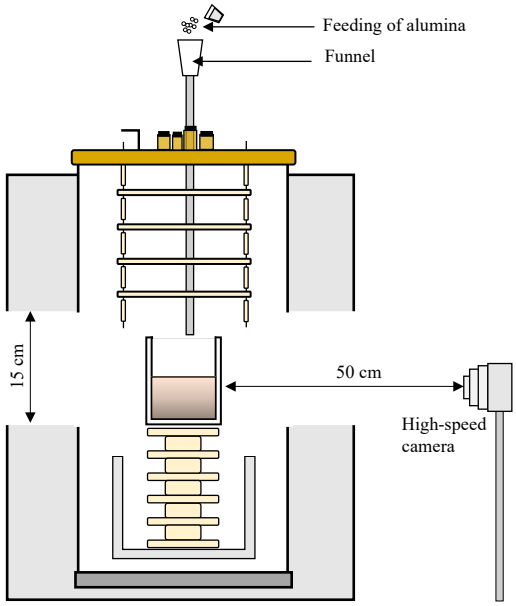

Figure 3.10 Principal sketch of the experimental set up for video recordings performed in a transparent quartz crucible. The high-speed camera is shown on the right Principal sketch of the experimental set up for video recordings performed in a transparent quartz crucible. The high-speed camera is shown on the right.

Another disadvantage of the setup shown in Figure 3.10 was the long distance needed between the camera and the crucible, resulting in a lack of details in the videos. Due to the heat from the oven when the wall plugs were removed, the camera needed to be at least 50 cm away from the crucible to avoid damages in

the lens. Therefore, the two wall plugs were replaced with two square quartz windows, Figure 3.11. The windows blocked part of the heat from the furnace and the camera could be brought closer to the crucible resulting in a better resolution in the videos. However, gasses from the melt were constantly sticking to the windows reducing visibility during the video recordings.

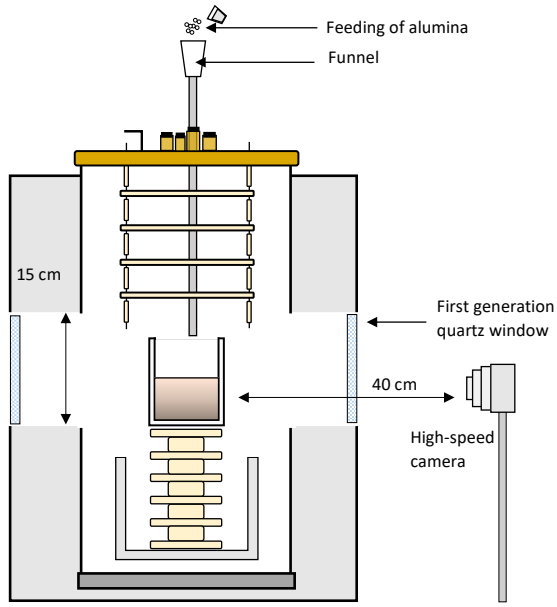

Figure 3.11 Sketch of the experimental setup for video recordings with two transparent quartz windows on the sides.

3.2.2 Chapter 6: Oxide sensor measurements and simultaneous optical observations during dissolution of alumina in cryolite melt

An important change in the design of the graphite reference was needed to be able to use this electrode for emf measurements in the see-through oven. Since the furnace was not completely sealed, the air inside the furnace burnt with the graphite part of the graphite quasi-reference electrode that was above the surface of the melt, generating CO_2 and affecting the sensor measurements. Thus, the new

designed reference electrode was completely shielded with boron nitride as shown on the top of Figure 3.12. The quasi-reference electrode was based on a graphite rod (Ø 0.5 cm, h 5 cm) which was screwed to a graphite connector and put inside a boron nitride tube ($Ø_{inner}$ 10 mm, $Ø_{outer}$ 22 mm, h 118 mm). A hole (Ø 1 mm) was drilled above the bottom of the tube to ensure ionic contact between the alumina saturated bath inside the tube and the bath in the crucible. A stainless-steel rod was screwed to the graphite connector. Alumina powder (2.5 g) was added to the boron nitride tube to make an alumina saturated bath (approximately 8 wt% with the bath composition used in this chapter). A more accurate sketch is shown in Figure A5.

The aluminium reference was also modified to a more robust design to increase the number of successful experiments, as shown in the middle of Figure 3.12. Many of the experiments were not successful due to the failure of the boron nitride tube or misalignment of the tungsten wire inside the boron nitride tube, causing loss of contact with the molten aluminium. The new design had a thicker boron nitride tube which had longer lifetime inside the melt. This new aluminium reference electrode had a thinner channel in the lower part of the boron nitride tube to ensure a higher height in the level of the molten aluminium. This to prevent loss of contact between the tungsten wire and molten aluminium. In addition, the carbon holder on the upper part of the metal tube, fixed the alumina tube and the tungsten wire in a more stable position preventing undesirable movements of the wire which resulted in less noise in the emf measurements. Experiments performed with this new design served just to confirm some of the behaviours of the sensor observed in previous publications. Results with this design are not published. An accurate sketch is shown in Figure A6.

The alumina probe was modified to reduce the noise in the emf measurements. The noise was assumed to arise from the undissolved alumina accumulating under the horizontal part of the graphite rod and gas bubbles in the melt. The rod was therefore protected with a boron nitride tube at the bottom part, bottom of Figure 3.12. The probe was also made thicker for more surface area of the probe possibly evening out local differences at the carbon-melt interface. However, no differences between measurements of the new and old design were observed.

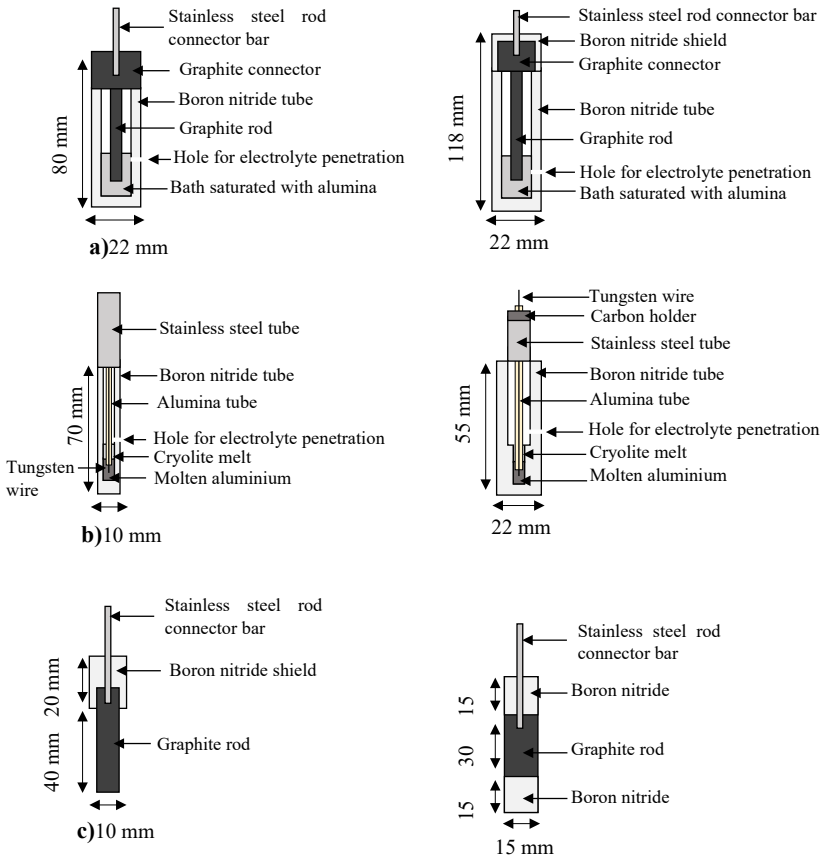

Figure 3.12 Improvement in the design of the electrodes. **a)**: graphite quasi-reference electrode, **b)**: aluminium reference electrode, **c)**: alumina probe.

New designed windows were built to reduce the problems of heat loss from the windows, freezing of the melt and lack of transparency during the video recordings. The new windows were composed of a quartz piece (l 80 mm, h 80 mm, w 4 mm) fitted between two insulation sections. Then a metal plate was used to cover the exterior of the insulation sections to protect them. The windows were fixed to the oven with screws in a system where the windows could be exchanged at any time. The new design permitted the windows to stay fixed to the oven during the whole experiment, and to work with a constant melt temperature. A detailed design of the windows is shown in Figure A7 and Figure A8.

In addition, nitrogen was flushed from both windows (100 mL/min.) through a metal tube (Ø 6 mm) to prevent vapours and particles from sticking to the windows and thereby enhancing the visibility. The diameter of the tunnels of the oven were also reduced to 10 cm to decrease the heat losses. One hole in the lid was kept open to create a flow of gas from the windows to the upper part of the oven. The gas flow brought with it the fumes from the melt preventing it from sticking to the quartz windows, Figure 3.13. No sudden jumps in the potential during the alumina additions of these experiments were observed. This observation might be related with the setup of these experiments. The setup might allow the establishing of a buffer system between the gas composition inside and above the melt with respect to the amount of air entering the cell.

The improvements in this setup together with lower liquidus point of the melt brought several advantages. It led to a decrease in the heat loss from the oven, the possibility to work at lower temperatures resulting in longer service time of the materials inside the oven, and the ability to work with constant melt temperatures during the whole experiment. These advantages allowed the performance of emf measurements, video recordings, and temperature measurements simultaneously during addition and dissolution of alumina. Additionally, the setup was improved by the addition of a second camera, a digital single-lens reflex camera (Sony) on the other side of the oven to measure the dissolution time. Due to better insulation from the new windows, the cameras could be brought even closer to the crucible than in the previous experiments resulting in better resolution in the recorded videos.

The melt temperature was measured with a thermocouple type S and was kept around 950 °C prior to additions. The theoretical liquidus temperature was around 922 °C given a superheat of approximately 28 °C. Even though the setup was improved with respect to previous experiments, this relatively high superheat was necessary to avoid freezing of the bath due to the absence of insulation material and heating elements in the see-through zone.

Four subsequent additions of 1 wt% of Alumina A, B and C were performed for all the experiments. A stainless-steel feeding tube (Ø 15 mm, h=300 mm) together with a funnel was used for the additions of alumina. The feeding tube was placed approximately 1 cm above the melt. The addition time defined as the time between the first and last particle to hit the surface, ranged between 0.5 to 1.5 seconds

The emf measurements were carried out with the alumina probe shown in Figure 3.6 and the new graphite quasi-reference showed in Figure 3.12. A sketch of the quartz crucible is shown in Figure 3.14. A Data Acquisition System (DAQ)

measurement hardware (NI 9205) was used to obtain the emf data. Simultaneous video recording during the additions and dissolution process of the alumina was performed using the high-speed camera and the digital single-lens reflex camera located in front of the windows of the oven. The images shown were all taken from the high-speed camera due to its high-quality images suitable for extracting the dissolution characteristics. The high-speed camera could only serve for the first five minutes of the dissolution process due to limitations in memory capacity. The digital single-lens reflex camera was used to record the whole dissolution process for each alumina addition and to estimate the dissolution time.

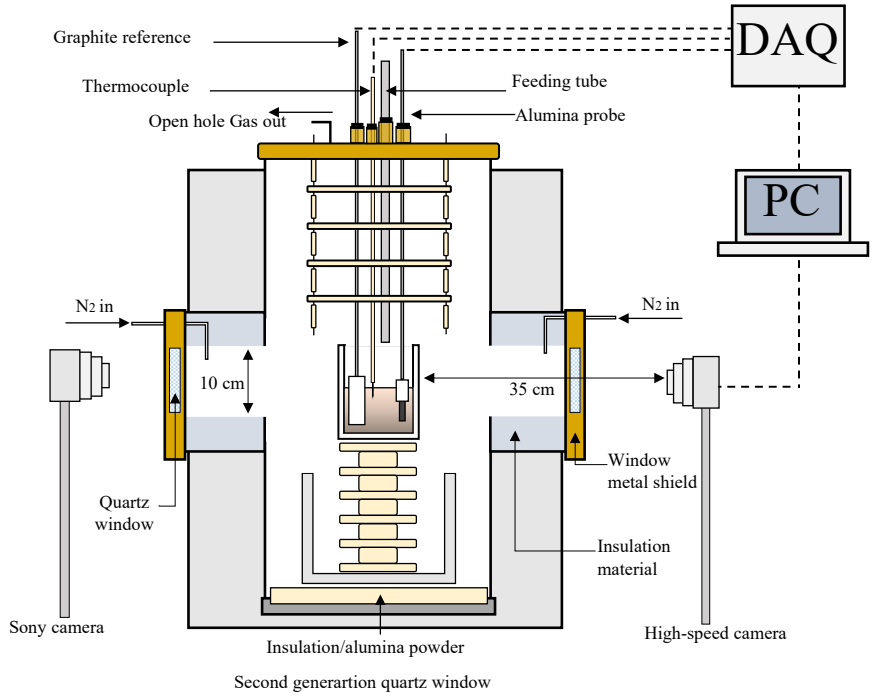

Figure 3.13 Sketch of the experimental setup for the simultaneous emf and optical measurements performed in a transparent quartz crucible.

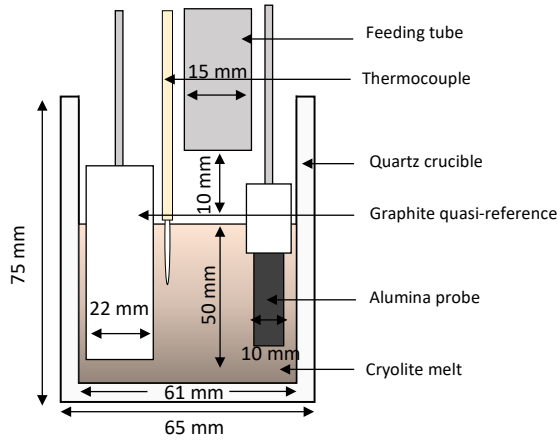

Figure 3.14 Sketch of the quartz crucible.

In addition, the effect of convection in the electrolyte was also studied applying a stainless-steel rod stirrer at a constant rotation speed of 200 rpm, Figure 3.15. The emf between the alumina probe and the graphite quasi-reference electrode was measured before and during the addition of alumina and throughout the entire dissolution process for all the experiments.

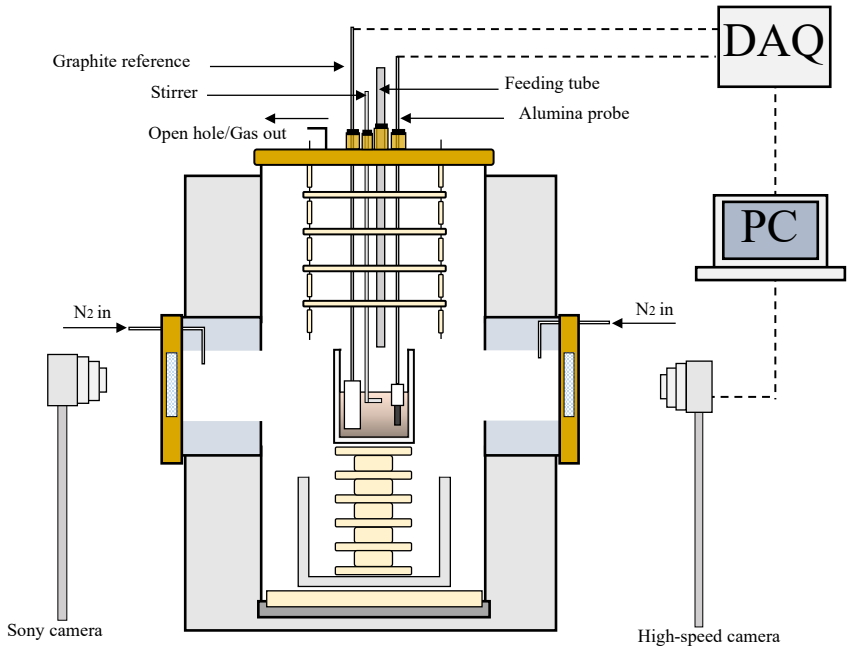

Figure 3.15 Set up for the emf measurements and visual recordings of the dissolution of alumina when stirring was applied. The thermocouple was removed due to space limitations.

Electrolyte and alumina

The experiments were performed using 250 g of bath. The initial composition was synthetic cryolite (74 wt%), aluminium fluoride (15 wt%), calcium fluoride (6.5 wt%)and lithium fluoride (3.5 wt%). The synthetic cryolite contained approximately 1 wt% of alumina. The use of LiF lowered the liquidus temperature of the bath allowing to operate the furnace at lower temperatures, resulting in longer lifetime of the crucible and materials inside the furnace. For the additions, three different industrial grade aluminas were used. Some of the most important physicochemical properties are shown in Table 3.1.

Table 3.1 Physicochemical properties of the different aluminas.

Alumina	MOI (300 °C) (%)	LOI (1000 °C) (%)	BET Surface (m^2/g)	ɣ-content alumina (%)	Particles ≤ 45 µm (%)
A	1.70	2.33	69.8	38.1	15
B	2.65	2.11	65	37.2	10
C	1.50	1.86	73.9	39.7	10

3.2.3 Chapter 7: Influence of secondary alumina properties on alumina dissolution in cryolite melt

See-through experiments

The setup showed in Figure 3.16 permitted the observation of dissolution of different aluminas from the addition and throughout the entire dissolution process. The characteristics of the dissolution mechanism and dissolution time were obtained. Possible correlation of the dissolution time with the physicochemical properties of the aluminas were evaluated.

The melt temperature was measured with a thermocouple type S and was kept around 960 °C prior to additions. The theoretical liquidus temperature was 931 °C given a superheat of approximately 29 °C. The relatively high superheat was necessary to avoid freezing of the bath due to the absence of insulation material and heating elements in the see-through zone of the furnace.

Video recording during the additions and dissolution process of alumina was performed using a high-speed camera (Photron Fastcam Mini AX) and a digital single-lens reflex camera (Sony) located in front of the windows of the oven. The images were all taken with the high-speed camera due to its high-quality images suitable for extracting the dissolution characteristics. The high-speed camera could only record for the first and last minutes of the dissolution process due to limitations in memory capacity. The digital single-lens reflex camera was used to record the whole dissolution process for each alumina addition and to estimate the dissolution time.

Based on the video recordings, the dissolution process was considered finished when no trace of crust or rafts was observed in the bath. This time could be decided with an estimated accuracy of approximately ± 0.2 minutes. The inaccuracy arises from transparency limitations of the crucible in addition to difficulties observing

small rafts through the meniscus that the melt made on the surface of the quartz crucible walls.

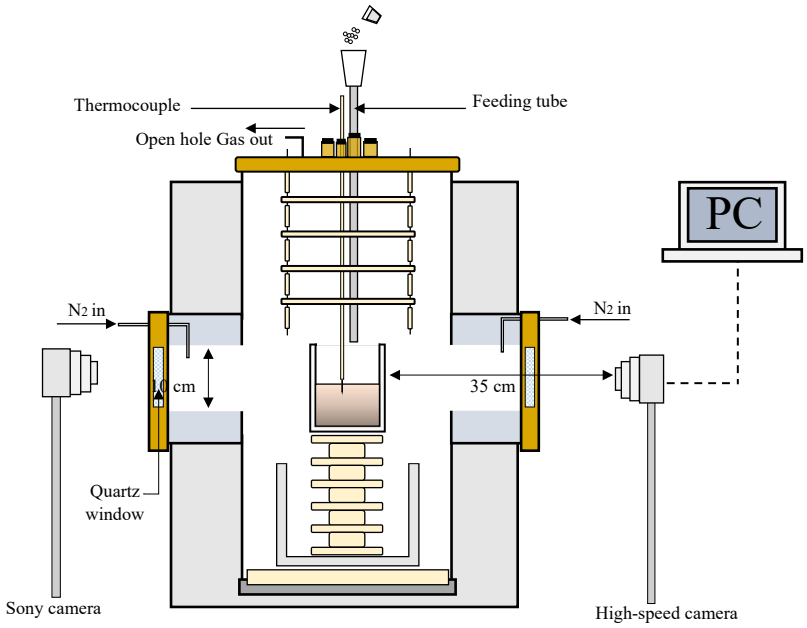

Figure 3.16 Principal sketch of the experimental set up for video recordings performed in a transparent quartz crucible.

The experiments were performed using 250 g of industrial bath. The initial composition was: cryolite 78 wt%, aluminium fluoride 9 wt%, calcium fluoride 6 wt%, lithium fluoride 5 wt%, and alumina 2 wt%. The use of LiF lowered the liquidus point of the bath allowing the operation of the furnace at lower temperatures resulting in longer lifetime of the crucible and materials inside the furnace.

Three different industrial grade aluminas were used. The aluminas have different particle size distribution, bulk alumina and alumina fines. Bulk alumina, was the term to define the aluminas as received from the industry, with particle sizes typically ranging between 0-250 μm. Alumina fines, were obtained by sieving the received aluminas to particles sizes ≤ 45 μm. After sieving, the particle size

distribution of bulk alumina and alumina fines were determined by laser diffraction using Miemodel of light scattering by particles. Measurements have been performed with a Coulter LS200 instrument. The physicochemical properties of the aluminas can be seen in chapter 7.

Four subsequent additions of 1 wt% of alumina bulk and alumina fines were performed using a stainless-steel feeding tube (Ø inner 1.5 cm, h 30 cm). The feeding tube was placed approximately 1 cm above the melt. The time between the first and last particle to hit the surface, ranged between 0.5 to 1.5 seconds. The addition was considered completed when the last particle hit the melt.

Chapter 4 Alumina Concentration Measurements in Cryolite Melt

Luis BRACAMONTE[1], Karoline NILSEN[1], Christian ROSENKILDE[2], Espen SANDNES[1]

[1]Department of Materials Science and Engineering, Norwegian University of Science and Technology NTNU, Trondheim, Norway
[2]Nork Hydro ASA, Hydro's Corporate Technology Office, Norway

Published in Light Metals 2020. Pp 600-607
https://doi.org/10.1007/978-3-030-36408-3_82

Abstract

The alumina dissolution is one of the most important processes for advanced aluminium electrolysis. For a better understanding and improvements on the dissolution process, it is important to find an effective and reliable method to perform in situ measurements in the cryolite melt, obtaining in this way the variation in alumina concentration during the entire electrolysis process. Electromotive force (emf) measurements between an electrochemical alumina sensor made of graphite and two reference electrodes (a graphite quasi-reference electrode and an aluminium reference electrode), were performed during the addition of alumina and throughout the entire process of dissolution. Cell reactions between the alumina sensor and the two reference electrodes were derived, and the theoretical cell voltages were calculated. The cell voltage measurements were analyzed and compared with the theoretical calculations to determine the reliability of the electrochemical sensor and verify the validity of the basis and assumptions used in this work for the determination of alumina concentration.

4.1 Introduction

The Hall–Héroult process involves electrolytic reduction of aluminium oxide (Al_2O_3) dissolved in molten cryolite ($3NaF\text{-}AlF_3$) at temperatures in the range of 970 °C [1]. The primary electrochemical reaction can be one of the following, Equations 4.1 and 4.2.

$$Al_2O_3(l) + 3C \rightarrow 2Al\ (l) + 3CO\ (g) \quad (4.1)$$

$$2Al_2O_3(l) + 3C\ (s) \rightarrow 4Al\ (l) + 3CO_2(g) \quad (4.2)$$

The cathode product is liquid aluminium, and the gaseous anode product is a CO_2-CO mixture. As a result, carbon anodes are consumed. The primary anode product is CO_2 (g), but some CO can be formed at low current densities 0.05 - 0.1 A cm^{-2} [2].

One of the most crucial mechanisms during the electrolysis process is the dissolution of alumina in cryolite melts. This dissolution can be described by different steps, from the release of alumina powder during the addition until the formation of a homogeneous solution in the electrolyte. These steps include: the crust formation when the bath freeze around the alumina particles, heating and remelting of the bath, the conversion of gamma-alumina to alpha-alumina and the dissolution of alpha-alumina to lastly have the completely dissolved alumina and uniform electrolyte composition. Chemical reactions and physical processes strongly influence the dissolution process and both heat and mass transfer can be rate determining [3,4]. Due to the complexity of all the steps of the dissolution process mentioned above, a continuous, reliable and simple measurement of the alumina concentration could be beneficial in extracting information on the dissolution process. Also, continuous alumina concentration measurements could be beneficial during operation of industrial cells in order to avoid formation of muck, bottom sludge or crust which give an increase in resistance and temperature and decrease in current efficiency [5]. Technology for continuous measurements has not yet been implemented in industry.

Several attempts have been made to achieve reliable and continuous alumina concentration measurements in lab scale. Some studies are based on the correlation between the alumina concentration profiles and the current distribution in the electrolysis cell [6] and some based on electrochemical methods such as

chronopotentiometry or fast linear sweep voltammetry, often termed critical current density [7,8]. Electromotive force measurements (emf) based on an electrical voltage difference, is one of the electrochemical methods that can also be used to study the dissolution process. Vasyunina et al. studied the solubility and the dissolution rate of alumina in acidic cryolite aluminous melts using an electrochemical method based on a measurement of the equilibrium electromotive force of a concentration galvanic cell.

The objective of the present work is to study the performance of an electrochemical alumina sensor made of carbon. emf measurements between the alumina sensor and two different reference electrodes is to be explored. The alumina sensor is based on the reaction between oxide species in the bath and carbon. Thus, the measured emf is a result of the activity of oxide in the bath. This type of sensor has previously not been reported. A new quasi-reference carbon electrode has also been made and tested. Since the sensor and reference electrode are based on carbon, the principle is expected to function for long periods in the corrosive cryolite bath. This can potentially make the principle applicable in an industrial setting.

4.2 Method

The cell reactions between the alumina sensor and a reference electrode are derived together with the corresponding Nernst equations and theoretical emf values. As the alumina sensor is based on a graphite material it is also referred to as a graphite probe. Two different reference electrodes are used. One of the reference electrodes is the well-known aluminium reference electrode, and the other reference electrode is a quasi-reference electrode which applies the same principle as the alumina sensor but with an internal chamber with a bath saturated with alumina. Calculated emf values were compared to experimental measurements to explore the reliability of the electrochemical alumina sensor

4.2.1 Graphite probe versus graphite quasi-reference electrode

A carbon crucible containing cryolite melt, a graphite probe and a graphite quasi-reference electrode are shown in Figure 4.1. The graphite quasi-reference is a graphite electrode placed inside a boron nitride tube. A small hole in the boron nitride tube ensures electrical contact between the alumina saturated bath inside the tube (chamber I) and the bath in the crucible (chamber II).

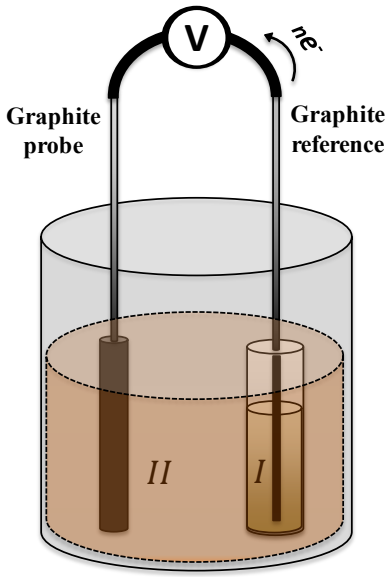

Figure 4.1: Illustration of the electrochemical cell with the graphite probe and the graphite quasi-reference electrode.

The half-cell reactions between the graphite probe and the graphite quasi-reference electrode taking place in the chambers are shown in Equations 4.3 and 4.4. Equation 4.5 represents the migration of sodium ions from chamber I to chamber II in order to maintain charge neutrality. The addition of the half-cell reactions is shown in Equation 4.6.

Chamber I $$O^{2-}_{(I)} + C_{(I)} = 2e^- + CO_{(I)} \quad (4.3)$$

Chamber II $$CO_{(II)} + 2e^- = C_{(II)} + O^{2-}_{(II)} \quad (4.4)$$

$$Na^+_{(I)} = Na^+_{(II)} \quad (4.5)$$

$$C_{(I)} + CO_{(II)} + Na_2O_{(I)} = CO_{(I)} + C_{(II)} + Na_2O_{(II)} \quad (4.6)$$

As E^0 is equal to 0, the Nernst equation for the cell reaction becomes as written in Equation 4.7, where n is equal to 2. In Equation 4.5, it is implicitly assumed that $t_{Na^+} = 1$, which is not far from reality [9].

$$E = -\frac{RT}{nF} \ln \frac{P_{CO_{(I)}} \cdot a_{Na_2O_{(II)}} \cdot a_{C_{(II)}}}{P_{CO_{(II)}} \cdot a_{Na_2O_{(I)}} \cdot a_{C_{(I)}}} \quad (4.7)$$

The activity of CO is expressed as the partial pressure of CO above the melt since the adsorbed CO is believed to be in equilibrium with partial pressure of CO in the melt which is also in equilibrium with the pressure of CO above the melt. The expression in Equation 4.7 can be simplified to Equation 4.8 as $a_{C_{(I)}}$ is equal to $a_{C_{(II)}}$ because the same graphite material is used in both electrodes, and with the assumption that the CO pressure is constant and equal in chamber I and II.

$$E = -\frac{RT}{2F} \ln \frac{a_{Na_2O_{(II)}}}{a_{Na_2O_{(I)}}} \quad (4.8)$$

By using data from FactSage (ThermFact Inc., Montreal, Canada) it can be found that the a_{Na_2O} versus the alumina concentration is roughly linearly related. This implies that the activity coefficient of Na_2O is approximately constant if the bath composition (exclusive of alumina) is the same in chambers I and II. This gives another simplification of the Nernst equation, Equation 4.9.

$$E = -\frac{RT}{2F} \ln \frac{wt\%\ Al_2O_{3\ (II)}}{wt\%\ Al_2O_{3(I)}} \quad (4.9)$$

Finally, the potential of the graphite probe can be expressed as a function of the alumina concentration. The calculated values are given in Figure 4.2.

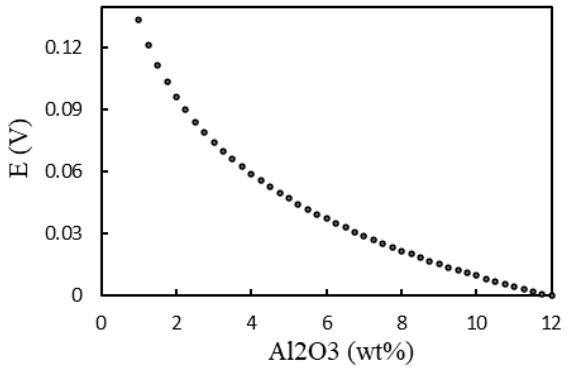

Figure 4.2: Calculated values of the potential of a graphite electrode vs. a graphite quasi-reference electrode as a function of alumina concentration (T= 975 ˚C, 11 wt% $Al_2O_{3(l)}$).

Moreover, Equation 4.9 shows that the relation between the cell potential and the temperature is linear at constant alumina content. In Figure 4.3 this relation is plotted for different alumina concentrations. There is a minor effect on the potential at low alumina content, while it is almost negligible at concentrations close to saturation.

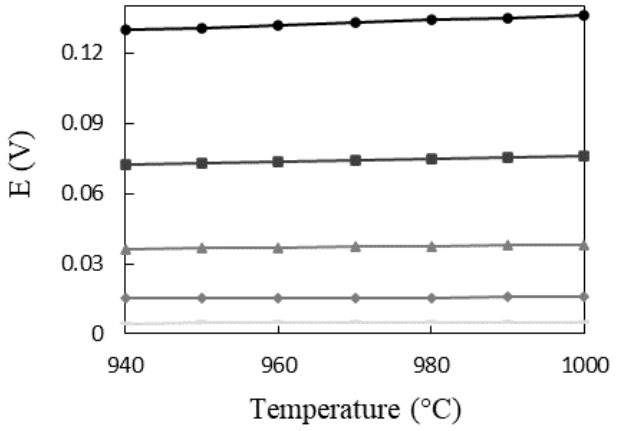

Figure 4.3: Calculated values of the potential of a graphite electrode vs. the graphite quasi-reference electrode as a function of the temperature at different

alumina concentrations. Concentration of alumina: 1 wt% (circular dots), 3 wt% (square dots), 6 wt% (triangles), 9 wt% (rhombus), and 11 wt% (small dashes).

4.2.2 Graphite probe versus aluminium reference electrode

Applying the same reasoning as for the case with the graphite reference showed in Figure 4.1, the half-cell reactions between the graphite probe and the aluminium reference electrode are shown in the Equations 4.10 and 4.11. Equation 4.12 represents the migration of sodium ions between chamber I and chamber II in order to maintain charge neutrality.

Chamber I $$2Al_{(I)} = 6e^- + 2Al^{3+}_{(I)} \quad (4.10)$$

Chamber II $$3CO_{(II)} + 6e^- = 3C_{(II)} + 3O^{2-}_{(II)} \quad (4.11)$$

$$6Na^+_{(I)} = 6Na^+_{(II)} \quad (4.12)$$

$$3O^{2-}_{(I)} = 3O^{2-}_{(I)} \quad (4.13)$$

$$2Al_{(I)} + 3CO_{(II)} + 3Na_2O_{(I)} = Al_2O_{3(I)} + 3C_{(II)} + 3Na_2O_{(II)} \quad (4.14)$$

$$E^0_{(T)} \neq 0 \quad (4.15)$$

Equation 4.13, i.e the addition of 3 oxide ions to chamber I at each side of the reaction, is introduced to avoid complications to determine the reference state of ionic species in the Nernst equation. The total cell reaction is shown in Equation 4.14. As $E^0_{(T)}$ is different to zero as it is shown in Equation 4.15, the Nernst equation for the cell can be written as in Equation 4.16.

$$E = E^0_{(T)} - \frac{RT}{6F} \ln \frac{a_{Al_2O_{3(I)}} \cdot a^3_{C_{(II)}} \cdot a^3_{Na_2O_{(II)}}}{a^2_{Al} \cdot P^3_{CO_{(II)}} \cdot a^3_{Na_2O_{(I)}}} \quad (4.16)$$

It can be simplified to Equation 4.17 by assuming the activity of the liquid aluminium equal to 1.

$$E = E^{0}_{(T)} - \frac{RT}{6F} \ln \frac{a_{Al_2O_{3(I)}}}{P^{3}_{CO_{(II)}}} - \frac{RT}{2F} \ln \frac{a_{Na_2O_{(II)}}}{a_{Na_2O_{(I)}}} \quad (4.17)$$

At saturation, the activity of alumina is 1, so $a_{Al_2O_{3(I)}}$ is assumed to be 1 in Equation 4.17. The a_{Na_2O} versus the alumina concentration is roughly linearly related, so the a_{Na_2O} can be replaced with the alumina concentration. Equation 4.17 therefore simplifies to Equation 4.18. Given an empiric cell potential of ~1 V at 1 wt% Al_2O_3, the partial pressure of CO was estimated to 0.022 atm.. $E^{0}_{(T)}$ was found from FactSage at T = 975 °C.

$$E = E^{0}_{(T)} - \frac{RT}{6F} \ln \frac{1}{P^{3}_{CO_{(II)}}} - \frac{RT}{2F} \ln \frac{wt\%\ Al_2O_{3\ (II)}}{wt\%\ Al_2O_{3\ (I)}} \quad (4.18)$$

Then, the potential of the graphite probe can be expressed as a function of the alumina concentration. The calculated values are given in Figure 4.4.

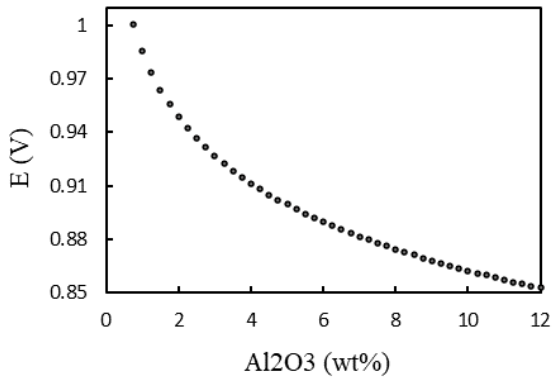

Figure 4.4: Calculated values of the potential of a graphite electrode vs. an aluminium reference electrode as a function of alumina concentration (T= 975 ˚C).

4.3 Experimental work

4.3.1 Design of the graphite probe

The graphite probe is shown in Figure 4.5a. The electrode is a graphite rod. The graphite electrode was made of the same carbon material as the graphite rod used in the graphite quasi-reference electrode.

4.3.2 Design of the graphite quasi-reference electrode

The graphite quasi-reference electrode is shown in Figure 4.5b. A carbon rod (Ø 5 mm, height 50 mm) was screwed to a graphite connector and put inside a boron nitride tube (Ø 10/22 mm). A hole (1.5 mm) was drilled above the bottom of the tube. A steel rod connector bar (height 50 cm) was screwed to the graphite connector. Alumina (3 g) was added inside the boron nitride tube in order to make an alumina saturated bath (10-12 wt%).

4.3.3 Design of the aluminium reference electrode

An illustration of the aluminium reference electrode is shown in Figure 4.5c and is mainly based on the reference electrode described by Sommerseth et al. [10]. A boron nitride tube (Ø 5/10 mm) was screwed to a steel tube. Pure aluminium metal (0.65 g) was added inside the boron nitride tube. A hole was drilled above the metal surface to allow bath to enter the tube. A tungsten wire in contact with the molten aluminium was used for electrical contact.

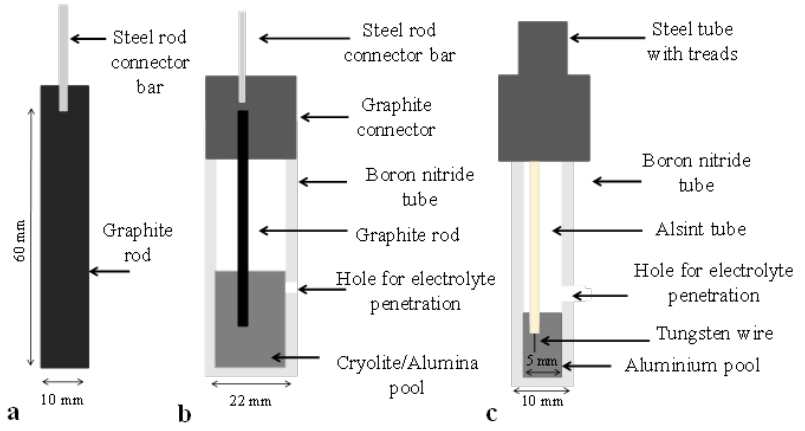

Figure 4.5: Sketch of: **a** Graphite probe **b** Graphite quasi-reference electrode **c** Aluminium reference electrode.

4.3.4 Apparatus setup

A carbon crucible (Ø 85 mm, height 130 mm) with cryolite (500 g) was place inside a closed furnace as it is showed in Figure 4.6. The furnace was heated until the temperature inside the melt reached 975 °C. Experiments were done under N_2 or CO_2 atmosphere. All electrodes and a thermocouple type S were put inside the melt and were fixed by plugs to the top lid of the furnace. Additions of 3 wt% of primary alumina were performed using a feeding tube. emf measurements between the graphite probe and the two references electrodes were performed during the addition of alumina and throughout the entire dissolution process. A logger (Keithley 2000 multimeter) was used to acquire the emf data and temperature.

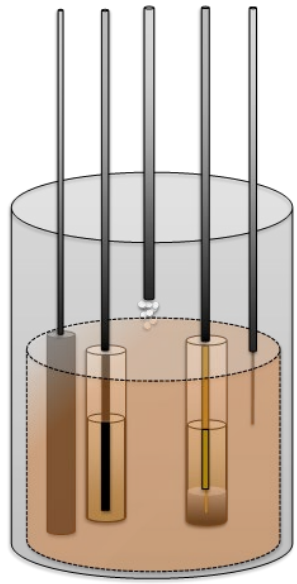

Figure 4.6: Principal sketch of the cell setup. From left to right: graphite probe, graphite quasi-reference electrode, alumina feeding tube, aluminium reference electrode and thermocouple.

4.4 Results and Discussion

The variation in potential between the graphite probe and the graphite quasi-reference electrode vs. time during 5 additions of alumina is shown in Figure 4.7. The temperature variation is also shown. The variation in potential can be divided

into two characteristic stages for each addition of alumina. The first stage is a very sharp drop followed by a second stage characterized by a slow increase until stabilization at a constant potential. Immediately after the first addition of 3 wt% of alumina at 5742 s the potential dropped quickly, followed by a slow increase and stabilization around -0.033 V. The 0.059 V difference in potential from the starting value at 0.026 V to the final value at -0.033 V is similar to the 0.068 V difference in potential expected from theoretical values shown in Figure 4.2. The temperature dropped about 20 °C immediately after the addition of alumina followed by a continuos increase and stabilization back to the starting temperature around 975°C. This drop of approximately 20 °C in temperature corresponds to a 2 mV theoretical decrease in the potential. This decrease is small compared to the 0.059 V decrease observed. The temperature decrease associated with alumina addition is therefore considered to have only a small effect on the measured potential value. This effect gets smaller when approaching alumina saturation as shown in Figure 4.3.

The drop in the potential after the second addition of 3 wt% of alumina was about 0.046 V which is also relatively consistent with the 0.037 V decrease in potential expected from the calculations. After the fourth additions the bath became saturated and the potential stabilized around -0.102 V.
The potential before the first addition (0.026 V) was not the same as the calculated (0.14 V). However, the total decrease in the potential was around 0.13 V at saturation which is comparable to the 0.14 V decrease in potential expected from the calculations.

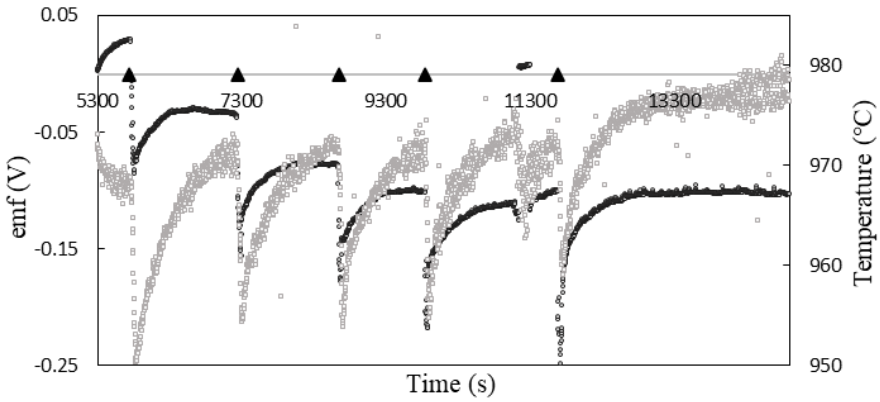

Figure 4.7: emf between the graphite probe and the graphite quasi-reference electrode vs. time (circular dark dots). Temperature vs. time (square light dots). Addition of 3 wt% alumina (triangles).

The variation in potential between the graphite probe and the aluminium reference electrode vs. time during 5 additions of alumina is presented in Figure 4.8. These variations in the potential can also be divided into two characteristic stages for every addition of alumina. Contrary to the initial potential drop observed using the graphite reference electrode, the first stage is characterized by a rapid increase in the potential followed by a second stage characterized by a slow and continuos decrease. Furthermore, no plateaus or constant values are reached in the potential after any addition of alumina.

After the first addition of 3 wt% alumina was done, a rapid increase in the potential was observed followed by a continuos decrease until the potential reached 0.84 V. This change of approximately 0.11 V in the potential from 0.95 V to 0.84 V is comparable to the 0.13 V difference in potential expected from calculations and shown in Figure 4.4. The behaviour of the temperature was the same as previously observed, i.e. a rapid decrease immediately after the alumina was added followed by an increase and stabilization back to the initial temperature. After the second addition of 3 wt% of alumina the potential reached a value of 0.82 V. This decrease of 0.02 V is somewhat lower than the 0.03 V difference in potential expected from calculations. The total change in the potential was around 0.14 V at saturation which is consistent with the calculated 0.14 V change in potential shown in Figure 4.4 The expected plateaus of the potential were not observed after additions of alumina.

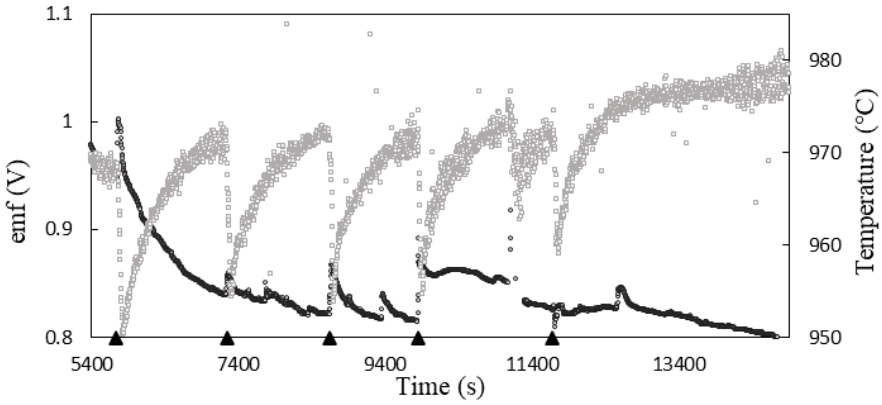

Figure 4.8: emf between the graphite probe and the aluminium reference electrode vs. time (circular dark dots). Temperature vs. time (square light dots). Addition of 3 wt% alumina (triangles).

Important challenges were faced during the experiments such as non-stabilized potential in experiments where the aluminium reference electrode was applied, potential noise, and sudden drops and jumps in potential just after alumina addition. In order to understand these events, some experiments were performed. Nitrogen was normally the gas flowing through the furnace during experiments. When a plug in the lid was opened air could enter the furnace. The emf measurements were strongly affected during such an operation. An example is shown in Figure 4.9. The potential increased from 0.907 V when the plug of the lid was closed to 0.917 V when the plug was opened.

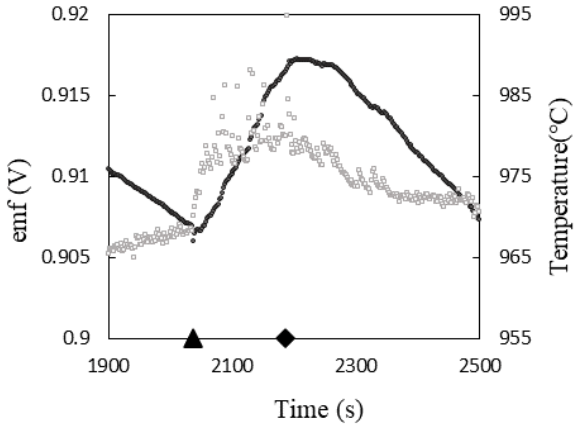

Figure 4.9: Influence of exposure of the cell to atmosphere on the potential (circular dark dots) when the gas composition above the melt was N_2. Temperature vs. time (square light dots). Lid opening (triangle). Lid closing (rhombus).

Substitution of N_2 by CO_2 was done in order to study the influence of having a gas composition rich in CO_2 above the melt. The result is presented in the Figure 4.10. It seems that when using CO_2 air entering the furnace does not affect the measurement. The potential value was around 0.856 V when the lid of the oven was closed and remained constant when it was opened.

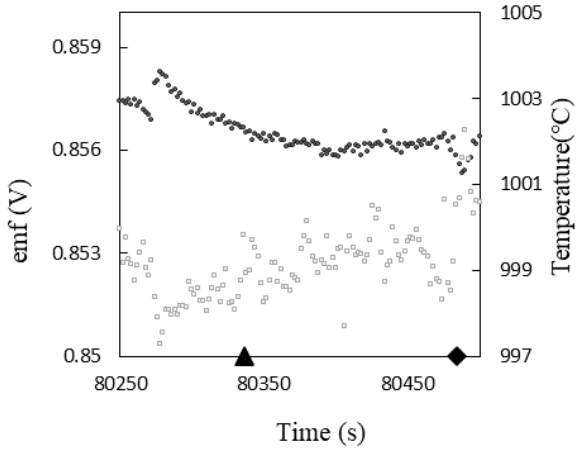

Figure 4.10: Influence of exposure of the cell to atmosphere on the potential (circular dark dots) when the gas composition above the melt was CO_2. Temperature vs. time (square light dots). Lid opening (triangle). Lid closing (rhombus).

The reactions shown in Equations 4.19, 4.20 and 4.21 may alter the partial pressures of CO and CO_2 in the cell and cause an increase in the potential.

$$C_{(S,anode)} + O_{2(gas)} = CO_{2(gas)} \quad (4.19)$$

$$C_{(S,anode)} + O_{2(gas)} = 2CO_{(gas)} \quad (4.20)$$

$$2CO_{(gas)} + O_{2(gas)} = 2CO_{2(gas)} \quad (4.21)$$

A constant flow of CO_2 into the cell is believed to prevent large variations in the partial pressures of CO and CO_2. The added CO_2 will establish a buffer system with respect to small amounts of air entering the cell.

Another important factor that is believed to affect the potential and which may be responsible for the continuous drifting in the potential as seen in Figure 4.7, was the dissolution of aluminium from the reference electrode into the melt. Dissolved aluminium is a strong reducing agent. To confirm this assumption, a few grams

of aluminium was added to the bath. The effect of the addition was a drop in the potential of more than 0.3 V as Figure 4.11 shows. This drop can be due to the reaction between aluminium and CO_2 or CO as shown in Equation 4.22.

$$4Al_{(diss)} + 6CO_{(gas)} = 2Al_2O_{3(diss)} + 6C_{(s)} \quad (4.22)$$

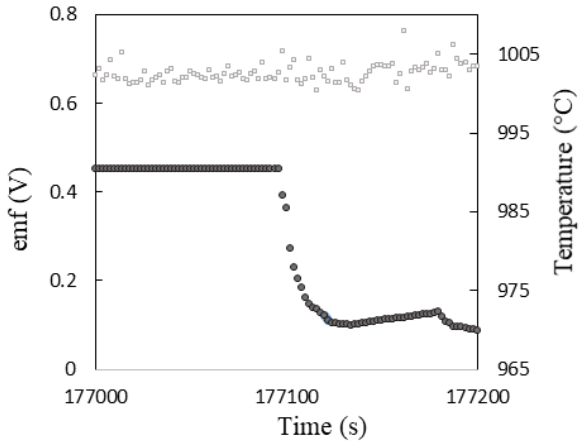

Figure 4.11: Influence of the addition of pure aluminium on the potential (circular dark dots). Temperature (square ligth dots).

4.5 Conclusions

The electrochemical alumina sensor has been tested. The decrease in potential associated with alumina additions is comparable to the calculated values. The total decrease in potential at saturation is also corresponding with calculated values. However, some potential measurements are sometimes not in agreement with the calculated values. There are some factors that causes sudden variations and drifting in the potential. The reactions between dissolved aluminium and CO and CO_2 are believed to be one of the main reasons for the drifting in potential when using the aluminium reference electrode. The entering of oxygen from the air into the furnace can cause changes in the partial pressures of CO and CO_2 which might affect the potential values of the electrodes.

References

1. Thonstad J, Fellner P, Haarberg GM (2001) Aluminium Electrolysis: Fundamentals of the Hall-Herault Process. Aluminium-Verlag.
2. Thonstad, J (1964) On the anode gas reactions in aluminium electrolysis, II. J. Electrochem. Soc. Vol. 111, No. 8, 959-965.
3. Grjotheim K, Kvande H (1993) Introduction to aluminium electrolysis: understanding the hall-heroult process. Aluminium-Verlag, Dusseldorf.
4. Thonstad J, Solheim A, Rolseth S, Skar O (1988) The dissolution of alumina in cryolite melts. Essential Readings in Light Metals, 105–111.
5. Zhan SQ, Mao LI, Zhou JM, Yang JH, Zhou YW (2015) Analysis and modeling of alumina dissolution based on heat and mass transfer. Transactions of Nonferrous Metals Society of China, 25(5):1648–1656.
6. Jakobsen S (2001) Estimating alumina concentration distribution in aluminium electrolysis cells. IFAC Automation in Mining, Mineral and Metal Processing. Tokyo.
7. Richards NE, Rolseth S, Thonstad J, Haverkamp RG (1995) Electrochemical analysis of alumina dissolved in cryolite melts. Light Metals 1995, 391–404.
8. Vasyunina NV, Vasyunina IP, Mikhalev YG, Vinogradov AM (2009) The solubility and dissolution rate of alumina in acidic cryolite aluminous melts. Russian Journal of Non-Ferrous Metals, 50(4):338–342.
9. Frank WB, Foster LM (1957) Investigation of transport phenomena in the cryolite-alumina system by mean of radioactive tracers. J.Phys. Chem. 61, 1531-1536.
10. Sommerseth C (2016) The effect of production parameters on the performance of carbon anodes for aluminium production. Ph.D. thesis, Norwegian University of Science and Technology, NTNU.

Chapter 5 Dissolution Characteristics and Concentration Measurements of Alumina in Cryolite Melts

Luis BRACAMONTE[1], Vegard AULIE[1], Christian ROSENKILDE[2], Kristian Etienne EINARSRUD[1], Espen SANDNES[1]

[1]Department of Materials Science and Engineering, NTNU Norwegian University of Science and Technology, Trondheim, Norway
[2]Nork Hydro ASA, Hydro's Corporate Technology Office, Norway

Published in Light Metals 2021: pp. 495-503
https://doi.org/10.1007/978-3-030-65396-5_70

Abstract

Alumina dissolution is one of the most important processes in the Hall-Héroult process. In this work, video recording using a high-speed camera and a see-through cell and electromotive force (emf) based alumina sensor measurements were performed during the addition of alumina and throughout the entire dissolution process. These methods can reveal crucial information about the alumina-bath interaction and the variation of the alumina concentration during the dissolution process. The sensor data reflecting the actual dissolved alumina in the melt is interesting itself, but especially so when analyzed together with the alumina-bath interaction obtained from the see-through cell.

5.1 Introduction

The alumina dissolution process in aluminium reduction cells is a complex process which can be described starting from the formation of a crust when the bath freezes around the alumina particles at the moment of the feeding, followed by the heating and re-melting of the bath, and then ending with the conversion of gamma-alumina to alpha-alumina. For this reason, the dissolution of alumina has always been a challenge and subject of study over the years [1,2]. The acquisition of reliable data to describe the dissolution of alumina and to better understand its behaviour, is undoubtedly a key factor to achieve important improvements in the Hall-Héroult process. The development of a method to perform in-situ alumina concentration measurements during the dissolution could lead to acquisition of important data to later being able to enhance the alumina dissolution process. Some of the investigations that have tried to develop a method to measure the concentration of alumina have been based on electrochemical techniques such as linear sweep voltammetry (LSV), critical current density (CCD) and chronopotentiometry [3,4,5]. Electromotive force (emf) is another electrochemical technique that has been very important during the years due to the usability and reliability of emf based sensors in different molten salt systems [6,7,8]. Another important type of measurement is based on physical observations. Haupin et al. were one of the first to use a see-through quartz cell for the observation of electrolyte circulation, alumina dissolution and gas bubble formation during electrolysis [9]. More recently, Yang et al. have carried out various studies in high temperature transparent cells to observe the behaviour and nature of some important phenomena during the dissolution of alumina in molten salts [10,11]. The present work shows emf-based alumina sensor measurements together with selected pictures from the addition and dissolution process of primary and secondary alumina using a transparent cell and a high-speed camera. In addition, the particle size distribution and the surface morphology of the primary and secondary alumina are presented.

5.2 Method

The cell reactions for the alumina sensor and an aluminium reference electrode are derived together with the corresponding Nernst equations and theoretical emf values. Calculated emf values were compared to experimental measurements to explore the reliability of the electrochemical alumina sensor

5.2.1 The alumina sensor principle

A quartz crucible containing cryolite melt, an alumina probe and an aluminium reference electrode are shown in Figure 5.1. The aluminium reference consists of a tungsten wire in contact with molten aluminium and placed inside a boron nitride tube. A small hole in the boron nitride tube ensures ionic contact between the bath inside the tube (chamber I) and the bath in the crucible (chamber II).

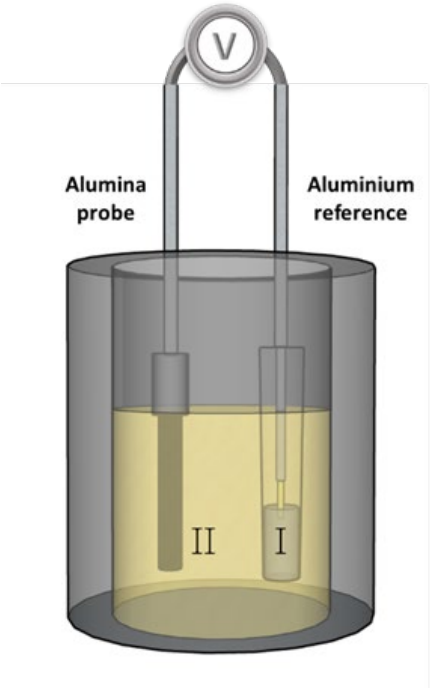

Figure 5.1: Illustration of the electrochemical cell with the alumina probe and the aluminium reference electrode.

The half-cell reactions between the alumina probe and the aluminium reference electrode taking place in the chambers are shown in Equations 5.1 and 5.2.

Equation 5.3 represents the migration of sodium ions between chamber I and chamber II in order to maintain charge neutrality, assuming the transference number of Na^+ to be 1 [12].

Chamber I $$2Al_{(I)} = 6e^- + 2Al^{3+}_{(I)} \quad (5.1)$$

Chamber II $$3CO_{(II)} + 6e^- = 3C_{(II)} + 3O^{2-}_{(II)} \quad (5.2)$$

$$6Na^+_{(I)} = 6Na^+_{(II)} \quad (5.3)$$

$$3O^{2-}_{(I)} = 3O^{2-}_{(I)} \quad (5.4)$$

$$2Al_{(I)} + 3CO_{(II)} + 3Na_2O_{(I)} = Al_2O_{3(I)} + 3C_{(II)} + 3Na_2O_{(II)} \quad (5.5)$$

Equation 5.4, i.e. the addition of 3 oxide ions to chamber I at each side of the reaction, is introduced to avoid complications to determine the reference state of ionic species in the Nernst equation. The total cell reaction is shown in Equation 5.5. As $E^0_{(T)}$ is different from zero as shown in Equation 5.6.

$$E^0_{(T)} \neq 0 \quad (5.6)$$

The Nernst equation for the cell can be written as in Equation 5.7.

$$E_{(T)} = E^0_{(T)} - \frac{RT}{6F} \ln \frac{a_{Al_2O_{3(I)}} \cdot a^3_{C_{(II)}} \cdot a^3_{Na_2O_{(II)}}}{a^2_{Al} \cdot P^3_{CO_{(II)}} \cdot a^3_{Na_2O_{(I)}}} \quad (5.7)$$

It can be simplified to Equation 5.8 by assuming the activity of the liquid aluminium equal to 1.

$$E_{(T)} = E^0_{(T)} - \frac{RT}{6F} \ln \frac{a_{Al_2O_{3(I)}}}{P^3_{CO_{(II)}}} - \frac{RT}{2F} \ln \frac{a_{Na_2O_{(II)}}}{a_{Na_2O_{(I)}}} \quad (5.8)$$

The bath in chamber I is saturated with alumina, thus $a_{Al_2O_{3(I)}}$ is equal to 1 in Equation 5.8. By using data from FactSage (ThermFact Inc., Montreal, Canada) it can be found that the a_{Na_2O} versus the alumina concentration is roughly linearly related, so a_{Na_2O} can be replaced with the alumina concentration. Equation 5.8 therefore simplifies to Equation 5.9.

$$E_{(T)} = E^0_{(T)} - \frac{RT}{6F} \ln \frac{1}{P^3_{CO_{(II)}}} - \frac{RT}{2F} \ln \frac{wt\%\ Al_2O_{3\ (II)}}{wt\%\ Al_2O_{3\ (I)}} \qquad (5.9)$$

Given an empirical cell potential of approx. 1.0 V at 1 wt% Al_2O_3, the partial pressure of CO in chamber II was calculated to 0.022 atm. From FactSage $E^0_{(T)}$ was found to be 1.057 V. The alumina concentration in chamber I has been calculated to 12 wt%.

The theoretical potential of the alumina probe as a function of the alumina concentration is shown in Figure 5.2.

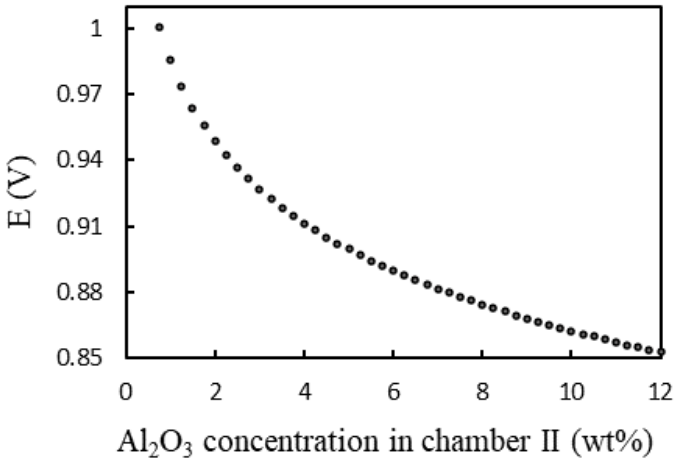

Figure 5.2: Calculated values of the potential of the alumina probe vs. the aluminium reference electrode as a function of alumina concentration (T= 975 ˚C).

5.3 Experimental work

5.3.1 Design of the alumina probe and the aluminium reference electrode

The alumina probe is shown in Figure 5.3a. The electrode is a graphite rod shielded with a boron nitride tube on the top. The purpose of the shielding is to hinder the reaction with air present above the melt.

An illustration of the aluminium reference electrode is shown in Figure 5.3b. The electrode is mainly based on the reference electrode described by Sommerseth et al. [13]. A boron nitride tube (Ø 5/10 mm) was threaded to a steel tube. Pure aluminium metal (0.45 g) was placed inside the boron nitride tube. A hole above the metal surface allowed the bath in chamber II to enter the boron nitride tube. A tungsten wire in contact with the molten aluminium was used for electrical contact. The wire was shielded with an alumina tube to hinder the wire to be in contact with the bath inside the boron nitride tube. The alumina tube ensured saturation of the bath inside the boron nitride tube.

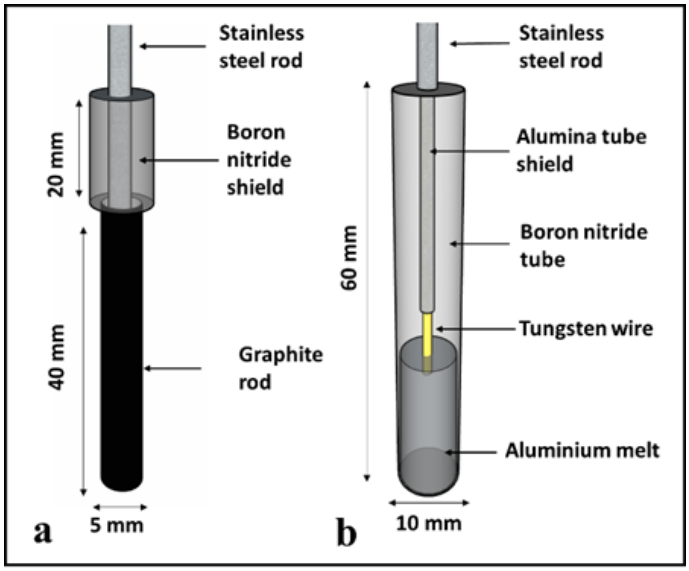

Figure 5.3: Sketch of **a** Alumina probe electrode **b** Aluminium reference electrode.

5.3.2 Apparatus and Measurements

A transparent quartz crucible (Ø 65 mm, height 75 mm) was used to contain the bath. The initial bath composition was synthetic cryolite (200 g) with approx. 1 wt% of alumina. The crucible was placed inside a see-through furnace (a custom-made furnace from Entech Energiteknik AB). The working temperature was 980 °C. The furnace was not completely sealed so the gas composition inside the furnace was close to the composition of the ambient air. Additions of 2 wt% of secondary alumina were performed using a feeding tube (stainless steel). The emf between the alumina probe and the aluminium reference electrode was measured during the addition of alumina and throughout the entire dissolution process. A Data Acquisition System (DAQ) measurement hardware (NI 9205) was used for obtaining the emf data. Visual observations were not done during emf experiments to avoid opening of the oven and freezing of the bath. The set-up is shown in Figure 5.4.

The video recording of the alumina dissolution process was performed using the following initial bath composition: synthetic cryolite (150 g, 75 wt%), aluminium fluoride (30 g, 15 wt%) and calcium fluoride (20 g, 10 wt%). The reason why the optical measurements were not performed with the same bath composition as the emf measurements is that a lower liquidus temperature was needed to avoid bath freeze on the walls of the quartz crucible. The working temperature was 980 °C. Subsequent additions of 1 wt% of primary and secondary alumina were performed separately to different baths using a feeding tube. The video recording was performed applying a high-speed camera (Photron Fastcam Mini AX)

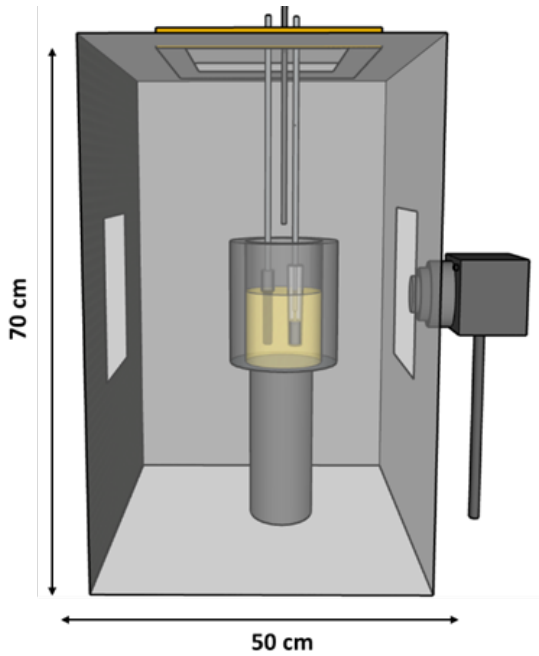

Figure 5.4: Principal sketch of the experimental set up for the emf and optical measurements performed in a transparent quartz crucible. The cell is placed in the middle of the furnace and contains the electrodes from figure 3. An alumina feeding tube is inserted from the top. The high-speed camera is shown on the right.

5.3.3 Particle size distribution and surface morphology

Scanning Electron Microscopy (SEM) was performed in a Zeiss Supra 55 VP for both primary and secondary alumina. The accelerating voltage (EHT) was 10 kV, and the working distance (WD) was 10 mm. Particle size distribution data was obtained by the average axes measured for two parallels of each type of alumina.

5.4 Results and Discussion

5.4.1 Emf measurements

The emf vs. time during five consecutive additions of secondary alumina is presented in Figure 5.5. The measured emf after each addition shows a sharp increase followed by a gradual decrease until the potential more or less stabilizes. The gradual decrease before the stabilization is interpreted as an increase in the alumina concentration. After stabilization there is a fairly good agreement

between the measured and calculated potential values for all additions. This indicates that the fundamental working principle stated for the sensor is correct.

A feature of the emf-curve which is unexpected is the abrupt increase in the potential after each addition. The fast response on the addition suggests that it is related to a surface phenomenon. The alumina fed to the bath is also introducing air and moisture into the bath. The air originates from the ambient air surrounding the alumina particles as they enter the bath. Some of the air inside pores in the alumina particles might also enter the bath. The oxygen may react with the carbon surface of the sensor increasing the CO activity around the sensor. This will quickly increase the potential according to equation 5.7. The potential is more sensitive to this phenomenon when the oxide activity is low as suggested from Figure 5.2 showing the fast exponential increase in potential when approaching zero alumina concentration. Figure 5.5 illustrates this as the initial potential increase is significant larger for the first addition than for the subsequent additions. An additional indication of the sensitivity of the sensor at very low oxide concentrations was the oscillations between 1 V and 1.1 V before the first addition.

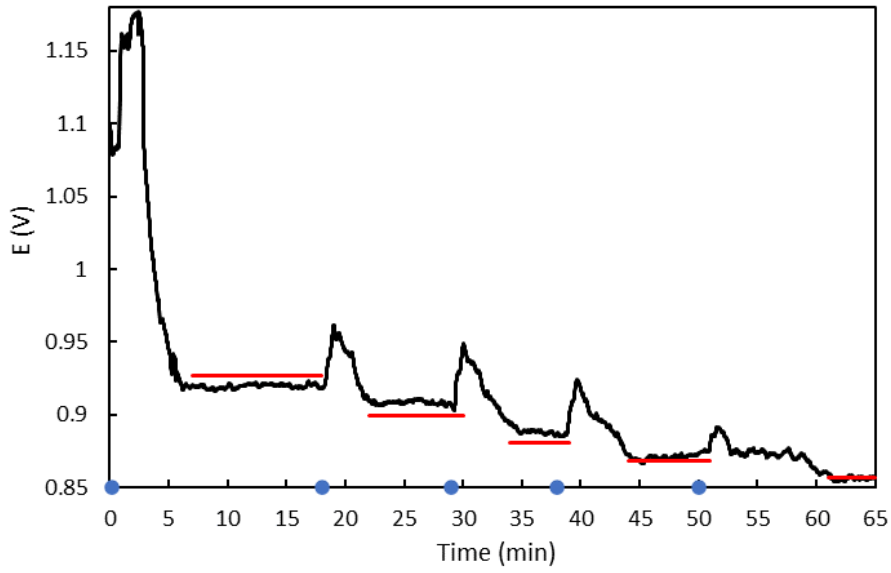

Figure 5.5: Emf between the alumina probe vs. time (black line), expected values from calculations (red line), time of addition of 2 wt% secondary alumina (blue circles).

All these values are summarized in Table 5.1. The table shows that the decrease in the calculated potential values are somehow comparable with the decrease in the measured potentials in the range 3-5 wt%, and becomes better in the ranges 5-7 wt%, 7-9 wt% and 9-11 wt%.

Table. 5.1 Theoretical and experimental potential values for different ranges of alumina concentration.

Range of alumina concentration (wt%)	Calculated values		Experimental	
	Potential interval (V)	Potential decrease (V)	Potential interval (V)	Potential decrease (V)
0.25-1	1.06-0.99	0.07	-	-
1-3	0.99-0.93	0.06	1.08-0.92	0.16
3-5	0.93-0.90	0.03	0.92-0.91	0.01
5-7	0.90-0.88	0.02	0.91-0.89	0.02
7-9	0.88-0.87	0.01	0.89-0.87	0.02
9-11	0.87-0.86	0.01	0.87-0.86	0.01

Moreover, the dissolution time for the alumina was obtained from the analysis of the results showed in Figure 5.5. The dissolution time was taken from the moment when the alumina was added until the time when the potential reached a steady value. Table 5.2 shows the dissolution time for every addition of 2 wt% of secondary alumina. It shows that the dissolution time for the first 2 wt% of alumina is approximately 5 minutes, and it increases gradually for the following additions.

Table. 5.2 Dissolution time measurements for 2 wt % additions of secondary alumina using the alumina probe.

Secondary alumina		
Number of addition	**Range of alumina concentration (wt%)**	**Time (min.)**
First	1-2	5
Second	2-4	6
Third	4-6	7
Fouth	6-8	9
Fifth	8-10	12

Measurements for the primary alumina are not shown in the present work. Nonetheless, Bracamonte et al. [8] presented dissolution times for 3 wt% additions of primary alumina using the same electrochemical alumina probe. The data revealed larger dissolution times for the primary alumina. These values are presented in Table 5.3.

Table. 5.3 Dissolution time measurements for 3 wt% additions of primary alumina using the alumina probe [8].

Primary alumina		
Number of addition	**Range of alumina concentration (wt%)**	**Time (min.)**
First	1-3	12
Second	3-6	15
Third	6-9	19
Fourth	9-12	23

Data from Table 5.2 and 5.3 is presented in Figure 5.6. Figure 5.6a illustrates that the curve for secondary alumina has a steeper slope than the primary alumina. It is also evident that the time to dissolve 3 wt% of primary alumina is more than two times larger than the time needed to dissolve the same amount of secondary alumina. When the melt reaches the saturation point for alumina, the dissolution time for secondary alumina is around 12 minutes whereas for the primary alumina the dissolution time is slightly under 25 minutes. As the alumina addition amount is not the same (3 wt% vs. 2 wt%) the comparison only gives an indication. Figure 5.6b illustrates that the dissolution rate for secondary alumina is larger than for the primary alumina, especially at low alumina concentrations. The decrease in dissolution rate for both aluminas with increasing alumina concentration is evident.

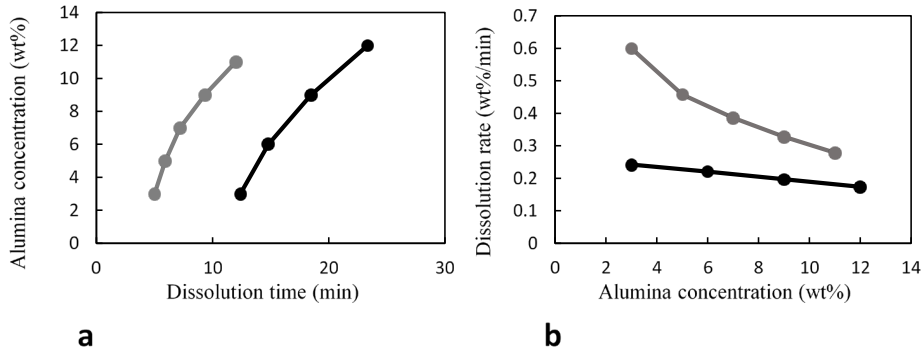

Figure 5.6: a Alumina concentration for 3 wt% additions of primary alumina (black line) and for 2 wt% additions of secondary alumina (grey line). **b** Dissolution rate of primary alumina (black line) and secondary alumina (grey line).

5.4.2 Visual Observations

Figure 5.7 shows pictures for the addition and the dissolution process of primary alumina. The pictures are selected from the video recording using the high-speed camera. Figure 5.7a shows the quartz crucible with the initial bath before the feeding. Immediately after addition, the alumina penetrated approx. 2 cm into the melt, Figure 5.7b. At 4 seconds, Figure 5.7c, a crust has formed, and dispersed

alumina particles undergo rapid dissolution in the upper part of the melt. At 120 seconds, Figure 5.7d, a thicker crust has formed and detachment and sinking of flakes were observed. The flakes probably consist of alumina particles in a bath matrix, with density greater than the bath [14]. In the following 180 seconds bigger flakes detached from the crust and sank, Figure 5.7e. A relatively thick crust remained on the top of the bath even 400 seconds after the alumina addition, Figure 5.7f, and illustrates that the dissolution process was far from completed.

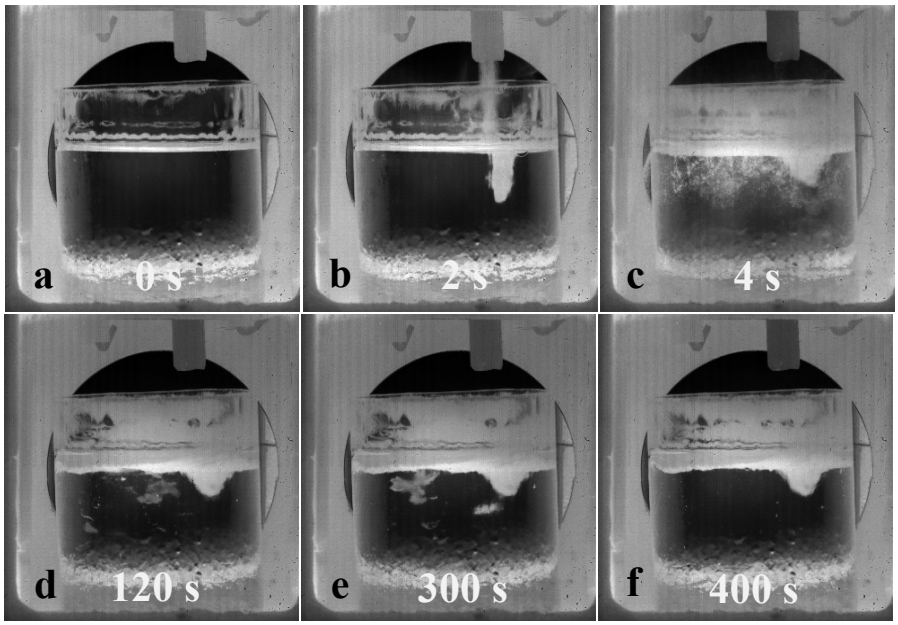

Figure 5.7: Selected pictures for the dissolution process of a 1 wt% primary alumina addition. **a** 0 second **b** 2 seconds **c** 4 seconds **d** 120 seconds **e** 300 seconds **f** 400 seconds. Initial alumina concentration is approx. 1 wt%.

In the same way, Figure 5.8 shows the selected pictures for the addition and the dissolution process of the secondary alumina. Figure 5.8a shows the quartz crucible with the bath and some fume outside the crucible before the feeding. Approx. 2 seconds after the feeding of alumina, Figure 5.8b, the alumina penetrated the melt followed by a fast spread of some alumina particles forming a cloud. Figure 5.8c and 5.8d show a fast dispersion of the alumina particles through

the whole bath. At 120 seconds, Figure 5.8e, a significant amount of alumina was completely dissolved. Moreover, sinking of small alumina/bath agglomerates were also observed. Finally, after 180 seconds the alumina was completely dissolved, Figure 5.8f.

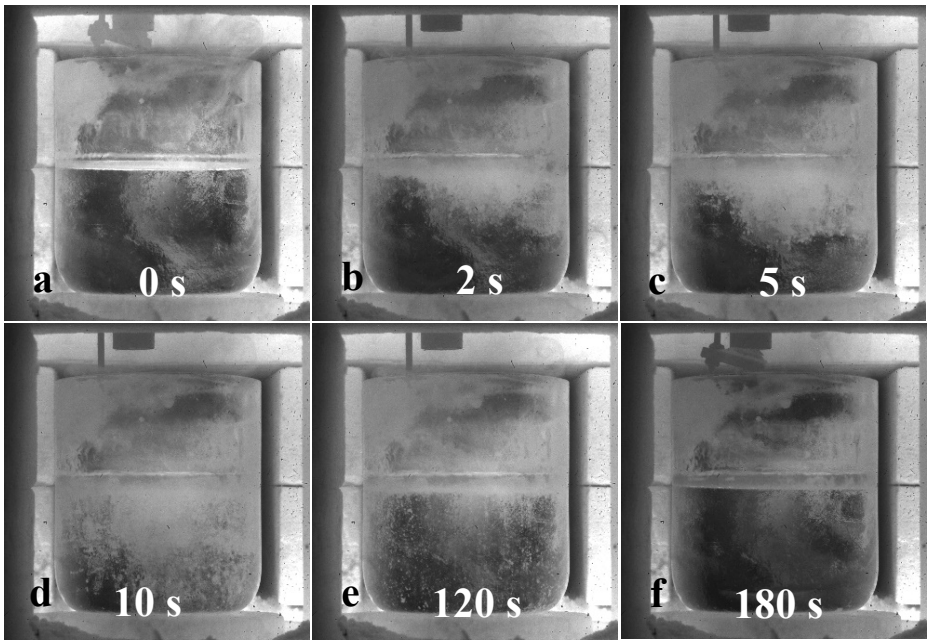

Figure 5.8: Selected pictures for the dissolution process of a 1 wt% secondary alumina addition **a** 0 second **b** 2 seconds **c** 5 seconds **d** 10 seconds **e** 120 seconds **f** 180 seconds. Initial alumina concentration is approx. 1 wt%.

Overall, these results highlight the differences in the dissolution process between primary and secondary alumina. The most noticeable difference is in the required time to dissolve, making evident that the dissolution process of the secondary alumina is considerably faster than the dissolution of the primary alumina. Furthermore, the pictures also suggest a different mechanism to dissolve for each type of alumina. The dissolution process for the primary alumina was characterized by the formation of a big crust on the top of the melt followed by the detaching and sinking of alumina flake-shaped particles. On the contrary,

almost no crust formation was seen for the secondary alumina and the dissolution process was mainly characterized by a rapid dispersion of all the particles throughout the whole cryolite melt forming a cloud until the dissolution was finished. The reasons for the better dispersion and less aggregation demonstrated by the secondary alumina could be related to the tendency of the secondary alumina to have a better flowability at higher HF contents [15].

These experiments were repeated three times for the primary and secondary alumina. Even though the dissolution times for every 1 wt% addition of alumina varied a few seconds for each experiment, the dissolution behaviour was always the same.

5.4.3 Particle size distribution and morphological surface analysis

Figure 5.9 shows SEM images of the particles in the aluminas. From analysis of two micrographs for each alumina, a particle size distribution was established, Table 5.4. Even though the statistical material for the particle size distribution is small, the data indicates that the secondary alumina has larger particle size than the primary alumina. This is opposite to what is expected because the amount of fines is reported to always increase during the dry scrubber process. No explanation for this distribution has been found. However, both the larger particle size as well as the increased fluoride surface concentration from adsorbed HF point in the direction of faster dissolution for the secondary alumina [16], which in fact was also observed both for the emf measurements and the visual observations.

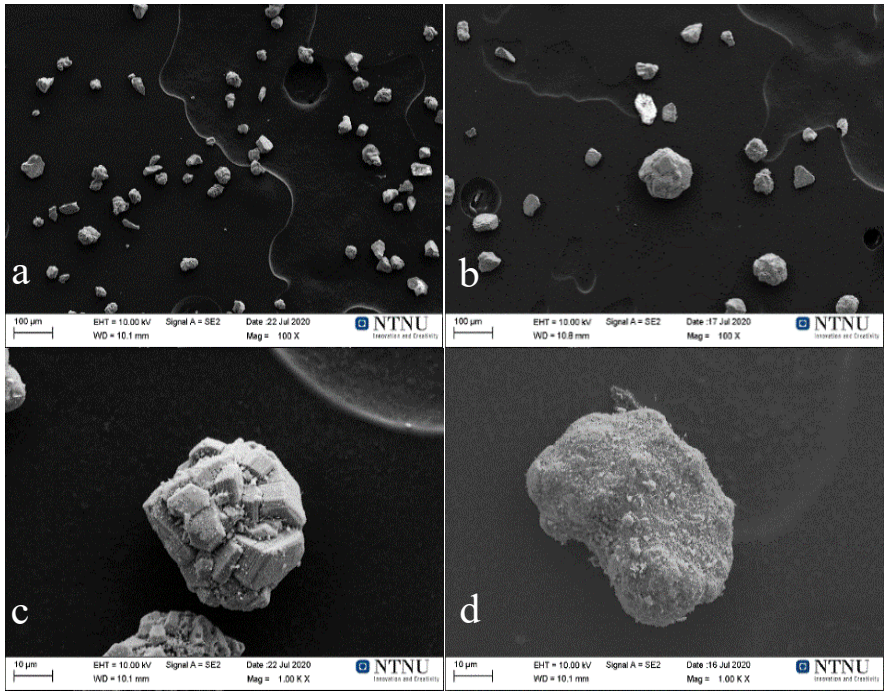

Figure 5.9: SEM pictures. Particle size for **a** Primary alumina **b** Secondary alumina. Surface morphology of **c** Primary alumina **d** Secondary alumina.

Table. 5.4 Summary of the particle size distribution for the primary and the secondary alumina.

	Particle size distribution				
Alumina	**1-19 µm**	**20-39 µm**	**40-59 µm**	**60-79 µm**	**≥ 80 µm**
Primary	26 %	46 %	23 %	2 %	3 %
Secondary	10 %	28 %	39 %	14 %	9 %

Furthermore, SEM analysis also revealed differences in the surface morphology of the primary alumina and the secondary alumina. Figure 5.9c shows that the primary alumina had a very compact surface conformed by many laminate-shaped sections whereas Figure 5.9d revealed that the secondary alumina had a surface characterized by the presence of pores. Moisture together with the HF adsorbed on the secondary alumina might be a cause for the shattering of the particles upon the dissolution of the secondary alumina preventing agglomeration. A more fragmented alumina will have more contact area with the melt, and it will dissolve faster [17]. On the contrary the compact surface of the primary alumina suggests that little shattering occurs, leading to agglomerations and a slower dissolution process.

5.5 Conclusion

The emf measurements indicated that the alumina probe is a promising tool for measuring the alumina concentration in cryolite based melts. The sensor gave values in fair agreement with the potentials calculated from the Nernst equation. Although the emf measurements gave stable values after the dissolution process had completed, there is an abrupt and significant rise in the potential of the sensor immediately after alumina addition. Oxygen and humidity entering the melt because of the alumina addition is believed to cause the sudden increase in the potential of the sensor. The dissolution rates obtained using the sensor demonstrated a significant faster dissolution process for the secondary alumina. The results from the application of a high-speed camera and a see-through cell for documenting the alumina addition and dissolution process seem to be in fair accordance with the emf measurements, revealing a considerably shorter time needed for the secondary alumina to dissolve. The visual observations also revealed different dissolution behaviour for primary and secondary alumina. The dissolution behaviour for the primary alumina was characterized by the formation of a crust after feeding, followed by a slow dissolution including detachment of flakes probably consisting of alumina particles in a bath matrix. The dissolution mechanism for the secondary alumina was characterized by rapid dispersion of all the particles throughout the whole melt leading to a faster dissolution.

References

1. Grjotheim K, Kvande H (1993) Introduction to aluminium electrolysis: understanding the hall-heroult process. Aluminium-Verlag, Dusseldorf
2. Thonstad J, Solheim A, Rolseth S, Skar O (1988) The dissolution of alumina in cryolite melts. Essential Readings in Light Metals, 105–111
3. Haverkamp RG, Welch BJ (1998) Modelling the dissolution of alumina powder in cryolite. Chemical engineering and processing 37, 177-187
4. Thonstad J (1967) Critical current densities in cryolite melts. Electrochimica Acta, Vol 12, 1219-1226
5. Thonstad J (1972) Dissolution of alumina in molten cryolite. Metallurgical Transactions, Vol 3, 408
6. Vasyunina NV, Vasyunina IP, Mikhalev YG, Vinogradov AM (2009) The solubility and dissolution rate of alumina in acidic cryolite aluminous melts. Russian Journal of Non-Ferrous Metals, 50(4):338–342
7. Kim Y (2020) Applicability of the Electrochemical Oxygen Sensor for In-Situ Evaluation of MgO Solubility in the MgF2–LiF Molten Salt Electrolysis System. Metals, 10, 906
8. Bracamonte L, Nilsen K, Rosenkilde C, Sandnes E (2020) Alumina Concentration Measurements in Cryolite Melts. Light Metals 2020.
9. Haupin WE (1974) See-through Hall-Héroult cell. Light Metals 1974
10. Yang Y, Gao B, Wang Z, Shi Z, Hu X (2015) Study on the Dissolution of Alumina in Cryolite Electrolyte Using the See-Through Cell. Light Metals 2015
11. Yang Y, Gao B, Wang Z, Shi Z, Hu X (2015) Effect of Physiochemical Properties and Bath Chemistry on Alumina Dissolution Rate in Cryolite Electrolyte. JOM, Vol 67, No 5
12. Haarberg GM, Osen KS, Thonstad J (1993) Measurement of electronic conduction in cryolite alumina melts and estimation of its effect on current efficiency. Metallurgical Transactions B. Vol 24B, 729-735

13. Sommerseth C (2016) The effect of production parameters on the performance of carbon anodes for aluminium production. Ph.D. thesis, Norwegian University of Science and Technology, NTNU

14. Gylver, S (2019) The micro-and macrostructure of alumina raft. Light Metals 2019.689-696

15. Haverkamp RG, Welch BJ (1994) The influence of fluorination on the dissolution rate of alumina in smelter electrolyte. Light Metals 1994, 365-370

16. Wai-Poi N, Welch BJ (1994) Comparing alumina quality specifications and smelter expectations in cells. Light Metals (1994), 345-350

17. Liu X (1994) Visualization of alumina dissolution in cryolite melts. Light Metals (1994) 359-354

Chapter 6 Oxide Sensor Measurements and Simultaneous Optical Observations During Dissolution of Alumina in Cryolite Melt

Luis BRACAMONTE[1], Kristian Etienne EINARSRUD[1], Christian ROSENKILDE[2], Espen SANDNES[1,]*
[1]Department of Materials Science and Engineering, NTNU Norwegian University of Science and Technology, Trondheim, Norway
[2]Nork Hydro ASA, Hydro's Corporate Technology Office, Norway

Submitted and accepted in Light Metals 2022

Abstract
Faster dissolution of alumina is one of the key challenges for improvement of the energy efficiency and production rate increase of Hall-Héroult electrolysis cells. To obtain a faster dissolution a better knowledge of the phenomena involved in the alumina dissolution process becomes important. In this work, an alumina sensor based on the electromotive force principle was applied to measure the concentration of dissolved alumina in a cryolite based melt from the addition of the alumina throughout the entire dissolution process. Simultaneously, the dissolution process was video recorded. The measurements were performed in a quartz crucible and alumina was added in 1 wt% subsequent additions. Three different industrial aluminas were tested. The general working principle of the sensor was studied, and the information extracted from the video recordings was used to explain the sensor results as well as the general dissolution phenomena. The total dissolution time found based on the sensor results and video recording were compared for different alumina concentrations. The influence of stirring of the melt was also studied.

6.1 Introduction

The dissolution of alumina in aluminium reduction cells is a complex process which involves several steps. During the feeding a crust is formed around the alumina particles when the bath freezes, followed by heating and re-melting of the crust around the alumina particles. Gamma-alumina goes through a phase transition to alpha-alumina which then dissolves [1,2]. Moreover, the dissolution process is affected by several conditions such as bath composition, bath temperature, and alumina properties among others. Due to the complexity of the process a method to perform in-situ alumina concentration measurements during the dissolution will lead to information for characterizing the alumina-bath interaction and bring to light the variables that influence the dissolution characteristics and dissolution rate of alumina. This information can be valuable to later improve the industrial alumina feeding and dissolution process. Haverkamp and Thonstad developed methods to measure the concentration of alumina based on electrochemical techniques such as linear sweep voltammetry (LSV), critical current density (CCD) and chronopotentiometry [3,4,5]. Other researchers have focused on electromotive force (emf), a technique which has been experimented with in lab scale in several molten salt systems [6,7]. Visual observations have also been used to extract information about the dissolution of alumina. Using transparent cells Yang et al. studied the raft formation and dissolution rates of different aluminas with known physicochemical properties in cryolite based melts [8,9]. The aim of the present work was to create a good basis for extracting detailed information from the dissolution process. Video recordings of the alumina dissolution in a transparent quartz crucible were performed. In the same quartz crucible, a relatively simple emf-based alumina sensor was simultaneously used to follow the amount of dissolved alumina from the addition and throughout the whole dissolution process. The total dissolution time for both techniques was compared. Images from the video recordings lead to a better understanding of the performance of the sensor. Simultaneous images from visual observations and in-situ alumina sensor measurements have previously not been reported.

6.2 Method

The half-cell reactions for the alumina sensor and a quasi-reference electrode are derived together with the corresponding Nernst equation. The alumina sensor is a graphite electrode immersed in the bath (Chamber I). The potential of the sensor is measured against the quasi-reference electrode with an undefined potential. The

quasi-reference electrode consists of a graphite electrode immersed in a bath with the same composition as for the sensor but saturated with alumina (Chamber II). Thus, the potential between the sensor and the quasi-reference is due to the difference in activity of alumina in the two chambers. The principle of the alumina sensor is shown on the upper part in Figure 6.1.

The half-cell reactions for the alumina sensor and the quasi-reference electrode are shown in Equations 6.1 and 6.2, respectively. Equation 6.3 represents the migration of sodium ions from chamber I to chamber II in order to maintain charge neutrality. In Equation 6.3, t_{Na+} is assumed equal to 1 [10]. However, the addition of 3.5 wt% LiF in the experiments makes the assumption more uncertain. The reason why LiF was added is explained in the experimental part. The total cell reaction is shown in Equation 6.4.

$$\text{Half} - \text{cell rx chamber I} \qquad O^{2-}_{(I)} + C_{(I)} = 2e^- + CO_{(I)} \qquad (6.1)$$

$$\text{Half} - \text{cell rx chamber II} \qquad CO_{(II)} + 2e^- = C_{(II)} + O^{2-}_{(II)} \qquad (6.2)$$

$$\text{Ionic transport} \qquad 2\, t_{Na^+_{(I)}} = 2\, t_{Na^+_{(II)}} \qquad (6.3)$$

$$\text{Total cell rx} \qquad C_{(I)} + CO_{(II)} + Na_2O_{(I)} = CO_{(I)} + C_{(II)} + Na_2O_{(II)} \qquad (6.4)$$

As E^0 is equal to 0, the Nernst equation for the cell reaction becomes as written in Equation 6.5, where n is equal to 2.

$$E = -\frac{RT}{nF} \ln \frac{P_{CO_{(I)}} \cdot a_{Na_2O_{(II)}} \cdot a_{C_{(II)}}}{P_{CO_{(II)}} \cdot a_{Na_2O_{(I)}} \cdot a_{C_{(I)}}} \qquad (6.5)$$

The activity of CO is expressed as the partial pressure of CO above the melt since the adsorbed CO is believed to be in equilibrium with dissolved CO which is also in equilibrium with the pressure of CO above the melt. The expression in Equation

6.5 can be simplified to Equation 6.6 as $a_{C_{(I)}}$ is equal to $a_{C_{(II)}}$ because the same graphite material is used in both electrodes, and with the assumption that the CO pressure is constant and equal in chamber I and II.

$$E = -\frac{RT}{2F} \ln \frac{a_{Na_2O_{(II)}}}{a_{Na_2O_{(I)}}} \quad (6.6)$$

By using data from FactSage (ThermFact Inc., Montreal, Canada) it can be found that a_{Na_2O} is roughly linearly related with the alumina concentration. This implies that the activity coefficient of Na_2O is approximately constant. Since the bath composition is the same in chamber I and II, Equation 6.6 simplifies to Equation 6.7.

$$E = -\frac{RT}{2F} \ln \frac{wt\%\ Al_2O_{3\ (II)}}{wt\%\ Al_2O_{3(I)}} \quad (6.7)$$

Finally, the potential of the alumina sensor can be expressed as a function of the alumina concentration. The calculated values are given on the lower part of Figure 6.1

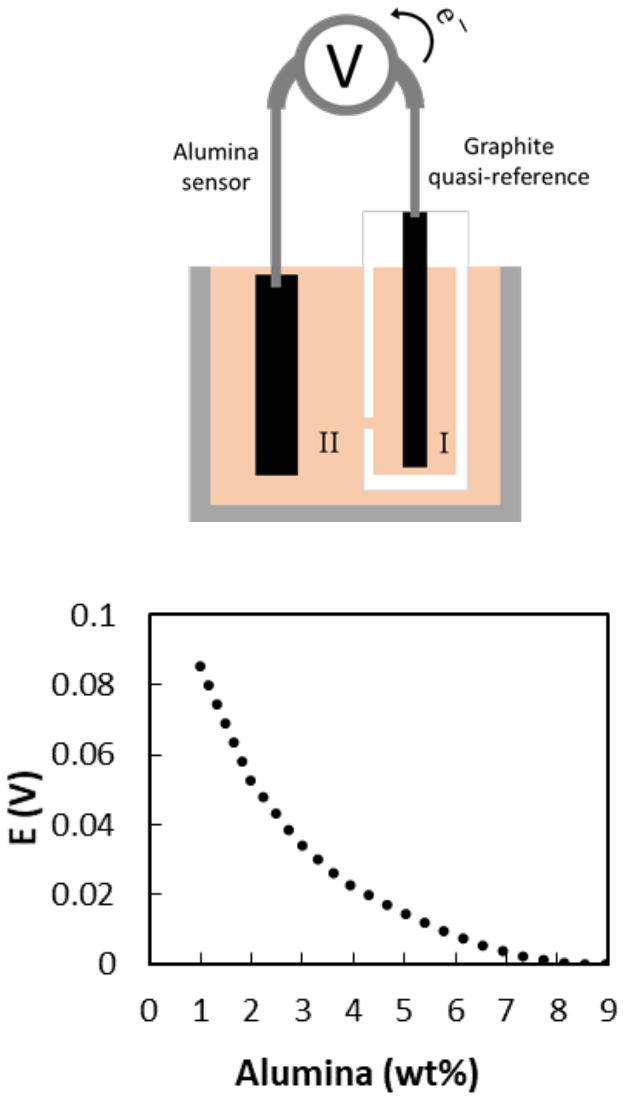

Figure 6.1: Upper part: Schematic of the alumina sensor. Lower part: Calculated values of the potential of the alumina sensor vs. the quasi-reference electrode as a function of alumina concentration (T = 950 ˚C, the corresponding alumina saturation is $\mathbf{8\ wt\%\ Al_2O_{3(l)}}$).

6.3 Experimental work

6.3.1 Design of the alumina sensor

The alumina sensor is shown in the upper part of Figure 6.2. The probe is a graphite rod (Ø 1 cm, h 5 cm) shielded with a boron nitride tube on the top. The purpose of the shielding is to hinder the reaction with air possibly present above the melt and to prevent the carbon to be in contact with the crust after feeding. The probe was made of the same graphite material as the graphite rod used for the quasi-reference electrode**.**

The quasi-reference electrode is based on a graphite rod (Ø 0.5 cm, h 5 cm) which was screwed to a graphite connector and put inside a boron nitride tube ($Ø_{inner}$ 1 cm, $Ø_{outer}$ 2.5 cm). A hole (Ø 0.1 cm) was drilled above the bottom of the tube to ensure ionic contact between the alumina saturated bath inside the tube (chamber I) and the bath in the crucible (chamber II). A stainless-steel rod was screwed to the graphite connector. Alumina powder (2.5 g) was added inside the boron nitride tube to make an alumina saturated bath (approximately 8 wt%).

6.3.2 Electrolyte and alumina

The experiments were performed using 250 g of bath. The initial composition was synthetic cryolite (74 wt%), aluminium fluoride (15 wt%), calcium fluoride (6.5 wt%), lithium fluoride (3.5 wt%). The synthetic cryolite contained approximately 1 wt% of alumina. The use of LiF lowered the liquidus point of the bath allowing to operate the furnace at lower temperatures resulting in longer lifetime of the crucible and materials inside the furnace. For the additions three different industrial-grade secondary aluminas were used. Some of their physicochemical properties are shown in Table 6.1.

Table 6.1 Physicochemical characteristics of the different aluminas.

Alumina	MOI 300 °C (%)	LOI 1000 °C (%)	BET (m^2/g)	γ-alumina (%)	Particles ≤ 45 µm (%)
A	1.70	2.33	69.8	38.1	15
B	2.65	2.11	65	37.2	10
C	1.50	1.86	73.9	39.7	10

6.3.3 Experimental set-up and procedure

The experimental set up is shown in the lower part of Figure 6.2. A transparent quartz crucible (Ø 6.5 cm, h 7.5 cm) was used to contain the bath. The crucible was placed inside a see-through furnace with quartz windows on the sides. The furnace was custom-made from Entech Energiteknik AB. Nitrogen was flushed from both windows (100 mL/min.) to prevent vapors and particles from sticking to the windows thereby enhancing the visibility. The furnace was not completely sealed so the nitrogen gas inside the furnace could contain small amounts of oxygen from the ambient air. A stainless-steel tube (Ø 1.5 cm, h=30 cm) together with a funnel was used for the additions of alumina. The melt temperature was measured with a thermocouple type S and was kept around 950 °C prior to additions. The theoretical liquidus temperature was around 922 °C given a superheat of approximately 28 °C. The relatively high superheat was necessary to avoid freezing of the bath due to the absence of insulation material and heating elements in the see-through zone. In addition, the effect of convection in the electrolyte was also studied applying a stainless-steel rod stirrer at a constant rotation speed of 200 rpm. The emf between the alumina probe and the graphite quasi-reference electrode was measured before and during the addition of alumina and throughout the entire dissolution process for all the experiments. A Data Acquisition System (DAQ) measurement hardware (NI 9205) was used for obtaining the emf data.

Simultaneous video recording during the additions and dissolution process of the alumina was performed using a high-speed camera (Photron Fastcam Mini AX) and a digital single-lens reflex camera (Sony) located in front of the windows of the oven. The images shown in the present work are all taken from the high-speed camera due to its high-quality images suitable for extracting the dissolution characteristics. The high-speed camera could only serve for the first five minutes of the dissolution process due to limitations in memory capacity. The digital single-lens reflex camera was used to record the whole dissolution process for each alumina addition and to estimate the dissolution time.

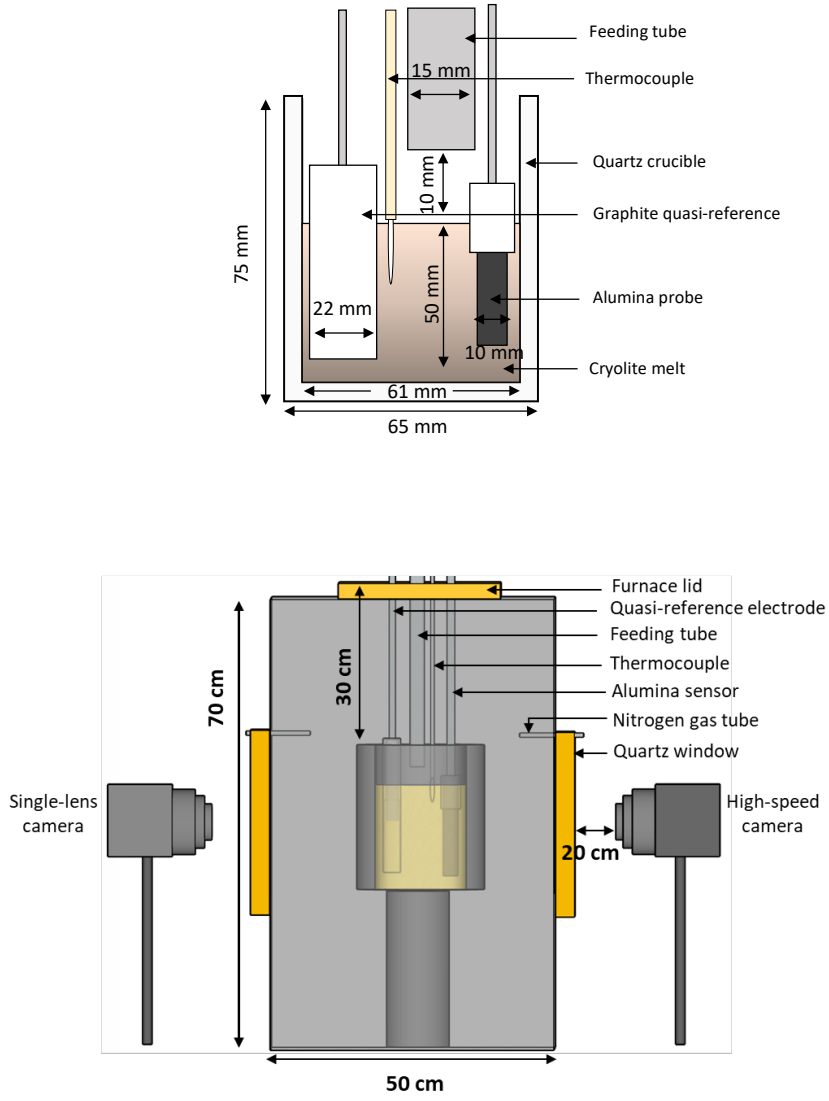

Figure 6.2: Upper part: sketch of the quartz crucible with the alumina sensor and the graphite quasi-reference electrode. Lower part: Principal sketch of the see-through furnace. The alumina feeding tube and the thermocouple are also inserted through the lid. The high-speed camera is shown on the right and the single-lens camera on the left.

Four subsequent additions of 1 wt% of Alumina A, B and and C were performed. The feeding tube was placed approximately 1 cm above the melt. The time from the first alumina particle hit the surface until the last particle hit was in the range between 0.5 to 1.5 seconds. The addition is considered as finished when the last particle has hit the melt. The time stamp for pictures later presented refer to the completion of the addition.

6.4 Results and Discussion

6.4.1 Interpretation of sensor data and video recordings

The emf data and the melt temperature for the dissolution of Alumina A are presented in Figure 6.3. In general, after each addition the emf curve shows a decrease, which is interpreted as an increase in the alumina concentration. Then, the potential stabilizes and reaches more or less a constant value when the dissolution process is closed to completion. For the first addition, the emf curve shows a fast decrease before the potential reached a horizontal plateau suggesting that the dissolution process was completed, while less pronounced drops and slightly inclining plateaus were observed for the subsequent additions.

The time when each alumina addition was performed and the the time when the dissolution was estimated to be finished based on the alumina sensor and video recordings are also showed in the figure. Based on the video recordings, the dissolution process was considered to be finished at the moment when no trace of crust or rafts was seen in the bath. This time could be decided with an estimated accuracy of approximately ± 0.2 minutes. The inaccuracy arises from transparency limitations of the crucible in addition to difficulties being able to see small rafts through the meniscus that the melt made on the surface of the quartz crucible walls.

For additions number 2 and 3 the dissolution process has finished before the inclination of the plateau appears. The inclination is therefore assumed to be drifting of the sensor. The cause of the drifting is not understood. In Figure 3 the green dashed lines shows the linear regression lines associated with the drifting ocurring from the end of the dissolution process to the next addition. The average of the slope of these two lines is used for the correction of the sensor data in the same time range. This correction is done for addition numbers 2, 3 and 4 and the corrected values are represented by the red lines. The purpose of the correction is to be able to more accurately estimate the dissolution time based on the sensor data. In the estimation, a horizontal line was drawn from the time when the

dissolution was estimated to be completed based on the video recording to the time of the addition. The line is positioned on the plateau value and extended back to the time of the addition. The time when the horizontal line started to deviate from the emf curve was taken as the time when the dissolution was completed. This time could be decided with an estimated accuracy of approximately ± 0.4 minutes. The inaccuracy arises from the fluctuations in the curve making it impossible to define one specific time as the end of the dissolution.

The measured potential values were generally not in agreement with the calculated values for all the aluminas. The difference arises from simplifications done in the deduction of the Nernst equation and the sensitivity of the sensor to variations of the gas concentration in or above the melt. Despite this difference, the general behaviour of the emf curve after each alumina addition makes it possible to estimate dissolution times, suggesting that the working principle for the sensor is partly confirmed.

Generally, temperature drops between 2 to 6 °C for the alumina additions were observed. This was comparable with previous studies [11]. The time from feeding until the temperature approaches the temperature before addition showed a slight agreement with the dissolution time based on video recording and sensor measurements, especially for the second and the third addition. Anyway, the relationship is loose, and the temperature data is not used in the further analysis

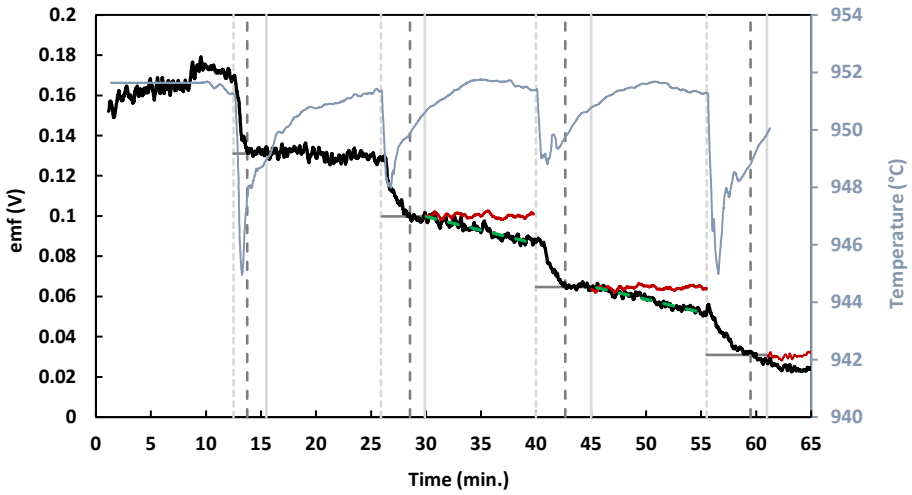

Figure 6.3: Emf of the alumina sensor and the melt temperature for additions of Alumina A. Emf (black line). Temperature (blue line). Time of addition (light-

grey short dashed line). Time for end of dissolution based on the video recording (light-grey line). Correction of the emf curve (red line). Linear regression line (green dashed line). Line for extension of the plateau (dark grey solid line). Time for end of dissolution based on the alumina sensor (dark grey long dashed line).

Figure 6.4 shows in detail the simultaneous emf measurement and the dissolution characteristics recorded by the high-speed camera for the first addition of Alumina A. Frame a) shows the situation before feeding. The quasi-reference is located on the left, the alumina sensor is on the right, and the thermocouple Pt and Pt-Rh threads are shown in the middle of the crucible. Upon addition, the alumina penetrated 2 cm into the bath, frame b). After one second, frame c), a fraction of the alumina penetrated the bath and rapidly dispersed forming a white cloud which underwent a rapid dissolution few centimeters down below the surface of the melt. Moreover, the other fraction of the alumina remained on the top of the bath forming a layer or crust with a lot of gas bubbles trapped inside. The bubbles inside the layer had an average size of about 1 mm in diameter. After 20 seconds, dissolution of the white cloud in the upper part of the crucible was observed, frames d), e) and f). This rapid dissolution is also observed in the fast decrease in the emf curve. Frame g) shows the situation after 1 minute. In a relatively short time, the crust had almost completely dissolved with only few small rafts of approximately 1 mm in diameter remaining on the surface. At this time, the emf curve is about to reach the plateau value. After 1.3 minutes the dissolution process was considered to be finished based on the alumina sensor data, illustrated by the dark grey dashed line. Almost no alumina particles were left in the crucible after 2.5 minutes, frame h). Frame i) shows a completely transparent bath with no alumina remaining neither in the crucible bottom nor at melt surface. Thus, based on the video recording the dissolution was considered to be finished after 3 minutes. In Figure 6.4 a lot of bubbles can be seen to have formed on the BN part of the quasi-reference. The origin of these bubbles is uncertain. Periodically the bubbles were released. Frame h) shows an example of a big bubble being released from the bottom of the BN part. Gas was also evolved on the graphite sensor. The gas evolution might have caused some noise in the emf curves and sometimes sudden convection increase in the bath.

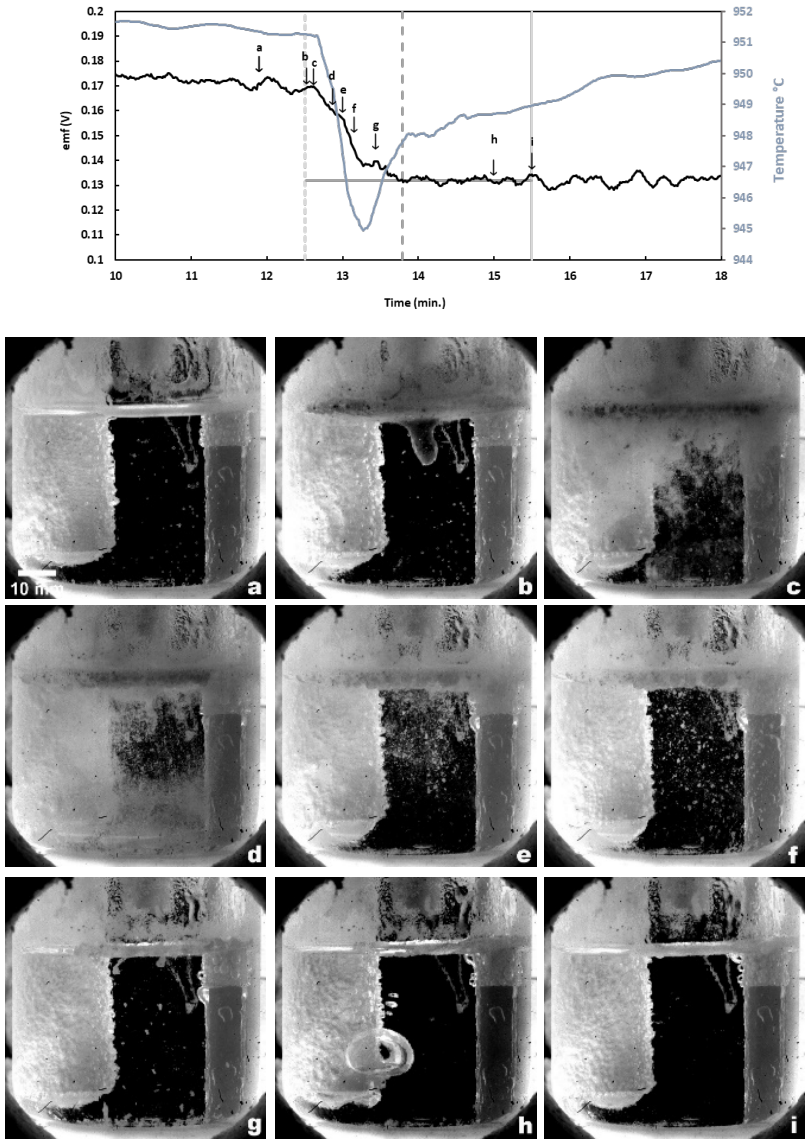

Figure 6.4: Simultaneous emf measurements and images from the dissolution process of the first addition of Alumina A **a** before addition **b** upon addition **c** 1 second **d** 20 seconds **e** 30 seconds **f** 40 seconds **g** 1 minute **h** 2.5 minutes **i** 3 minutes.

The emf data for the additions of Alumina B is presented on the upper part of Figure 6.5. For the first addition the emf decreased quickly before reaching an almost constant value. The principal shape of the emf curve resembles the shape of the emf curve for Alumina A, including the drift after the dissolution process has finished. Although not shown, the same principle for correction applies to Figure 6.5 as to Figure 6.3.

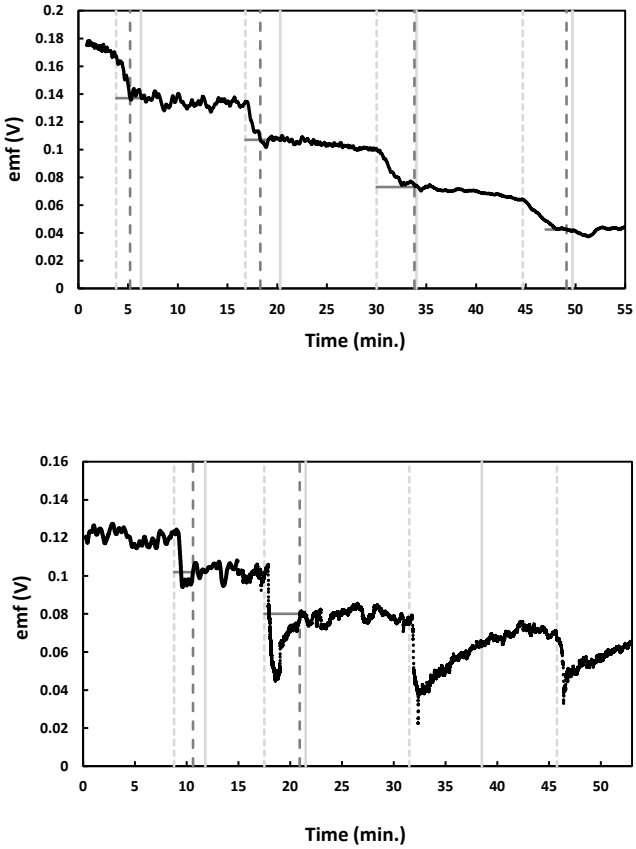

Figure 6.5: Upper part: emf of the alumina sensor for additions of Alumina B. Emf (black line). Lower part: emf of the alumina sensor for additions of Alumina C. Emf (black line) Time of each addition (light grey short dashed line). Time for end of dissolution based on the video recording (light-grey line). Line for extension of the plateau (dark grey solid line). Time for end of dissolution based on the alumina sensor (dark grey long dashed line).

Due to technical problems the sensor data from the first two addtions of Alumina C could not be obtained. For this reason the emf curve on the lower part of Figure 6.5 shows addition number 3, 4, 5, and 6. Here, it was possible to estimate the dissolution time only for the third and the fourth addition based on the alumina sensor measurements. Unlike the results obtained for Alumina A and B, the sudden emf drop after each addition was larger for Alumina C. The potential later increased and more or less stabilized forming a plateau. This type of behaviour of the emf can be explained by a lot of alumina ending up close to the sensor during or after feeding, increasing the concentration rapidly in the volume nearby the sensor. Afterwards the alumina concentration around the sensor decreases. The video recordings for Alumina C appear not very different to the video recordings for Alumina A and B, and thus can not explain the difference in the emf curve.

Figure 6.6 shows images from the fourth addition of Alumina A, with an initial bath concentration of approximately 4 wt% alumina. Contrary to the first addition, most of the alumina remained on the top of the bath forming a thicker crust with larger gas bubbles trapped inside. The bursting of the bubbles inside promoted the detachment and following sinking of smaller parts of the crust. These parts had flake-like shapes of 2 to 10 mm length, probably consisting of alumina particles in a bath matrix with density greater than the bath [12]. The whole dissolution process was completed after 5 minutes evidencing a significantly longer dissolution time. The same phenomenon was also observed for Alumina B and C at this higher initial concentration.

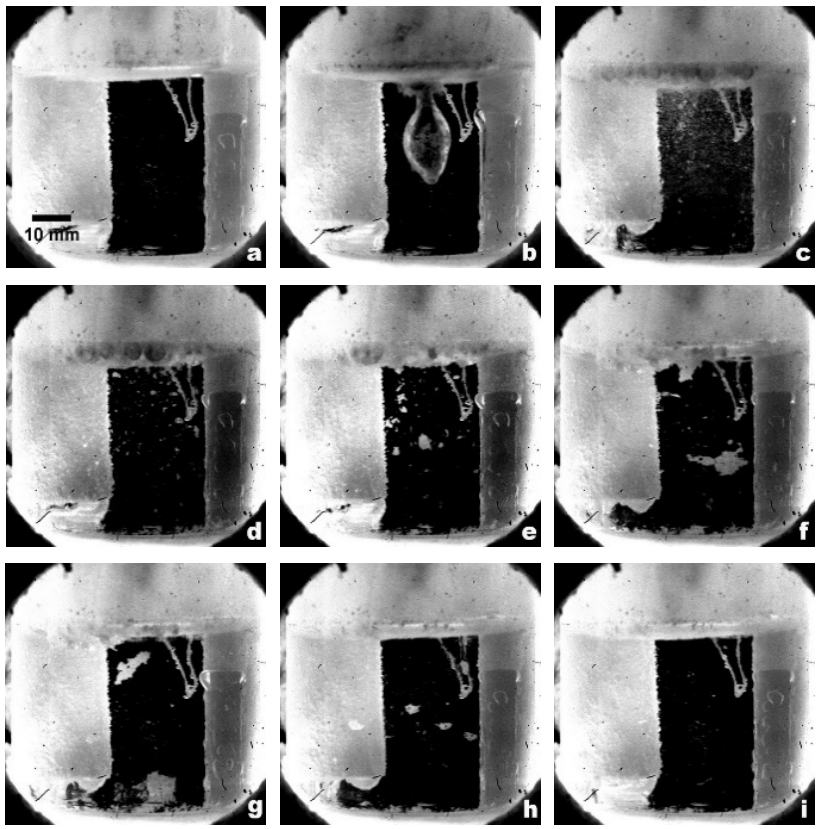

Figure 6.6: Selected images for the dissolution process of the fourth addition of Alumina A **a** before addition **b** upon addition **c** 1 second **d** 20 seconds **e** 30 seconds **f** 40 seconds **g** 41 seconds **h** 2.5 minutes **i** 5 minutes.

6.4.2 Dissolution time

A general trend was observed in the dissolution times based on the sensor for Alumina A, B and C, characterized by decreasing dissolution rate with increasing alumina concentration. This was reflected in the behaviour of the emf curve, with a fast decrease immediately after the first alumina addition and a less pronounced decrease as the initial alumina concentration increase in the subsequent additions. The same trend was observed in the dissolution times based on video recordings. Estimated dissolution times for all the aluminas are given in Table 6.2 and Figure 6.7.

The estimated dissolution times based on the alumina sensor were lower than the estimated times based on the video recordings. The reason for the lower values obtained using the alumina sensor might be related to the method for estimating the dissolution time from the emf curve as the emf curve probably obtained a plateau value before the remaining alumina in the crust was able to dissolve. The difference in the dissolution times based on the alumina sensor and video recordings was especially pronounce at lower initial alumina concentrations probably because a major part of the alumina dissolve quickly, as described in relation to Figure 6.4, while at higher initial alumina concentrations more of the alumina ended up in the crust making the dissolution times based on the sensor and video recordings to obtain more similar values. In general, the dissolution times obtained based on the sensor do not show a significant difference between the dissolution times of Alumina A and B. For Alumina C it is difficult conclude due to the lack of measurements. On the other hand, the video recordings together with the described method to estimate the dissolution time, indicate a significant difference in the dissolution times of the aluminas with respect to complete dissolution of the crust. The shorter dissolution times based on video recordings for Alumina C might be related with some physicochemical properties as its highest BET surface and lowest content of particles $\leq$ 45µm among the three aluminas. These properties are usually related with fast dissolution rates [9]. However, it is difficult to conclude because Alumina C also has the lowest LOI and MOI values among the aluminas, also properties related with fast dissolution rates.

Based on emf measurements, Yasinskiy et al. [13] reported alumina dissolution times between 3.7 and 6 minutes for subsequent 1 wt% alumina additions in a KF-AlF_3-Al_2O_3 melt at 750 °C. These dissolution times are slightly higher than for the present work, but this can be explained by the lower temperature

Table 6.2 Dissolution times of the aluminas based on the alumina sensor and video recordings.

Alumina	Alumina addition number	Dissolution time (min.) Alumina sensor (± 0.4)	Video recording (± 0.2)
A	1	1.3	3.0
	2	2.6	4.0
	3	2.7	5.0
	4	4.5	5.5
B	1	1.4	2.5
	2	1.9	3.5
	3	3.8	4.0
	4	4.4	5.0
C	1	Not measured	2.0
	2	Not measured	3.0
	3	1.8	3.0
	4	3.4	4.0

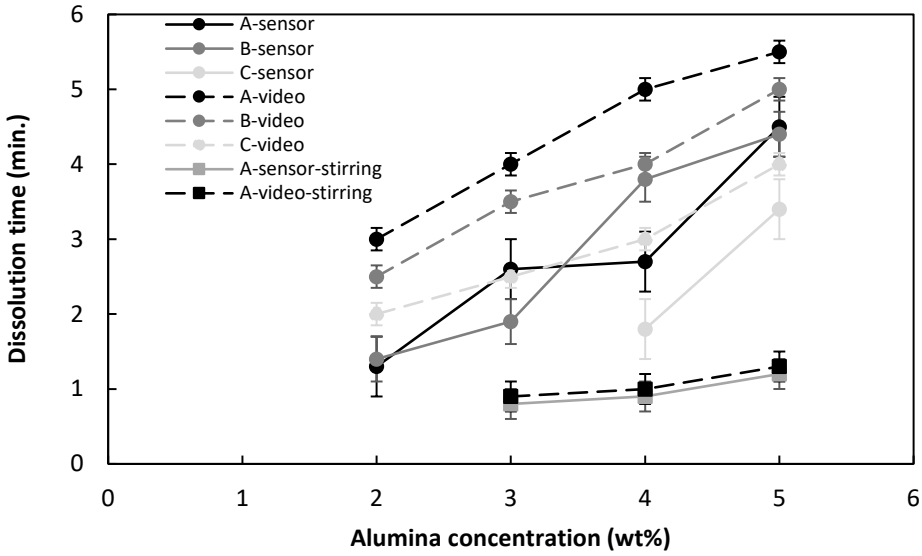

Figure 6.7: Dissolution times of the aluminas without stirring based on the alumina sensor (solid line with circles) and video recordings (dashed lined with circles). Dissolution times for Alumina A with stirring based on the alumina sensor (solid line with squares) and video recordings (dashed lines with squares).

6.4.3 Influence of stirring on the alumina dissolution

The obtained emf curve when stirring was applied is shown in Figure 6.8. The most significant differences compared to the experiments without stirring are a faster decrease in emf immediately after feeding and shorter time to reach the plateau values. For all additions a horizontal plateau was reached. The mechanical stirring promoted a rapid dispersion giving a faster dissolution of the alumina particles in the cryolite melt and possibly also to a large degree reducing crust formation. These observations agree with the results found by Yang [14]. The estimated dissolution times based on the video recordings and the alumina sensor are given in Table 6.3. These results suggest that the dissolution process is mainly limited by mass transport as reported by Haverkamp and Welch [15].

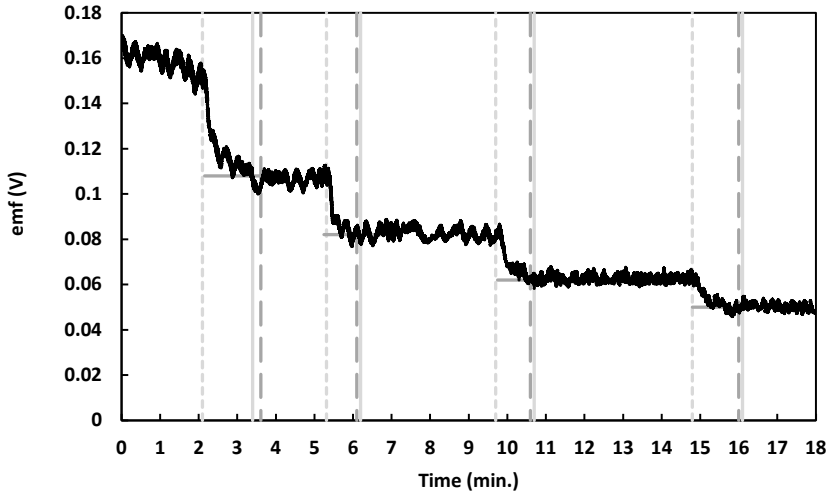

Figure 6.8: Emf of the alumina sensor for additions of Alumina A when mechanical stirring was applied (black line). Time of each addition (light-grey short dashed line). Time for end of dissolution based on the video recording (light-grey line). Line for extension of the plateau (dark grey solid line). Time for end of dissolution based on the alumina sensor (dark grey long dashed line).

Even though the dissolution time based on the sensor measurements for the first injection was rejected due small perturbations in the signal of the probe, the video recording of the addition was not affected and was still relevant for the investigation. Figure 6.9 shows the images for the first addition and dissolution process of Alumina A when stirring was applied. Upon addition, the alumina very

rapidly dispersed in the bath, and 1 second after addition was finished a 5 mm thick crust formed with bubbles less than 1 mm in diameter trapped inside it, frame c). After 2 seconds, the particles started to detach from the crust and rapidly dissolved before reaching the bottom of the crucible, frame d). Later, frames e-f), the bubbles inside the crust reached maximum size with average diameters of around 3 mm before bursting. At this time, part of the crust was already dissolved. The whole dissolution process was completed after approximately 1.4 minutes, frame i).

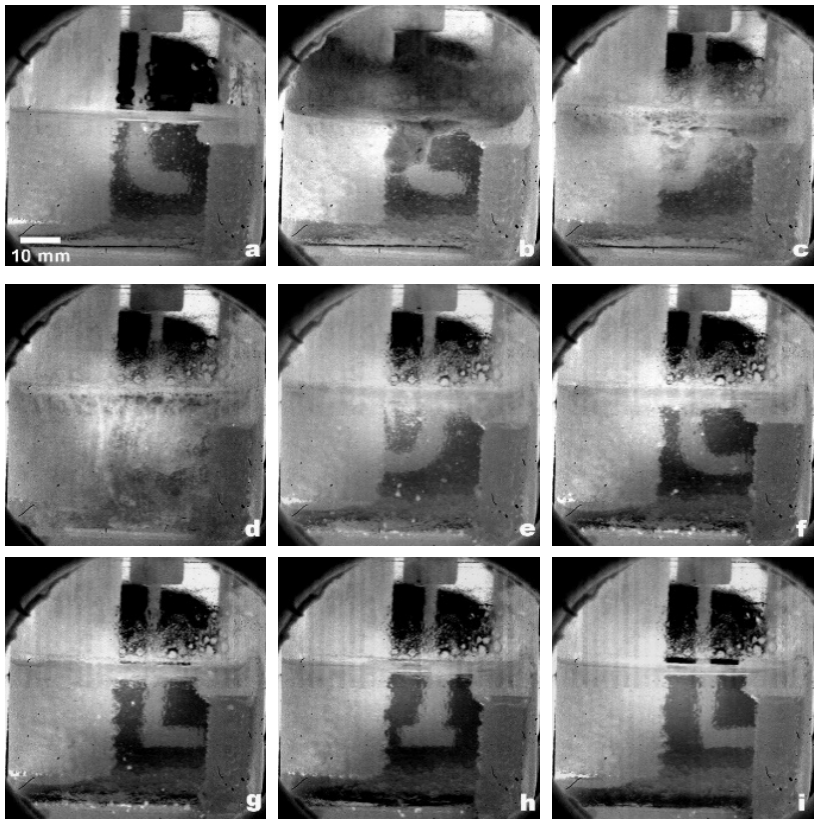

Figure 6.9: Selected images for the dissolution process of the first addition of Alumina A when mechanical stirring was applied. **a** before addition **b** upon addition **c** 1 second **d** 2 seconds **e** 6 seconds **f** 30 seconds **g** 45 seconds **h** 1 minute **i** 1.4 minutes.

When excluding the dissolution time obtained for the first addition due to technical problems with the stirrer for this addition, smaller deviation in the dissolution times based on the alumina sensor and video recordings were found,

Table 6.3 and Figure 6.7. This can be explained by the reduced crust formation. Also, the increased convection from stirring has made the dissolution time less affected by the initial alumina concentration.

Table 6.3 Dissolution times for Alumina A based on the alumina sensor and video recordings when stirring was applied.

Alumina addition number	Dissolution time (min.)	
	Alumina sensor (± 0.2)	Video recording (± 0.2)
1	Not measured	1.4
2	0.8	0.9
3	0.9	1.0
4	1.2	1.3

6.5 Conclusions

The emf curve obtained using the alumina sensor made it possible to estimate the dissolution times of the aluminas based on the initial decrease in emf immediately after alumina addition and the plateau value reached when most of the alumina was dissolved. The working principle for the sensor was only partly confirmed as the actual potential values were generally not in agreement with the calculated values. The video recordings revealed a rapid dispersion of the alumina immediately after addition. At lower alumina concentration a thin crust formed but the dissolution is mainly proceeding through the dissolution of a white cloud consisting of smaller dispersed alumina particles. The crust became thicker the higher the initial alumina concentration in the melt and it dissolved mainly by detachment and sinking of flake-shaped particles. The estimated dissolution times based on the alumina sensor and video recordings show an increase in the dissolution time with increasing initial alumina concentration. Introduction of convection by stirring the melt resulted in smaller dissolution times by reducing the amount of crust formation.

Acknowledgements

This work is partially funded by SFI Metal Production, Centre for Research-based Innovation, 237738. Financial support from the Research Council of Norway and the partners of SFI Metal Production is gratefully acknowledged

References

1. Lavoie P, Taylor M, Metson J (2016) A review of alumina feeding and dissolution factors in aluminium reduction cells. Metallurgical and Materials Transactions B, Vol 47B, 2690-2696.
2. Dassylva-Raymond V, Kiss L, Poncsak S, (2014) Modeling the behaviour of alumina agglomerate in the Hall-Héroult process. Light Metals 2014, 603-608. Wiley, Hoboken.
3. Haverkamp RG, Welch BJ (1998) Modelling the dissolution of alumina powder in cryolite. Chemical engineering and processing 37, 177-187.
4. Thonstad J (1967) Critical current densities in cryolite melts. Electrochimical Acta, Vol 12, 1219-1226.
5. Thonstad J (1972) Dissolution of alumina in molten cryolite. Metallurgical Transactions, Vol 3, 408.
6. Vasyunina NV, Vasyunina IP, Mikhalev YG, Vinogradov AM (2009) The solubility and dissolution rate of alumina in acidic cryolite aluminous melts. Russian Journal of Non-Ferrous Metals, 50(4):338–342.
7. Bracamonte L, Nilsen K, Rosenkilde C, Sandnes E (2020) Alumina Concentration Measurements in Cryolite Melts. Light Metals 2020.
8. Yang Y, Gao B, Wang Z, Shi Z, Hu X (2015) Study on the Dissolution of Alumina in Cryolite Electrolyte Using the See-Through Cell. Light Metals 2015.
9. Yang Y, Gao B, Wang Z, Shi Z, Hu X (2015) Effect of Physiochemical Properties and Bath Chemistry on Alumina Dissolution Rate in Cryolite Electrolyte. JOM, Vol 67, No 5.
10. Haarberg GM, Osen KS, Thonstad J (1993) Measurement of electronic conduction in cryolite alumina melts and estimation of its effect on current efficiency. Metallurgical Transactions B. Vol 24B, 729-735.
11. Kuschel G, Welch BJ (1990) Effect of alumina properties and operation of smelting cells on the dissolution behavior of alumina. Pasmico Research Center, Newcastle, Australia. Department Chemical and Material Engineering, University of Auckland, New Zealand.

12. Gylver, S (2019) The micro-and macrostructure of alumina raft. Light Metals 2019.689-696.

13. Yasinskiy A, Suzdaltsev A, Polyakov P, Padamata S, (2020) Behaviour of aluminium oxide in KF-AlF3-Al2O3 melts and suspensions, Ceramics International.

14. Yang Y, Gao B, Shi Z, Hu X (2015) The Formation and Dissolution of Crust Upon Alumina Addition into Cryolite Electrolyte. The Minerals, Metals & Materials Society. Vol 67. 2170-2180.

15. Haverkamp RG, Welch BJ (1998) Modelling the dissolution alumina powder in cryolite. Chemical Engineering and Processing. Vol 37, 177-187.

Chapter 7 Influence of Secondary Alumina Properties on Alumina Dissolution in Cryolite Melt

Luis BRACAMONTE[1], Sindre ENGZELIUS GYLVER[1], Kristian Etienne EINARSRUD[1], Espen SANDNES[1]
[1]Department of Materials Science and Engineering, NTNU Norwegian University of Science and Technology, Trondheim, Norway

Submitted to Metallurgical and Materials Transactions B in December 2021

Abstract
Alumina dissolution is one of the most important processes in the production of primary aluminium. The complexity of the dissolution of alumina relies on its dependency on several factors such as chemical and physical properties, feeding method, and chemistry and temperature of the electrolyte. The main goal of this work was to obtain the characteristics and the time of the dissolution process for different aluminas and evaluate a possible correlation with its physicochemical properties. Video recordings of the dissolution process of 1 wt% subsequent additions of alumina in a cryolite based melt contained in a quartz crucible were performed. Three different industrial secondary aluminas were used. The experiments were conducted with the alumina as received and also with only the fines fraction consisting of particles ≤ 45 μm. The particle size distribution was found to have the largest impact on the dissolution time as the fines fraction dissolved slower than the as received alumina. Physicochemical properties such as MOI, LOI, BET, and phase content was found to have less impact on the dissolution.

Chapter 8 Research Highlights

The purpose of this chapter is to tie together all the work and chapters into a common discussion

8.1 Study of the behaviour of the sensor. Comparison between the emf measurements and the calculations

The aim of the investigation was to study the performance of an electrochemical alumina sensor made of graphite and to understand its behaviour. The first objective was to analyse and compare the emf measurements with the theoretical calculations to verify the validity of the basis and assumptions used in this work. Thus, to verify these assumptions the first experiments were carried out in a sealed furnace, under nitrogen atmosphere with a simple bath composed only of 99% cryolite and 1 % alumina. The objective was to have few and simple variables to compare the experiments with the calculations. The emf measurements were performed during the addition of alumina and throughout the entire process of dissolution between the electrochemical alumina probe and two reference electrodes (an alumina saturated graphite quasi-reference electrode and an aluminium reference electrode). In addition, the half-cell reactions of the alumina sensor and the two reference electrodes were derived. The theoretical cell voltages were calculated and expressed as a function of the alumina concentration. It was found that the decrease in the potential in the emf measurements during the additions of alumina were consistent with calculations. These results mainly agreed with the fundamental working principle stated for the sensor. However, at this point the priciple of the sensor was not completely confirmed due to some behavoirs of the sensor which were not completely understood. There were some factors that caused sudden drops and jumps in the potential just after alumina addition as well as some drifting in the potential which appeared not to be related with the concentration of alumina. It was also observed that the emf measurements were strongly affected when exposed to the atmosphere, which happened when the lid of the oven was open during the alumina feeding. The potential increased when air entered the oven during the opening of the lid. The hypothesis made was that during the experiments under nitrogen gas, the entering of oxygen from the air into the furnace reacted with carbon from the probe or the crucible and altered the partial pressures of CO and CO_2 in the cell, which might have affected the potential values

Some experiments were carried out to better understand this behaviour. Substitution of N_2 with CO_2 was done to study the influence of having a gas composition rich in CO_2 above the melt. It was observed that air entering the furnace did not affect the emf measurements when CO_2 was used. The potential value remained constant when the lid was opened during feeding. It was believed that a constant flow of CO_2 can prevent large variations in the partial pressures of CO and CO_2. The added CO_2 seemed to establish a buffer system with respect to small amounts of air entering the cell. Based on these results, experiments where doses of alumina were added under CO_2 were carried out. However, under CO_2 the sensor decreased the sensitivity to the changes in concentration of alumina during the dissolution. This decrease in the sensitivity was probably due an excess of CO_2 flushed inside the furnace.

To further investigate the behaviour of the sensor, feeding of alumina was performed without opening the furnace during experiments under nitrogen gas. To avoid the removal of the plugs for the additions, the alumina was placed inside a chamber under nitrogen atmosphere. The chamber consisted of a syringe, which was connected to the feeding tube. The system was completely sealed, Figure 3.8 in Chapter 3. During the experiment, the inlet N_2 gas flow was set at 500 mL/min. The out gas was connected to a gas trap. At this gas flow, a frequency of one bubble per second was observed inside the gas trap. Upon the addition of alumina to the bath, a rapid increase in the number of bubbles inside the gas trap was observed for about 2 seconds. This increase in the number of bubbles occurred at the same time as a jump in the potential was observed in the emf curve of the sensor. This gave further evidence that the jumps in the potential just after the additions were related to the generation of gases. The origin of these gases most certainly come from the contact of the alumina with the melt.

It was also found that some problems seen in the emf measurements were due to magnetic, electrical, and apparatus issues. These problemstried to be solved with some changes in the setup. The first change was to shield all the cables connected from the Keithley multimeter to the electrodes and properly connect the cables to earth to avoid electromagnetic or electrical interference. The multimeter was changed to a Data Acquisition System (DAQ) measurement hardware (NI 9205) compatible with a more modern software. A new software (NI Flexlogger) with the option to monitor simultaneously the emf and the temperature through real time graphs/curves was used. This allowed seeing any unusual change in the system and detecting any problem during the experiments. Finally, the sealed furnace was changed for a see-through oven with a different distribution of the heating elements.

8.2 Studies of the behaviour of the sensor in the see-through furnace

Comparison of the emf measurements with calculations and video recordings

To further investigate the behaviour of the sensor, emf measurements were performed during the dissolution of alumina in a see-through furnace. Separately, video recordings were also performed to gather more information to help to understand the behaviour of the sensor and to obtain visual information of the dissolution of the aluminas. The emf showed a jump in the potential followed by a gradual decrease until the potential more or less stabilizes after each addition. The gradual decrease before the stabilization was interpreted as an increase in the alumina concentration. After stabilization there was a fairly good agreement between the measured and calculated potential values for all additions, meaning that the concentration measurements of the sensor were comparable with the concentration expected from the calculations. The decrease in the calculated potential values were somehow comparable with the decrease in the measured potentials in the range of 3-5 wt% and becomes better in the ranges of 5-7 wt%, 7-9 wt% and 9-11 wt%. However, lack of accuracy in the measurements of the sensor was observed at low concentrations of alumina, presenting a difference of 0.1 V between the calculated and theoretical potential values between 1-3 wt% of alumina.

Video recordings showed generation of bubbles upon the addition of the alumina at the same time the jump in the potential was observed in the emf curve. This observation gave further evidence that the jump in the potential of the sensor was related with the generation of gases during the impact between the alumina and the melt. It is suggested that the moisture and air from inside the alumina pores enters into the bath during the addition. The oxygen reacts with the carbon surface of the sensor increasing the CO/CO_2 partial pressure. This will quickly increase the potential according to the Nernst equation. In later publications, it will be suggested that the formation of the bubbles may be also caused by the formation of HF gas.

The emf measurements were also used to calculate the dissolution rate of the primary and secondary alumina and to be able to compare the two types of alumina. Faster dissolution rates were observed for secondary alumina, especially at low alumina concentrations. A decrease in the dissolution rate with increasing the concentration of alumina in the melt was observed for both aluminas. The results were in fair accordance with the dissolution rates obtained from video recordings.

The dissolution process for the primary alumina was characterized by the formation of a big crust on the top of the melt followed by the detaching and sinking of alumina flake-shaped particles. On the contrary, almost no crust formation was seen for the secondary alumina. This dissolution process for secondary alumina was mainly characterized by a rapid dispersion of the alumina throughout the cryolite melt forming a white cloud composed of alumina particles until the dissolution was finished. One of the reasons for the better dispersion and less aggregation demonstrated by the secondary alumina might be related to its tendency to have a better flowability at higher HF contents.

Furthermore, SEM analysis revealed differences in the surface morphology of the primary alumina and the secondary alumina. Primary alumina had a very compact surface conformed by many laminate-shaped sections whereas the secondary alumina had a surface characterized by the presence of pores. Moisture together with the HF adsorbed on the secondary alumina might be a cause of the shattering of the particles upon the dissolution of the secondary alumina preventing agglomeration. A more fragmented alumina will have more contact area with the melt, and it will dissolve faster. On the contrary, the compact surface of the primary alumina suggests that little shattering occurs, leading to agglomerations and a slower dissolution process.

8.3 Further studies of the behaviour of the sensor

Simultaneous sensor measurements and video recordings. Comparisons of experimental results with calculations

The behaviour of the sensor was further studied through simultaneous emf measurements and video recordings of the dissolution of the alumina. The information extracted from the video recordings was used to explain the sensor results as well as the general dissolution phenomena.

Important changes in the set-up were made to performs these simultaneous emf measurements and video recordings. The first change was the implementation of new windows with better insulation to decrease heat losses from the see-through oven. Another change in the setup was to keep one of the holes of the lid open to create a gas flow from the bottom to the top of the furnace. This action was done to prevent vapours and particles from sticking to the windows and thereby enhancing the visibility of the camera. The last change was made in the initial composition of the bath. For these experiments, AlF_3, CaF_2, and LiF were added to the melt in order to decrease the liquidus temperature. This change allowed to keep the transparency of the crucible avoiding freezing of the melt in the walls and enhancing the video recordings. A complete description of the setup is described in Chapter 3 Figure 3.13.

In general, the emf curve showed a decrease after each addition of alumina which was interpreted as an increase in the alumina concentration. Then, the potential stabilized and reached a more or less constant value when the dissolution process was close to completion. For the first addition, the emf curve showed a fast decrease before the potential reached a horizontal plateau suggesting that the dissolution process was completed, while less pronounced drops and slightly declining plateaus were observed for the subsequent additions. Observations from video recordings suggested that this inclination of the plateau might be related to a crust or alumina particles remaining on the top of the bath. Further experiments when stirring was applied confirmed this hypothesis. When mechanical stirring was applied, it was observed a faster decrease in emf immediately after feeding and shorter time to reach the plateau. For all additions a horizontal plateau was reached, and no particles were observed on the top of the bath. The stirring promoted a rapid dispersion giving a faster dissolution of the alumina particles in the cryolite melt and possibly to a large degree reduced crust formation.

No jumps in the potential after the addition of alumina were observed during these experiments. The reason for not jumps in the potential might be related to the open

system used during these experiments. As it was described above, the furnace was kept open during the experiments to create a gas flow from the bottom to the top of the furnace. This new setup might help to create an equilibrium between adsorbed CO in the probe with the dissolved CO in the melt which was also in equilibrium with the partial pressure of CO above the melt.

However, for these experiments the agreement between the measured potential values with the calculations was less consistent than the agreement observed in chapter 5. The measured starting potential before the first addition in each experiment were generally around 0.03-0.04 V higher than the expected from calculations. Further, the measured decrease in the potential after each addition was generally 0.01-0.02 V higher than the calculated value. The measured total change in the potential after all alumina additions were generally 0.03 V higher than the expected values from calculations. The calculated and the experimental potential values of all the experiments from chapter 6 are presented in Table 8.1. These values serve just as a reference since the experimental data is not statistically representative.

Table 8.1 Calculated and experimental potential values from chapter 6.

Alumina concentration interval (wt%)	Calculated values		Experimental potential decrease (V)			
	Potential interval (V)	Potential decrease (V)	Alumina A	Alumina B	Alumina C	Stirring
1-2	0.09-0.05	0.04	0.04	0.03	-	0.04
2-3	0.05-0.03	0.02	0.03	0.03	-	0.03
3-4	0.03-0.02	0.01	0.02	0.02	0.02	0.02
4-5	0.02-0.01	0.01	0.02	0.03	0.02	0.01
	Total decrease	0.08	0.11	0.11	-	0.10

The weak agreement between the calculated and the experimental values are not completely understood. Some of the reasons for this weakness might be due to the more complex experimental conditions used in chapter 6 and the simplifications and assumptions made in the calculations. In chapter 5 the calculated values had a better agreement with the emf measurement possibly due to the simpler conditions used in those experiments. The experiments published in chapter 5, had an initial bath composition of mainly only synthetic cryolite and the experiments were carried out in a partially closed furnace under nitrogen gas. On the other hand, during the experiments published in chapter 6, the initial bath composition

of the melt was more complex with the addition of AlF_3, CaF_2, and LiF. Another reason for the differences between the calculated values and the emf measurements in chapter 6 might be related to the sensitivity of the sensor to variations in gas concentration in or above the melt in an open furnace, especially in a new setup where the furnace was partially open.

The simultaneous emf measurements and video recordings allowed to find some correlations between the characteristics of the dissolution process observed with the camera and the emf curve of the sensor. The fast decrease in the emf curve just after the addition of the alumina had a good correlation with the rapid dispersion and fast dissolution of the alumina observed with the camera during the first seconds of the process. Then, a second correlation was observed when an almost completely dissolved crust was observed with the camera when the emf curve was about to reach a constant value or plateau.

The estimated dissolution times based on the sensor measurements generally increased with increasing alumina concentration. This was reflected in the behaviour of the emf curve, with a fast decrease immediately after the first alumina addition and a less pronounced decrease as the initial alumina concentration increased in the subsequent additions. The same trend in the increasing of the dissolution time with the increasing of the alumina concentration in the melt was observed with video recordings.

In chapter 4 and 6, sudden emf drop after some alumina additions was observed in some of the experiments when the graphite quasi-reference electrode was used. The potential later increased and more or less stabilized forming a plateau. This type of behaviour of the emf was believed to be due to a lot of alumina ending up close to the sensor during or after feeding, rapidly increasing the concentration in the volume nearby the sensor. Then, the alumina concentration around the sensor decreases as the alumina concentration gradient decrease with time due to convection. Another possible explanation could be gas entering inside the reference electrode increasing the partial pressure of CO or CO_2 gas inside the reference electrode, resulting in a decrease in the potential as follows from the Nernst equation.

8.4 Dissolution process of the alumina

Video recordings of the dissolution of different types of alumina

In view of the great potential of the camera to characterize and extract important information of the dissolution of the alumina, and the great interest from the industry to obtain more information about the dissolution of the alumina, the entire dissolution process of different bulk alumina and alumina fines was video recorded. The aim of the work was to obtain the characteristics of the dissolution mechanism and dissolution time and evaluate a possible correlation with the physicochemical properties of the aluminas. Video recordings of the dissolution process of subsequent additions of 1 wt% alumina in a cryolite based melt contained in a quartz crucible were performed. Three different industrial secondary aluminas were used. The experiments were conducted with the alumina as received, as well as with only the fines fraction consisting of particles ≤ 45 μm.

The dissolution mechanism of the bulk alumina was characterized by a rapid dispersion and dissolution of alumina particles immediately after addition, succeeded by the formation of a crust with gas bubbles trapped inside. This was followed by the detaching and sinking of alumina bath-particles, and further a decrease in the thickness of the crust until the completion of the dissolution. The formation of bubbles inside the crust might be due to the generation of gas when the alumina is exposed to the bath. HF gas could be generated when fluoride species reacts with moisture and water is adsorbed on the alumina. Another source of HF formation involves fluoride species reacting with hydroxides species.

Alumina fines showed less dispersion of the particles immediately after feeding. The dissolution process of the alumina fines took place only at the alumina layer-bath surface interface and inside of the alumina layer. Towards the end of the dissolution process of alumina fines the crust appeared to have smaller pores and looked more compact than the crust of the bulk alumina. The growing of the crust or occurred over the surface of the bath, resembling a foam. These characteristics lead to less contact area between the alumina and the bath resulting in longer dissolution times.

The estimated dissolution time shows a general trend for all the aluminas, characterized by an increase in the dissolution time with increasing initial alumina concentration. The average time to dissolve 1wt% of alumina for most of the bulk aluminas was between 6 to 10 minutes (0.42-0.25 g/min) and the average time for alumina fines was between 12 to 14 minutes (0.21-0.18 g/min)

The results of the dissolution of all bulk alumina and alumina fines showed no clear correlation between the physicochemical properties and the dissolution time. However, excluding the results from Alumina A bulk, a correlation between the average dissolution time and physicochemical properties such as PSD, LOI, BET, alpha content, and some chemical elements were obtained

It was found that the average dissolution times had a negative correlation with the PSD, meaning that smaller particles with small surface area tend to promote longer dissolution times. The size of the particles and the lack of dispersion of alumina fines upon addition leads to the formation of a crust with a high number of small pores. Small pores reduce the penetration and the contact of the bath inside the crust. In addition, a high number of small pores in the crust lead to a low-density crust and thus larger floating times. This observation is closely related with the correlation found between the maximum crust thickness of the aluminas and LOI. The generation of gases during the dissolution of alumina fines appears to be ineffective in dispersing the alumina particles inside the cryolite, since alumina fines, only remains on the surface of the melt. Therefore, a growth of the alumina layer over the surface of the bath happens, where the contact between the alumina and the melt is not effective and the temperatures are lower than the temperature inside the melt, resulting in larger dissolution times. On the other hand, the better dispersion of bulk alumina during addition leads to the formation of a less compact crust. Then there is more contact between the melt and the alumina leading to the detachment and sinking of alumina flakes resulting in shorter dissolution times

8.5 Impact of the findings

The emf measurements indicated that the alumina probe is a promising tool for in-situ measurements of alumina concentration in cryolite melts, when properly calibrated. With the in-situ emf measurements the dissolution of the alumina can be monitored during the whole dissolution process.

This can give a more detailed picture of the dissolution. It not only gives a general dissolution rate but can also give important information about the different characteristics of the dissolution process and the amount of alumina dissolved at a particular time.

The dissolution time for primary alumina and different secondary aluminas could be obtained with the in-situ emf measurements of the sensor. The sensor is sensitive enough to detect differences in dissolution rate between primary and

secondary alumina, measuring longer dissolution times for primary alumina. No significant difference in the dissolution time among the secondary aluminas were observed. However, the three different secondary aluminas used in this work presented very similar physicochemical properties. The sensor could be used in a laboratory to measure the dissolution of different aluminas with difference physicochemical properties and potentially establish difference between them.

Since the sensor and reference electrode are based on carbon, the principle is expected to function for long periods in the corrosive cryolite bath. This can potentially make the principle applicable in an industrial setting. However, some factors such as magnetic field, electric field and different gases in an industrial setting are believed to be important obstacles to the correct performance of the sensor. Another important challenge to face will be the calibration of the sensor. Since the sensor measures voltage differences, a previous calibration to relate voltage to alumina concentrations is necessary. There is still work to be done to relate the emf directly to an alumina concentration, but with a proper functioning reference electrode and calibration it may be possible to relate the emf directly to an alumina concentration.

Video recordings can be used as tool to combine with the emf measurements to obtain more information about the dissolution characteristics of different aluminas. Video recordings showed potential to serve as an important tool for the industry to test and characterize different aluminas. In chapter 7 , Alumina A bulk had the longer dissolution time among the bulk alumina, which is normally considered as a negative characteristic since fast dissolution rates are always desirable in the industry. However, Alumina A bulk had also the longest floating time in the bath, which can be beneficial in the industry to avoid sinking of rafts and to avoid formation of sludge in the metal pad of the cell avoiding instability and decrease in current efficiency. This type of information can be beneficial for the industry to get different characteristics of the aluminas used in the pots and to extract the key parameters that influence the dissolution process.

Chapter 9 Conclusions

9.1 Principle and performance of the sensor

The behaviour of the electrochemical alumina sensor was studied under different experimental conditions. In a sealed furnace under nitrogen atmosphere and initial bath composition 99 wt% synthetic cryolite and 1 wt% alumina, the decrease in the emf with the added alumina dose was comparable to the calculated values. The total decrease in potential when saturation was reached was also corresponding with calculated values, which supports the working principle stated for the sensor.

It was revealed that the sensor was sensitive to variations in gas composition above the melt. This sensitivity was observed as changes in the potential when the feeding tube was opened before the addition of alumina. It is believed that the cause of this sensitivity is due to the reaction of oxygen from the air with the carbon probe or carbon crucible resulting in changes in the partial pressures of CO and CO_2. During the experiments carried out in the see-through furnace, the sensor measurements were not affected by air entering to the furnace prior to additions. Since the see-through furnace was not completely sealed, a buffer system with respect to the amounts of air entering the furnace might have established. This hypothesis was supported by experiments where this sensitivity was much reduced when a constant flow of CO_2 into the furnace prevented large variations in the partial pressures of CO and CO_2.

In different experiments, sudden jumps or drops in the emf measurements immediately after the additions of the alumina were observed. These behaviours are not understood. However, it is believed that the sudden jumps might be due to generation of CO, CO_2, or both gases in and above the melt. The sudden drops might be due to a lot of alumina ending up close to the sensor during feeding, rapidly increasing the concentration in the volume nearby the sensor.

During the experiments carried out with an open hole in the see-through oven, no sudden jumps in the potential after the addition of alumina were observed. The explanation is again believed to be related to the establishing of a buffer system in the atmosphere of the furnace. Less agreement between the measured potential and the calculated values was found for these experiments in comparison to the previous setups. The reason for the larger difference between the calculated values and the emf measurements in these experiments with an open furnace is not fully understood.

Convection induced by mechanical stirring in the melt resulted in a faster decrease in emf immediately after feeding and shorter time to reach the plateau values. The stirring promoted a rapid dispersion resulting in faster dissolution of the alumina particles in the melt and possibly also reducing crust formation.

9.2 Dissolution time and characteristics of the alumina dissolution

The dissolution times obtained based on the sensor measurements were slightly smaller than the dissolution times obtained based on the video recordings. A general trend from the emf measurements and the video recordings was the increase in dissolution time with increasing initial alumina concentration in the melt. The dissolution was characterized by the rapid dispersion and dissolution of a white cloud consisting of alumina particles followed by the formation of thin crust when the melt had low alumina content. Formation of a thicker crust and detachment and sinking of flake-shaped particles was observed when the melt had high alumina content.

In addition, both techniques also showed a significantly faster dissolution process for the secondary alumina compared to the primary alumina, which is consistent with previous results reported in the literature. The dissolution of the primary alumina was characterized by the formation of a thick crust after feeding, followed by a slow dissolution including detachment of large alumina-bath flakes. The dissolution of the secondary alumina was characterized by better dispersion of all the particles throughout the melt and the formation of a thinner crust leading to a faster dissolution.

Alumina fines showed less dispersion of the particle compared to primary and secondary bulk alumina upon feeding. The dissolution process of the alumina fines took place only at the alumina layer-bath surface interface and inside of the alumina layer. Towards the end of the dissolution process of alumina fines the crust or alumina-bath layer appeared to be more compact and with smaller pores than the crust of the bulk alumina.

No clear correlation between the dissolution time and the physicochemical properties of the alumina were found when the results from all the aluminas were considered in chapter 7. However, the average time to dissolve 1wt% of Alumina B bulk and Alumina C bulk was between 8 to 9 minutes. These average dissolution time values of these bulk aluminas are considerably smaller compared

to the average dissolution time of the alumina fines which were between 12 to 14 minutes. The slower dissolution times of alumina fines are consistent with previous results reported in the literature.

Some correlation between the dissolution time of the aluminas and physicochemical properties were found when Alumina A bulk results were excluded in chapter 7. PSD, BET, and gamma content were found to have a negative correlation to the dissolution time, meaning that particles with large surface area tend to promote shorter dissolution times. On the other hand, LOI was found to have a positive correlation with the dissolution times, meaning that larger values result in larger dissolution times. Not all of the correlations found in the current work are consistent with what has been reported in literature, showing the complexity of alumina dissolution.

Chapter 10 Further work

Studies to further understand the behaviour of the sensor are required. Additions of liquid cryolite bath saturated with alumina can serve as a method to check if the response of the sensor is fast, and that obtaining a constant potential value or plateau in shorter time. Such additions could also help to understand more about the response of the sensor to the generation of gas. These experiments could serve to clarify if the jumps observed in some emf measurements are due to the release of gases when the alumina powder get in contact with the melt. Some experiments to add liquid cryolite melt saturated with alumina were carried out but failed due to technical difficulties. No further experiments were done because of the limited time frame of the project.

Different carbon materials could be used in the probe and reference electrode for the alumina concentration measurements to further explore the behaviour of the sensor. Graphite has a relatively homogeneous surface in comparison to e.g. industrial carbon which has a lot of cracks and pores in addition to impurities. The cracks, pores, and impurities give a larger density of active sites for the CO adsorption which in turn could affect the sensor behaviour upon alumina addition and dissolution.

Experiments to study the sensitivity of the sensor to different gases are recommended. Emf measurement can be combined with a gas detector above the melt to obtain information and identify the gasses formed during the addition and dissolution of the alumina.

Mechanical stirring during the experiments showed to simplify the estimation of the dissolution time based on the emf measurements. More experiments applying mechanical stirring at different rotation rates are needed to further evaluate the effect of convection in the dissolution of the alumina. However, it is believed that at higher stirring rates, small differences between the dissolution time of different aluminas will be observed.

A rotating probe electrode can potentially improve the measurements. Gas bubbles were observed on the boron nitride surface of the reference electrode as well as on the graphite surface of the probe. These gasses bubbles were seen in all the experiments, and even before the additions of alumina. These bubbles can be a reason for noise in the emf measurements. Through rotation the bubbles would likely be detached. Mechanical stirring would probably have a similar but smaller effect.

Improvements in the setup can be achieve using more resistant materials. Higher grade quartz can be used for the crucible to obtain longer lifetime. With more resistant materials higher temperatures can be set in the furnace. This allows to explore baths with different compositions and higher liquid temperatures. This allows to try baths with fewer compounds and limit the use of LiF. Although there is no strong evidence that LiF alter much the alumina dissolution.

Video images could be improved with the use of a camera with a macro lens to magnify the images and to capture more details. More detailed images could help to extract more information e.g. the structure of the crust, the gas bubbles formation inside it and the detachment of alumina-bath flakes at the bottom of the crust.

It is important to point out that the path towards the use of the sensor at an industrial level is still quite long. This work represents only the first of various steps in the study of the behaviour of the sensor. One important step in future work will include to improve the repeatability of the experiments and obtain data that is statistically representative, to be able to gain more information and understanding of the results. The next challenge to solve for the application of the sensor at an industrial level will be the instability in the sensor measurements in the range of alumina concentration between 1 to 3 percent of alumina, common concentrations used in electrolysis cells. Further it will be important to relate the emf measurements directly to an alumina concentration for the implementation of the sensor in the industry. This could be possible with a proper functioning reference electrode and calibration. The challenge is to manage the gas composition (CO/CO_2) that is also a part of the equilibrium. One can hope that this is relatively constant in a Hall-Héroult cell. Anyway, it was shown that the graphite electrode senses differences in oxide concentration reasonably in line with what can be expected of an emf sensor. This opens for further development of an in-situ alumina concentration sensor.

APPENDICES

Appendix A Sensor and see-through oven

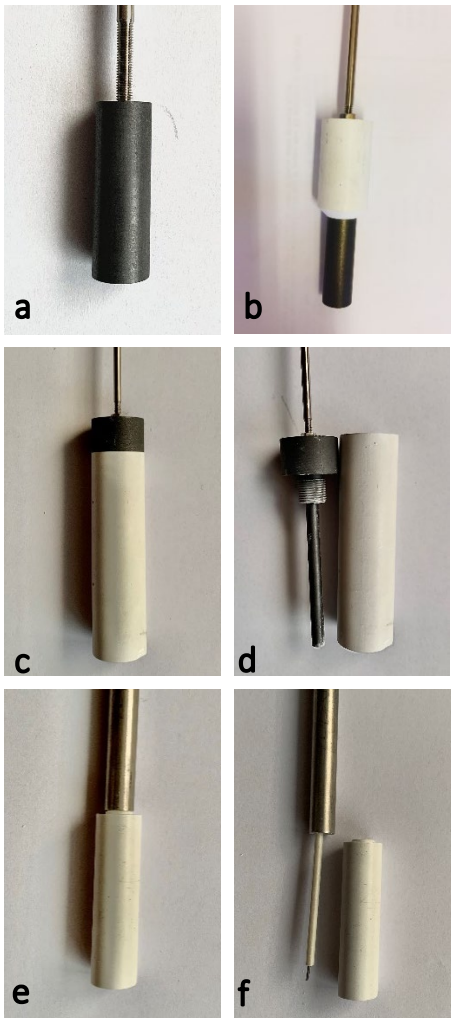

Figure A.1 a) graphite probe **b)** graphite probe shielded **c)** graphite quasi-reference electrode used in chapter 4 **d)** graphite quasi-reference electrode opened **d)** aluminium reference electrode used in chapter5 **e)** aluminium reference electrode opened.

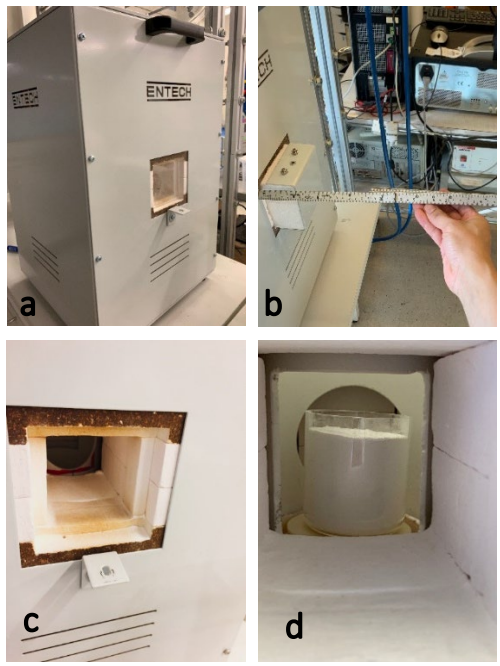

Figure A.2 a) see-through furnace without the wall-plugs. **b)** see-through furnace with the wall-plugs. **c)** view of one of the tunnels of the furnace. **d)** quartz crucible containing cryolite inside the furnace.

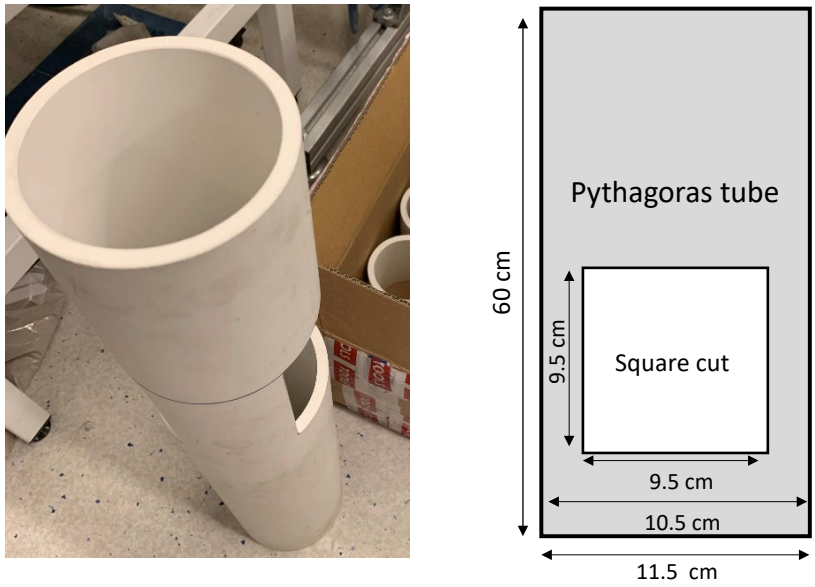

Figure A.3 Pythagoras tube with square holes for the see-through oven.

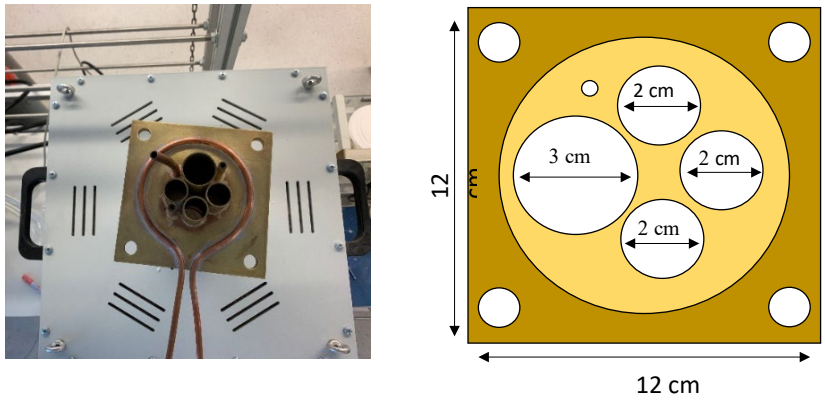

Figure A.4 Metal lid for the see-through oven.

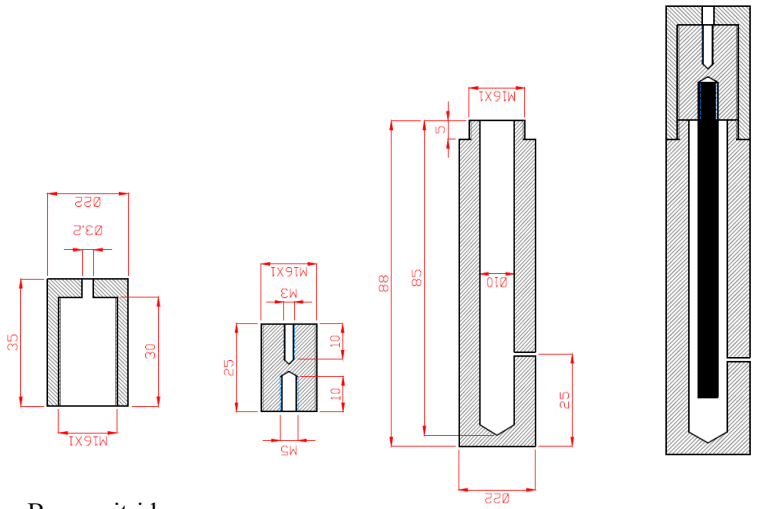

Boron nitride shield | Graphite connector | Boron nitride tube

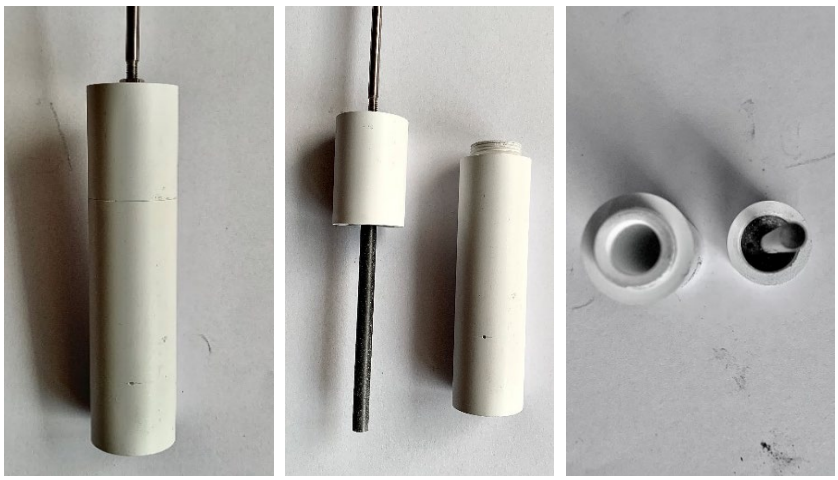

Figure A.5 Graphite quasi-reference electrode completely shielded with boron nitride. Improved version used in chapter 6 and presented in chapter 3.

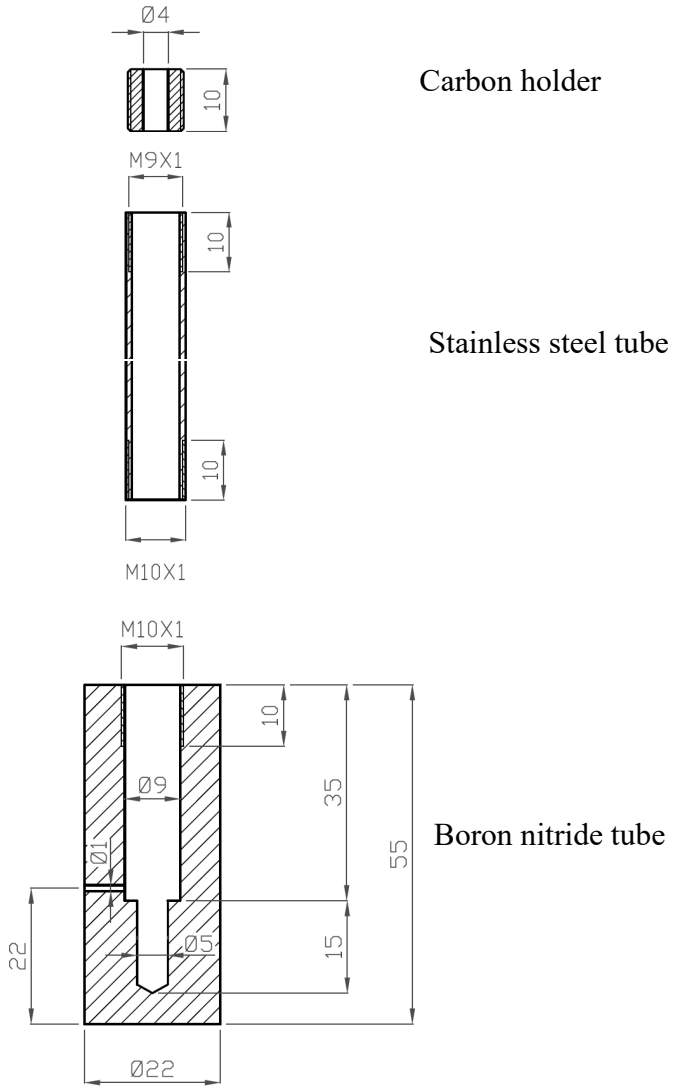

Figure A.6 Aluminium reference electrode. Improved version presented in chapter 3.

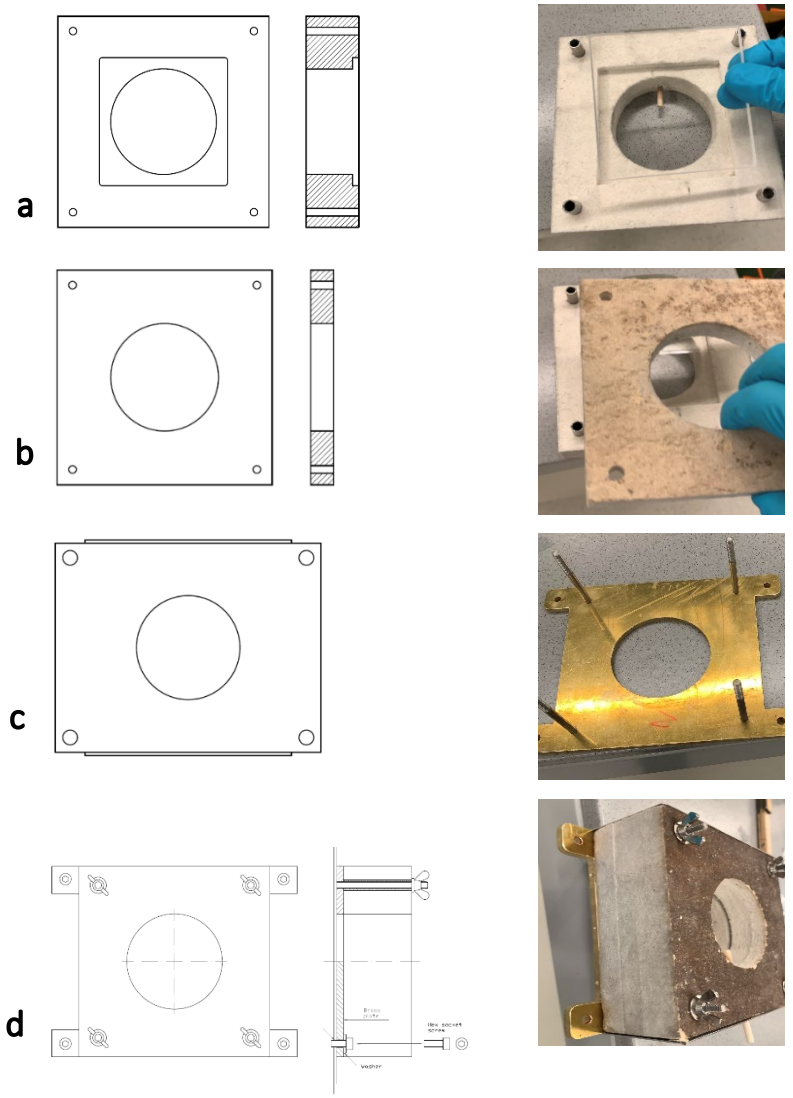

Figure A.7 a) insulation pocket for the quartz windows **b)** insulation cover for the quartz windows **c)** metal cover for the insulations and quartz window **d)** all the pieces assembled.

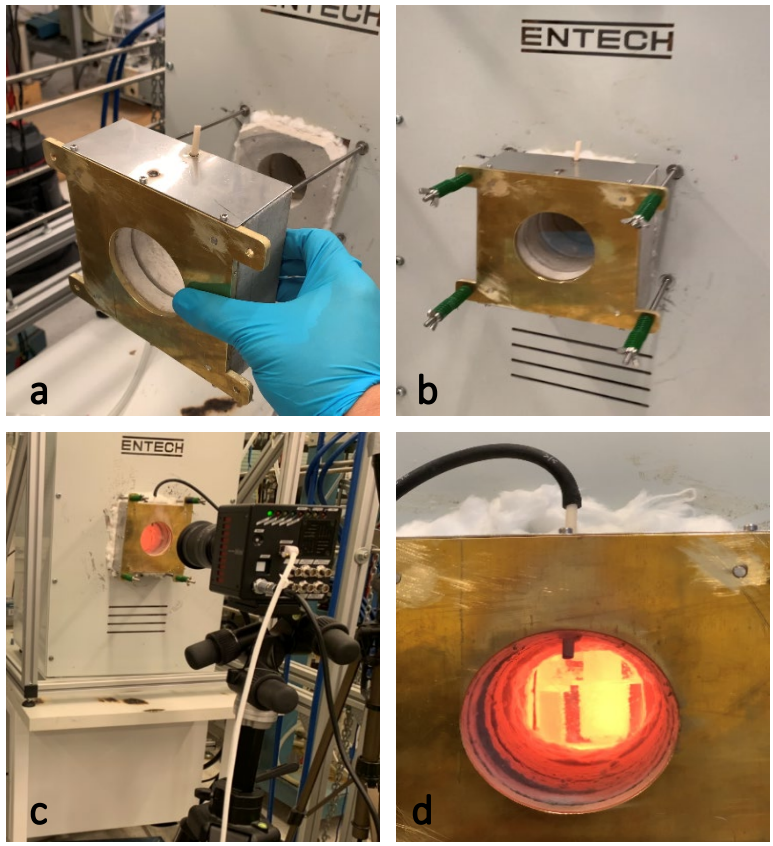

Figure A.8 a) installation of the windows in the wall of the oven. An alumina tube is inserted on the upper part of the window to flush N_2 gas **b)** window fixed in the wall of the oven **c)** camera located in front of one of the windows **d)** view inside the oven. In the window of the oven, a hose is connected to the alumina tube for flushing of N_2 gas. The graphite probe is on the left and the graphite quasi reference electrode is on the right of the crucible.

Appendix B Video recordings

Appendix B contains links to video recording from selected dissolution processes involving different alumina properties and melt compositions. The dissolution processes of the aluminas were recorded at 50 fps with the high-speed camera. The videos showed here are played at 30 fps.

Video B.1 shows the first addition of 3 wt% primary alumina. Initial bath composition: 75% synthetic cryolite 75 wt%, AlF_3 wt% and CaF_2 10 wt%. This video is relevant for the results showed in chapter 5.

Video B.1 https://www.youtube.com/watch?v=iquZt2PTJNE

Video B.2 shows the first addition of 1 wt% secondary alumina. Initial bath composition: synthetic cryolite 74 wt%, AlF_3 15 wt%, CaF_2 6.5 wt%, and LiF 3.5 wt%. Simultaneously emf measurements were performed. Graphite reference on the left. Graphite probe on the right of the crucible. This video is relevant for the results showed in chapter 6.

Video B.2 https://www.youtube.com/watch?v=F7tuIB06KJ4

Video B.3 shows the fourth addition of 1 wt% secondary alumina. Initial bath composition: synthetic cryolite 74 wt%, AlF_3 15 wt%, CaF_2 6.5 wt%, and LiF 3.5 wt%. Simultaneously emf measurements were performed. The graphite quasi-reference electrode is shown on the left, the Pt/Pt-Rh wires of the thermocouple are shown in the middle and the graphite probe in on the right of the crucible. This video is relevant for the results showed in chapter 6.

Video B.3 https://www.youtube.com/watch?v=hdfNHrd4kXM&t=180s

Video B.4 shows the fourth addition of 1 wt% secondary alumina when mechanical stirring was applied. Initial bath composition: synthetic cryolite 74 wt%, AlF_3 15 wt%, CaF_2 6.5 wt%, and LiF 3.5 wt%. Simultaneously emf measurements were performed. The graphite quasi-reference electrode is shown on the left, the metal stirrer is shown in the middle and the graphite probe in on the right of the crucible. This video is relevant for the results showed in chapter 6.

Video B.4 https://www.youtube.com/watch?v=LYprvKyyxoU

Video B.5 shows the first addition of 1 wt% bulk alumina. Industrial bath with initial composition of cryolite 78 wt%, AlF_3 (9 wt%), CaF_2 (6 wt%), Al_2O_3 (2 wt%), and LiF (5 wt%). The Pt/Pt-Rh wires of the thermocouple are shown in the middle of the crucible**.** This video is relevant for the results showed in chapter 7.

Video B.5 https://www.youtube.com/watch?v=9Iwhbwx8QQg

Video B.6 shows the fourth addition of 1 wt% bulk alumina. Industrial bath with initial composition of cryolite 78 wt%, AlF_3 (9 wt%), CaF_2 (6 wt%), Al_2O_3 (2 wt%), and LiF (5 wt%). The Pt/Pt-Rh wires of the thermocouple are shown in the middle of the crucible**.** This video is relevant for the results showed in chapter 7.

Video B.6 https://www.youtube.com/watch?v=7fmzjlC2kSU

Video B.7 shows the fourth addition of 1 wt% bulk alumina some minutes after the feeding was performed. It shows a typical detachment and sinking of alumina-bath flake. Industrial bath with initial composition of cryolite 78 wt%, AlF_3 (9 wt%), CaF_2 (6 wt%), Al_2O_3 (2 wt%), and LiF (5 wt%). The Pt/Pt-Rh wires of the thermocouple are shown in the middle of the crucible**.** This video is relevant for the results showed in chapter 7.

Video B.7 https://www.youtube.com/watch?v=ScOv0sHIMHI

Video B.8 shows the first addition of 1 wt% alumina fines. Industrial bath with initial composition of cryolite 78 wt%, AlF_3 (9 wt%), CaF_2 (6 wt%), Al_2O_3 (2 wt%), and LiF (5 wt%). The Pt/Pt-Rh wires of the thermocouple are shown in the middle of the crucible. This video is relevant for the results showed in chapter 7.

Video B.8 https://www.youtube.com/watch?v=SiTZ5hoWEjM

Video B.9 shows the fourth addition of 1 wt% alumina fines. Industrial bath with initial composition of cryolite 78 wt%, AlF_3 (9 wt%), CaF_2 (6 wt%), Al_2O_3 (2 wt%), and LiF (5 wt%). The Pt/Pt-Rh wires of the thermocouple are shown in the middle of the crucible. This video is relevant for the results showed in chapter 7.

Figure B.9 https://www.youtube.com/watch?v=i9KOQojFWJ4

Appendix C Supplementary Information

This appendix contains important details that were not published in the correspondent chapter. These details help to better understand some of the experiments and complement some of the results presented in some of the main chapters.

Chapter 4

Method

For the graphite quasi-reference electrode calculations, E^0 is equal to zero because the probe and the quasi-reference electrode were made of the same material, graphite. Then, the Nernst equation for the cell reaction becomes as written in Equation 4.7. Applying the same reasoning as for the case with the graphite quasi-reference, the half-cell reactions between the graphite probe and the aluminium reference electrode were shown in the Equations 4.10 and 4.11. For the aluminium reference calculations, Equation 4.15 could be omitted. However, because the probe and the aluminium reference electrode are made of different materials, E^0 is not zero as opposed to when graphite is used as reference. Then, E^0 must be included in Equation 4.16 while it can be omitted in Equation 4.7.

Experimental work

The present work started from the ground up with different designs and construction of a graphite probe, a graphite quasi-reference electrode and an aluminium reference electrode. Some ideas for the first designs and dimensions of the aluminium reference electrode, the graphite probe and the experimental setup used in this work were based on similar concepts previously used by Kjos et al [1], Sommerseth [2] and Vasyunina et al [3]. However, due to the innovative nature of the research, many of the parameters in the design of the reference electrodes and setup were still unknown. One of the first parameters to find was the size of a hole drilled above the bottom of the reference electrode tube. The hole was to ensure ionic contact between the alumina saturated bath inside the tube of the electrode (chamber I) and the bath in the crucible (chamber II). Hole diameters between 1 mm to 2 mm were tried for the reference electrodes. Holes above this rage were tried for the aluminium reference leading to continuous

leakage of the molten aluminium from the chamber of the reference electrode to the melt. The assumption of a molten aluminium leakage came from the drifting in the potential measurements observed several times during some experiments where the aluminium reference was used. Due to the leakage observed for the aluminium reference, holes above 2 mm in diameter were not tried for the graphite reference electrode. The study of the impact of the diameter of the hole on the voltage measurements was not studied. This could be an interesting parameter to further investigate in the future.

Diverse experiments

Some emf measurements presented in Chapter 4 were performed 22 and 48 hours after starting the experiments. These measurements are shown in Figure 4.10 and 4.11. These experiments were performed just to investigate some of the behaviours of the sensor and to get information about the durability of the electrodes. Due to melt evaporation losses with time, the duration of the experiments to study the characteristics and dissolution time of the alumina was usually around 1 hour, and up to 4 hours in some cases.

References

1. O. Kjos, T. Aarhaug, H. Gudbrandsen, A. Solheim and E. Sybakmoen, "Fundamenetal Studies of Perfluorocarbon Formation," in 10th AASTC, 2011.

2. C. Sommerseth, PhD Thesis: The Effect of Production Parameters on The Performance of Carbon Anodes for Aluminium Production, Trondheim: Norwegian University of Science and Technology, NTNU, 2016.

3. N. Vasyunina, I. Vasyunina , Y. Mikhalev and A. Vinogrado, "The Solubility and Dissolution Rate of Alumina in Acidic Cryolite Aluminous Melt," Russian Journal of Non-Ferrous Metals, vol. 50, no. 4, pp. 338-342, 2009.

Chapter 5

Experimental work

The measured temperature inside the melt was around 980 °C. It was monitored with a house made thermocouple type S (Pt/Pt-Rh). The melt composition was 99% cryolite and 1 wt% alumina. At this melt composition the expected liquidus temperature was around 1000°C. This discrepancy between the measured and expected temperature could be due to some of impurities present in the melt. It is believed that the superheat was around 0 °C because the melt was heated just until the melt started to reach the liquidus point. However, this represents an important uncertainty around the exact value of the superheat of the melt, which could have an important impact on the dissolution times presented in Chapter 5. Another possibility for the discrepancy between the measured and expected temperature could be due to a malfunction of the thermocouple. A possible deviation of the the thermocouple from the correct value of the temperature does not seem to have a great impact on the results presented in Chapter 5. Figure C.1 shows the theoretical calculation using 1000 °C as a temperature value instead of 980 °C as it was used in Chapter 5.

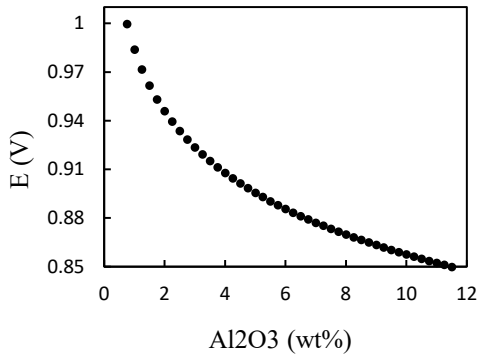

Figure C1: Calculated values of the potential of the alumina probe vs. the aluminium reference electrode as a function of alumina concentration (T= 1000 °C)

Table C1: Theoretical and experimental potential values for different ranges of alumina concentration. The theoretical values are calculated at T = 1000 ˚C.

Range of alumina concentration (wt%)	Calculated values		Experimental	
	Potential interval (V)	Potential decrease (V)	Potential interval (V)	Potential decrease (V)
0.25-1	1.06-0.98	0.08	-	-
1-3	0.98-0.92	0.06	1.08-0.92	0.16
3-5	0.92-0.90	0.02	0.92-0.91	0.01
5-7	0.90-0.88	0.02	0.91-0.89	0.02
7-9	0.88-0.86	0.02	0.89-0.87	0.02
9-11	0.86-0.85	0.01	0.87-0.86	0.01

The new calculated values shown in Table C.1 do not show a significant difference compared to the values obtained at 980 ˚C, shown in Table 5.1. There is still an important difference between the calculated and the measured potential values at low alumina concentrations. However, there is a better agreement between the calculated and the theoretical values in the rage from 7 to 9 wt% of alumina.

Particle size distribution and morphological surface analysis

The particle size distribution (PSD) and morphology of the alumina was studied by Scanning Electron Microscopy (SEM). The measurements were performed in a Zeiss Supra 55 VP for both primary and secondary alumina. The accelerating voltage (EHT) was 10 kV, and the working distance (WD) was 10 mm. The samples for SEM were obtained from a premixed batch of approximately 100 g of alumina for each type of alumina. These different 100 g alumina batches were taken from 2.5 kg bags of alumina received from the industry. It is important to highlight that these 2.5 kg bags of alumina were not premixed before the 100 g alumina batches were taken. This represents a source of error in the method to collect the sample and could influence in the particle size distribution shown in Chapter 5. No coating or special pretreatments were applied to the alumina samples before SEM analysis. The samples were dusted on an adhesive

conductive carbon disk attached to an aluminum mount before examination. Each sample contained around 250 alumina grains. The diameters and axes for each grain were measured on high magnification SEM images using Image J program. Particle size distribution data was obtained by the average axes measured for each type of alumina. Two parallels were performed for each type of alumina, representing an overall of 400-500 of individual grains measurements. One of the disadvantages of using this method to calculate PSD was the lack of parallels performed. The lack of parallels was due to the long periods for the analysis and measurements of the alumina grains on the SEM pictures. This drawback could also affect the results presented in Chapter 5. Laser diffraction, a more classic methodology to obtain the PSD was used in Chapter 7. Laser diffraction had also the advantage to perform analysis on much wider samples.

Results

Technical problems during some experiments

In Chapter 5, it was discussed that prior to the first addition of alumina, oscillations between 1.0 to 1.1 V (0.1 V) were observed, see Figure 5.5. The origin of these oscillations was believed to be due to the instability of the sensor at low alumina concentrations. These oscillations were accompanied of periodic violent drops and jumps of several volts of magnitude in the signal due to a technical problem. Because the magnitude of these jumps and drops in the voltage due to this technical problem was much larger than the oscillations coming from the sensor measurements, this part of the graph was not shown. The cause of the technical problem was found to be a bad connection in one of the cables connected to one of the electrodes. The cable was adjusted, and the problem was solved just few seconds before the first addition. For this reason, no constant value or clear plateau was obtained before the first addition.

These kind of problems with electrical connections, noise in the signal and sudden and violent jumps in the measurements which were not related with the alumina dissolution, but more to technical problems, occurred very frequently at this part of the investigation. These problems were in addition to other issues such as breaking of the crucibles or the electrodes during the experiments.

Drawbacks and limitations of the sensor

The mentioned challenges and technical problems further made it very difficult to follow the dissolution of alumina for more than 1 hour on several occasions. However, most of the experiments served to measure one or two additions of

alumina before the experiment failed. Even though this data was not shown in the thesis because they were isolated additions, all these experiments served to confirm on several occasions that the measurements were in agreement with the expected theoretical values. It is important to highlight that the lack of repeatability of the experiments was a major concern during the research and represents an important limitation to the obtention of more experimental data to evaluate the accuracy and performance of the sensor.

Another limitation of the sensor was its sensitivity in the potential measurements to changes when the oxide activity was low as suggested in Figure 5.2, showing the fast exponential increase in potential when approaching zero alumina concentration. Figure 5.5 illustrates this, as the initial potential increase is significantly larger for the first addition than for the subsequent additions. Moreover, a lower accuracy in the measurements of the sensor was observed at low concentrations of alumina, presenting a difference of 0.1 V between the calculated and theoretical potential values between 1-3 wt% of alumina. This is an important setback to consider from an industrial perspective because these low concentrations are in the normal operating range of the industrial electrolysis cells.

Different phenomena observed

Moreover, a feature of the emf-curve which was unexpected was the abrupt increase in the potential after each addition. The fast response on the addition suggested that it was related to a surface phenomenon. The alumina fed to the bath was also introducing air and moisture into the bath. The air originates from the ambient air surrounding the alumina particles as they enter the bath. Some of the air inside pores in the alumina particles might also have entered the bath. The oxygen may react with the carbon surface of the sensor increasing the CO activity around the sensor. At this point of the investigation, the alumina was not characterized by any other methods than the SEM. However, in the following publications presented in Chapter 6 and 7, the LOI and MOI content of the alumina was calculated. In addition, generation of gas seen as bubbles formation inside the alumina crust after the feeding, was observed by video recordings in Chapter 6 and 7. This new information led to the obtention of more information about the nature of the gases observed during the feeding. The bubbles observed inside the crust during the feeding could have originated from several reactions. Hydrolysis of the melt and melt fumes was one possibility. HF gas could also be generated when fluoride species reacted with moisture and water adsorbed on the alumina. The generation of these gases could also be involved in the abrupt increases in the potential observed in Chapter 5. More detailed information about the source of the gas and the possible reactions are described in Chapter 6 and 7.

Determination of the alumina dissolution times

At this point of the investigation, the method to determine the dissolution time of the alumina from the electrochemical measurements had not been completely developed. The first method to determine the dissolution time proposed to define the dissolution time from the moment when the alumina was added until the moment a plateau was reached or when the potential was more or less stabilized. This method depended on the appreciation of each person to read the final time, which might lead to different results. For this reason, it is important to clarify that the times reported might have an important deviation. A better methodology for determining the final time of the dissolution of alumina was proposed in Chapter 6. However, important deviation in the dissolution time values were still expected and reported in that chapter.

Chapter 6

Method

The melt composition used in Chapter 6 differs from the ones used in Chapter 4 and 5. This affects the Na_2O activity as a function of the alumina concentration. As the emf is a function of the Na_2O activity, the emf will have a different relation to the alumina concentration. One main difference is the more rapid approach to the saturation value of the melt from 12 wt% of alumina presented in Figure 4.2 and 5.2 to 8 wt% of alumina in Figure 6.1.

Results

Due to technical problems the sensor data from the first two addtions of Alumina C could not be obtained. For this reason the emf curve on the lower part of Figure C.2 shows addition number 3, 4, 5, and 6. Here, it was possible to estimate the dissolution time only for the third and the fourth addition based on the alumina sensor measurements. Unlike the results obtained for Alumina A and B, the sudden emf drop after each addition was larger for Alumina C. The potential later increased and more or less stabilized forming a plateau. This type of behaviour of the emf can be explained by a lot of alumina ending up close to the sensor during or after feeding, increasing the concentration rapidly in the volume nearby the sensor. Afterwards the alumina concentration around the sensor decreases. The video recordings for Alumina C appear not very different from the video recordings for Alumina A and B, and thus cannot explain the difference in the emf curve. It is possible that the sensor, which senses dissolved oxide that is not optically visible, experiences a higher local alumina concentration when adding C than A and B. This difference may not necessarily be observable in the videos. It is important to highlight that a difference between the videos and the sensor is that the sensor senses dissolved oxide, while the videos show undissolved oxide.

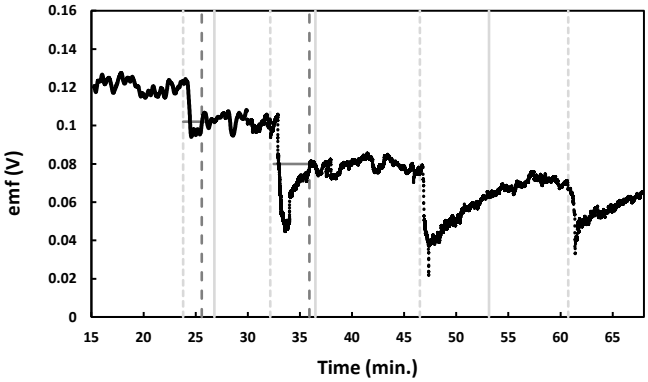

Figure C.2: emf of the alumina sensor for additions of Alumina C. Emf (black line), Time of each addition (light grey short dashed line). Time for end of dissolution based on the video recording (light-grey line). Line for extension of the plateau (dark grey solid line). Time for end of dissolution based on the alumina sensor (dark grey long dashed line).

In general, the difference in the dissolution times based on the alumina sensor and video recordings was especially pronounced at lower initial alumina concentrations. This could be because a major part of the alumina dissolve quickly at low alumina concentrations and the emf measurements can sense the difference in oxide concentration at the two electrodes, while the camera shows mainly the alumina on the top of the melt. On the other hand, at higher initial alumina concentrations more of the alumina ended up in the crust making the dissolution times based on the sensor and video recordings more similar to each other.

ISBN 978-82-326-6471-9 (printed ver.)
ISBN 978-82-326-5598-4 (electronic ver.)
ISSN 1503-8181 (printed ver.)
ISSN 2703-8084 (online ver.)

NTNU
Norwegian University of
Science and Technology